Summer 2022

Fully kinetic particle-in-cell simulations of plasma-surface-dust interactions for lunar exploration

Jianxun Zhao

Department: Mechanical and Aerospace Engineering

FULLY KINETIC PARTICLE-IN-CELL SIMULATIONS OF PLASMA-SURFACE-DUST INTERACTIONS FOR LUNAR EXPLORATION

by

JIANXUN ZHAO

A DISSERTATION

Presented to the Graduate Faculty of the

MISSOURI UNIVERSITY OF SCIENCE AND TECHNOLOGY

In Partial Fulfillment of the Requirements for the Degree

DOCTOR OF PHILOSOPHY

in

AEROSPACE ENGINEERING

2022

Approved by:

Dr. Daoru Han, Advisor
Dr. Xiaoming He
Dr. Serhat Hosder
Dr. Henry Pernicka
Dr. Guirong Yan

ABSTRACT

The studies involving lunar surface explorations have drawn attentions in recent years. A better understanding of possible potential hazards to astronauts and electronic equipment has become a necessity for future lunar explorations. The lunar surface, lacking an atmosphere and global magnetic field therefore directly exposed to solar radiation and solar wind plasma, is electrically charged by the bombardment of solar wind plasma and emission/collection of photoelectrons. Additionally, lunar dust grains can also get charged and levitated from the surface under the influence of the electric field as well as gravity within the plasma sheath. Since the plasma sheath formed near the illuminated lunar surface is dominated by photoelectrons, it is usually referred to as "photoelectron sheath".

In this research, we will focus on resolving the photoelectron sheath structure near lunar surface through numerical simulations. Firstly, we will introduce the fundamental assumptions of our analytic and simulation studies. We will present the derivation of a 1-D semi-analytic model to numerically obtain the quantities of interest as functions of the distance from surface within the photoelectron sheath. Secondly, we will present the numerical simulations with a fully kinetic Finite Difference (FD) Particle-in-Cell (PIC) code to solve the surface charging problem on lunar surface. In this study, we will consider both *Maxwellian* and *Kappa* distribution of solar wind electron velocities. Finally, we will show our current studies on the charged lunar dust lofting and transport under the influence of local electrostatic environment. We will consider both uncoupled and coupled method in the simulations. In uncoupled method, a steady state electric field is obtained through FD-PIC simulations and provided to simulate the charged dust transport, indicting that the charged dust transport does not influence the local electrostatic environment. Whereas in the coupled method, the electrostatic environment and the charged dust transport are simulated simultaneousness, which means the electrostatic environment and the dust transport influence each other during the simulations.

ACKNOWLEDGMENTS

First and foremost, I am extremely grateful to my advisor, Dr. Daoru Han, for his invaluable advice and support during my PhD studies. This dissertation would have never been accomplished without his assistance and dedicated involvement throughout the process.

Next, I would like to thank all members in my dissertation committee, Dr. Xiaoming He, Dr. Serhat Hosder, Dr. Henry Pernicka, and Dr. Guirong Yan. The value of their guidance cannot be overstated. I would also like to thank the previous users and developers of the code utilized in this dissertation, Dr. Yong Cao and Dr. Xiaoming He, for their fundamental work in this study. And I would like to thank all the group members, Dr. Zhangli Hu, Dr. Xinpeng Wei, Mr. Zach Gill, Mr. Blake Folta, Mr. David Lund, Mr. Terence McGarvey, Mr. Joshua Burch, Mr. Nicholas Ernst, and Mr. Alex Lamb, for their kind support.

Last but not least, I would like to give my sincere thanks to my parents , my friends, and all the relatives for their encouragement through my studies.

The work in this dissertation is supported in part by NASA-Missouri Space Grant Consortium through NASA-EPSCoR Missouri, as well as NSF through grant DMS-2111039. The simulations presented here were performed with computing resources provided by the Center for High Performance Computing Research at Missouri University of Science and Technology through NSF grant OAC-1919789.

TABLE OF CONTENTS

Page

LIST OF ILLUSTRATIONS

Figure Page

LIST OF TABLES

1. INTRODUCTION

This section will briefly describe the physics and the mathematical models of the interactions between the plasma and the celestial bodies (i.e., the Moon), and introduce the problems that investigated in our research. In Section 1.1, we will introduce the background of the study in this dissertation. In Section 1.2, we will present the motivations and objectives. The outline of this dissertation will be given in Section 1.3.

1.1. BACKGROUND

In this section, we will introduce the background knowledge of lunar exploration, including lunar surface environment and plasma conditions.

1.1.1. The Lunar Surface Environment. The Moon is directly exposed to solar radiation and solar wind plasma (mostly drifting protons and electrons), due to the lack of global atmosphere and magnetic field. Consequently, the lunar surface is electrically charged caused by the bombardment of solar wind plasma and emission and collection of photoelectrons. Additionally, dust grains on the lunar surface may get charged and levitated from the surface under the influence of the electric field as well as gravity within the plasma sheath. The interactions between the plasma environment and charging/levitation/transport of dust grains near the lunar surface can affect almost all kinds of human or mechanical activities on lunar surface as well as a series of natural process with respect to the surface topography. The related topics have been studied extensively (Abbas *et al.* (2007); Farrell *et al.* (2008b); Fu (1971); Halekas *et al.* (2007, 2011); Nitter *et al.* (1998); Poppe *et al.* (2011); Poppe and Horányi (2010); Poppe (2011); Poppe *et al.* (2012); Stubbs *et al.* (2014); Wang *et al.* (2008, 2016); Willis *et al.* (1973); Zimmerman *et al.* (2016); Zook and McCoy (1991)).

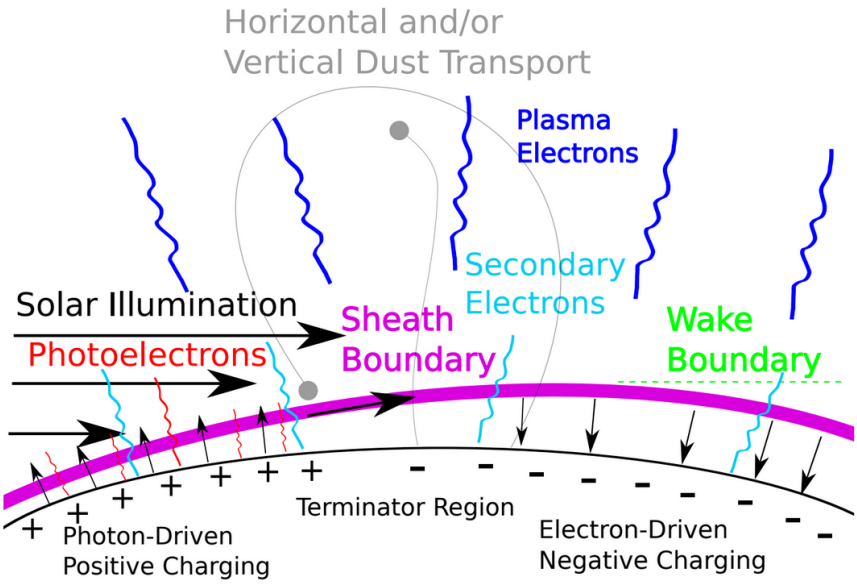

Figure 1.1. Lunar surface charging environment at the terminator region, Han (2015)

Among the potential landing sites for future lunar explorations, the lunar terminator draws the most attention due to the availability of stable solar power, and the possible storage of iced water which can be used as supplies for human activities and power source for mechanical purpose (Farrell *et al.* (2008a); French *et al.* (1991)). However, since the lunar terminator region is the transition region between the sunlit and the shadowed surface, the solar wind and solar radiation directs nearly horizontal to the surface. Therefore, the plasma interactions and charging process are highly complex near the terminator region, as shown in Figure 1.1 (Han (2015)). The charging on lunar surface would change from ion-driven positive charging to electron-driven negative charging over the transition between sunlit and shadow, leading to a strong differential charging on the lunar surface. In addition, the different surface terrains will also contribute to the strong differential charging on the surface, due to the shadows caused by low Sun elevation angle (SEA). Since the plasma sheath formed near the illuminated lunar surface is dominated by photoelectrons, it is usually referred to as "photoelectron sheath."

1.1.2. Plasma Dynamics. The ambient plasma above the lunar surface is considered as a quasi-neutral ionized gas of charged particles interacting with each other under the effects of electric and magnetic fields. The lunar surface that exposed to the ambient plasma collects electrons and ions until it reaches the steady state, where the net current entering and leaving the surface becomes zero. Here we will briefly introduce the plasma dynamics related to the study in this dissertation.

1.1.2.1. Governing equations. The net current on the lunar surface can be expressed as Eq. (1.1).

$$\frac{\mathrm{d}Q}{\mathrm{d}t} = I_{\mathrm{net}} \tag{1.1}$$

where Q is the total charge; t is time; and I_{net} is the net current.

The dynamics of the plasma is governed by the Maxwell's equations, as shown in Eq. (1.2).

$$\begin{aligned} \nabla \cdot \mathbf{B} &= 0 \\ \nabla \times \mathbf{B} &= \mathbf{J}\mu_0 + \frac{1}{c^2}\frac{\partial \mathbf{E}}{\partial t} \\ \nabla \cdot \mathbf{E} &= \frac{\rho}{\varepsilon_0} \\ \nabla \times \mathbf{E} &= \frac{\partial \mathbf{B}}{\partial t} \end{aligned} \tag{1.2}$$

where **B** and **E** represent magnetic and electric field, respectively; **J** is the electric current density; μ_0 is the vacuum permeability; ρ is the charge density; and ε_0 is the vacuum permittivity.

In this dissertation, we focused on the effects of electrostatic interactions, which reduces the above equations to the following form as shown in Eq. (1.3).

$$\nabla \cdot \mathbf{B} = 0$$
$$\nabla \times \mathbf{B} = 0$$
$$\nabla \cdot \mathbf{E} = \frac{\rho}{\varepsilon_0}$$
$$\nabla \times \mathbf{E} = 0 \tag{1.3}$$

Therefore, the electric potential Φ can be obtained by Eq. (1.4).

$$\mathbf{E} = -\nabla\Phi \tag{1.4}$$

And then the electric field $\mathbf{E}$ can be obtained by the Poisson's equation:

$$\nabla \cdot \mathbf{E} = -\nabla \cdot \nabla\Phi = -\nabla^2\Phi = \frac{\rho}{\varepsilon_0} \tag{1.5}$$

In this dissertation, the collision between plasma particles is neglected because the mean free distance is typically greater than the particle dimension, hence the trajectory of each particle with a charge q and velocity $\mathbf{v}$ under the effect of the electromagnetic field is governed by the the Newton's second law

$$m\frac{\mathrm{d}\mathbf{v}}{\mathrm{d}t} = q(\mathbf{E} + \mathbf{v} \times \mathbf{B}) \tag{1.6}$$

The charge density ρ and the current density $\mathbf{J}$ in a volume V can be calculated by Eq. (1.7).

$$\rho = \frac{1}{V}\sum_{i=1}^{N} q_i$$
$$\mathbf{J} = \frac{1}{V}\sum_{i=1}^{N} q_i\mathbf{v}_i \tag{1.7}$$

where subscript i denotes the properties of the i^{th} particle.

The current collection by the lunar surface shows different characteristics depending on the distance over which the charge is collected. In this dissertation, we assumed that such distance is large enough so that the current collection follows the orbital motion limited (OML) condition.

1.1.2.2. Plasma sheath. Debye shielding is one important property of plasma describing the ability of shielding the electric field over a certain length, leading to the quasi-neutral property of the plasma with a length scale λ_D (which is called Debye length). For the charged object inside plasma, the electric field around the object is shield out over a region as thick as several Debye lengths, therefore, the Debye length is one of the most important parameters of plasma dynamics. For a problem with a characteristic length L, when $L \ll \lambda_D$, the charged particles are considered as individual particles controlled by electric field (i.e., electrically uncoupled). When $L \gg \lambda_D$, collective coupling of the charged particles should be considered (i.e., electrically coupled) (Hastings and Garrett (2004)).

1.1.2.3. Photoelectron sheath model. The essential parts of the photoelectron sheath model considered in this dossertation follow the work of Fu (1971) and Nitter *et al.* (1998), but are extended to include the drifting velocity of the solar wind electrons. Similar to the classification in Fu (1971) and Nitter *et al.* (1998), we denote three possible types of potential profiles within the photoelectron sheath: Type A, Type B, and Type C as shown in Figure 1.2. For each sheath type, the population of the electrons are different. The solar wind electron population contains "free solar wind electrons" representing electrons that are able to reach the lunar surface, and "reflected solar wind electrons" representing electrons that are reflected by the potential barrier (if present in the sheath). The photoelectron population contains "free photoelectrons" representing those able to reach the infinity, and "captured photoelectrons" representing those attracted back to the lunar surface.

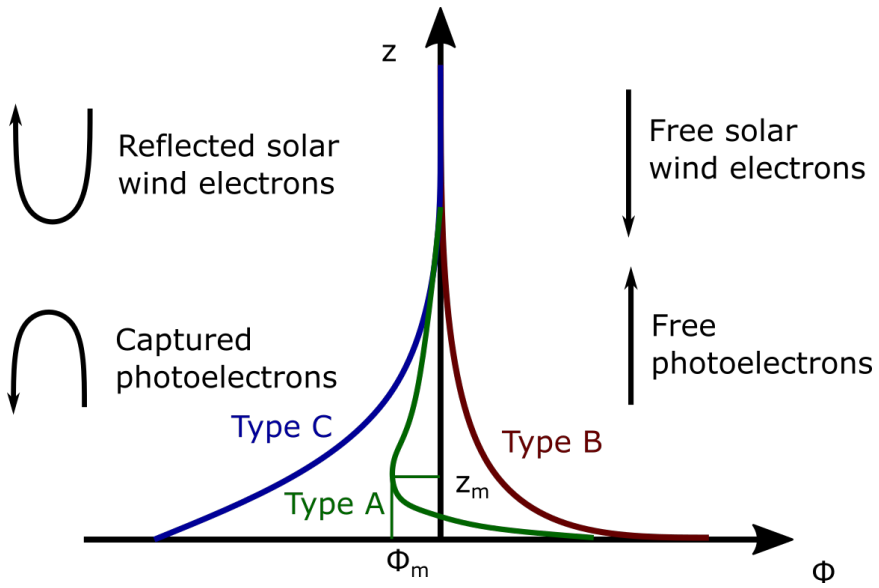

Figure 1.2. Different types of photoelectron sheath

Among these three types of potential profile, Type A is non-monotonic, the curve of Type A will first decrease from the surface to the minimum potential, then increase to the potential at infinity, which is zero. It is believed that non-monotonic potential profiles have lower electrostatic energy than their monotonic counterparts, therefore representing the more stable states (Nitter *et al.* (1998); Poppe (2011)). This hypothesis is then evidenced by measurements from the Lunar Prospector (Poppe *et al.* (2011)) and the ARTEMIS missions (Halekas *et al.* (2011)). Both Type B and Type C are monotonic. The curve of Type B will decrease from the surface potential to zero, whereas Type C will increase from the potential at the surface to zero.

1.1.2.4. Surface charging. As introduced above, the object inside the photoelectron sheath collects electrons and ions until it reaches the steady state. The floating potential of the object at steady state is determined by the electric current entering and leaving the surface. The electric field across the object surface is usually discontinued, due to the different media on two sides of the interface, as shown in Figure 1.3. The electric field flux jump across the interface can be calculated by Eq. (1.8) (Jackson (1999)).

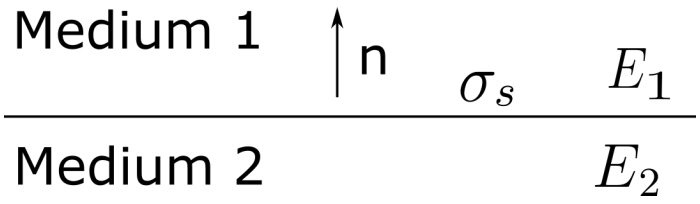

Figure 1.3. Flux jump across the interface

$$\left[\varepsilon\frac{\partial\phi}{\partial\mathbf{n}}\right]\Big|_{\Gamma} = -\left(\varepsilon_2\mathbf{E}_2 - \varepsilon_1\mathbf{E}_1\right)\cdot\mathbf{n} = -\sigma_s \tag{1.8}$$

where **n** is the normal factor from Medium 1 to Medium 2, and σ_s is the surface charge density.

The floating surface potential will then affect the collection of the electric current trough the surface, creating a dynamic interaction between plasma and object surface that can be described by the following equation:

$$\sum I(\phi_s) = 0 \tag{1.9}$$

where I is the collected current by the surface; ϕ_s is the surface potential.

1.2. MOTIVATION AND OBJECTIVES

The study in this dissertation is motivated by the lack of knowledge of the photo-electron sheath and the corresponding effects on various quantities of interests on the lunar surface (surface electric potential, surface electric field, lunar dust transport and levitation mechanism due to the accumulation of electric charge on the dusts, etc.).

The objective of this study is to apply the Finite-Difference (FD) Particle-in-Cell (PIC) code to simulate the surface charging with even and uneven surface terrain on the Moon. The numerical simulations will be validated by comparing the results with the 1-D semi-analytic solutions derived through mathematical approaches.

Through this dissertation, an insight of the potential hazards caused by electric discharge due to large differential electric potential between the lunar surface and the ambient dielectric objects can be provided, which can help improve the safety consideration for the future lunar explorations.

1.3. DISSERTATION OUTLINE

We will first introduce the numerical simulations to reveal the surface charging process and obtain the quantities of interest (electric potential, electric field, charge density, etc.) within a the photoelectron sheath near even lunar surface, and validate the model by running a number of test simulations and comparing the results with the 1-D semi-analytic solutions that we derived with mathematical approaches. Next, we will improve the simulations to include the geometry of even and uneven lunar surfaces (i.e., convex and concave surface) for 2-D and 3-D photoelectron sheath configuration. Then, we will study different scenarios of the charging process near the lunar terminator region, and investigate the charging process on lunar dust and the possible effects of local electrostatic field on the dynamics of lofted charged dust grains, which reveals the mechanism of the levitation and transport of charged lunar dust under the effects of both electrostatic forces and the gravity.

The study in this dissertation will provide important information of the plasma environment near the lunar terminator region, where has been considered as one of the idealist landing locations for the future lunar explorations, due to the stability of the solar power and the potential supply of the iced-water.

This dissertation is consist of seven sections, the details of each section are listed below:

- Section 1 introduces the background knowledge, study motivation, and research objectives of this dissertation.

- Section 2 presents the literature reviews with respect to the study of this dissertation, including numerical simulations of surface charging, surface charging modelings, plasma surface interactions, and levitation and transport of charged lunar dust grains.
- Section 3 introduces the FD-PIC framework which is employed to run simulations in this dissertation.
- Section 4 shows the details of derivation of the 1-D semi-analytic model and the validation of the numerical simulations.
- Section 5 presents the applications of the FD-PIC code on simulating the electrostatic environments with consideration of different electron distributions.
- Section 6 shows the study of the levitation and transport of charged dust near lunar surface through numerical simulations.
- Section 7 concludes the studies in this dissertation and presents the contributions to the corresponding fields of science and engineering, and recommends the future studies.

2. LITERATURE REVIEW

This section presents the literature review of the numerical modeling approaches related to the studies in this dissertation. The literature review will focus on field solving methods, surface charging, surface-plasma interactions, and dust grain transport dynamics. In Section 2.1, we will present the literature review of the methods to build the field solver in our code. In Section 2.2, we will present the literature review of the dust levitation and transport modeling. A brief summary of the literature review in this section will be given in Section 2.3.

2.1. FIELD SOLVERS

The objective of the simulation is to obtain the field information of the electrostatic environment (electric potential, electric field, charge density, etc.) inside the computation domain. For a interface problem, the electrostatic field can be obtained by solving the Poisson's equation with discontinuous coefficients across the interface, as illustrated in Figure 1.3. In this section, we will present a brief review of the methods to build the field solver in the code.

2.1.1. Cartesian Mesh. In simulations, the Cartesian and non-Cartesian mesh structures are usually employed to build the computation domain so that the charge information can be collected on the mesh nodes. The Cartesian mesh divides the computation domain into structured mesh cells and all mesh nodes are regularly distributed with certain distances, therefore brings a number of advantages such as:

- It is easy and computationally cheap to generate the Cartesian mesh even for a large computation domains.

- A number of efficient and widely used field solver methods are available for Cartesian mesh, which simplifies the improvement of the code by implementing the updated algorithms into the existing solver codes.

- For the PIC scheme, the structured Cartesian mesh is quite efficient in simulations because searching and locating a particle in structured mesh is much easier compared with that in the non-Cartesian mesh.

2.1.2. Non-Cartesian Mesh. For an object or a surface with non-regularly shaped boundary, a regular mesh is not able to fit the body therefore cannot be used in the simulations. In such situation, a non-Cartesian body-fitting mesh is necessary to fit the boundary of the object or the surface. Numerical schemes, such as Finite Difference, Finite Element, and Finite Volume can be used to solve the governing equations on mesh nodes of such body-fitting mesh with second order accuracy (Bramble and King (1996); Eastwood *et al.* (1995)).

Though the body-fitting mesh is widely used in solving complex boundary problems with high accuracy, it is associated with several disadvantages listed below:

- It is difficult to generate a body-fitting mesh to fit a complex shipped object or surface in a computation domain.

- It is computationally expensive to run simulations with complex body-fitting mesh. Though a reduction of mesh number can reduce the computation cost, it reduces the accuracy of the simulation as well.

- It is not efficient in cooperation with the PIC scheme, because searching and locating a particle in unstructured body-fitting mesh, which needs to be done in each iteration for all simulation particles, is highly computational expensive (Hewett (1997)).

With the considered advantages, we chose to use the structured Cartesian mesh in our simulations. In the following sections we will present a review of the applications of the Finite Difference scheme with Cartesian mesh in simulations.

2.2. A REVIEW OF DUST LEVITATION AND TRANSPORT MODELING

In this section, we will review some important studies and investigations on lunar dust levitation and transport regarding lunar exploration, lunar surface charging, and dust transport dynamics.

2.2.1. A Review of Lunar Exploration. The goal of sustainable human presence on the Moon has been made explicitly, therefore with the growing interest of lunar exploration, an increasing demand of deep understanding of in situ activities on lunar surface has shown in various fields of study. Unlike the mechanical activities on Earth, every simple process could encounter a series of issues on the Moon. Recently, more attentions have been given to the study on how to safely and efficiently achieve physical explorational purposes on lunar surface, i.e., lunar surface landing (Jiang *et al.* (2017)); transportation of lunar regolith for construction purpose (Kawamoto (2020)), etc. Therefore, a better understanding of dust charging mechanism is a necessity to avoid potential hazards during in situ activities on the lunar surface.

Woodcock et al. collected studies from NASA's contractor contributors and presented a report of the application of automation and robotics on lunar surface operations (Woodcock (1990)). The report was to broaden the assessment of the operational problems that could be encountered during the process of expanding human presence into the solar system, and to provide possible solutions. The study covered the assembly, emplacement, checkout, operation and maintenance of equipment on planetary surface with the consideration of three efforts, which are 1) conceptual design of required surface system, 2) assessments of contemporary developments in robotics, and 3) quantitative analysis of

machine and human tasks. The studies introduced in the report can be considered as the starting point of more extensive engineering analysis of the issues encountered during planetary explorations.

Reiss et al. introduced an insulation method that can be applied for designing the oven which is used to heat up lunar soil and extract volatiles during lunar missions (Reiss *et al.* (2017)). According to the authors, the power needed to heat up lunar soil sample to the target temperature (1200 °C) increases exponentially with the sample size, therefore in order to keep the demand power under the acceptable level, the authors proposed an insulation method regarding carbon aerogel or equivalent thermal properties for ovens, and conducted physical experiments and simulations to validate the insulation design. The validation showed that the oven design presented by the authors can reach the target heating temperature for thermal extraction with a low power demand, which meets the energy requirement.

Jiang et al. investigated the mechanical behavior of lunar soil for construction and landing process (Jiang *et al.* (2017)). The authors conducted a series of plate load tests on Tongji-1 lunar soil simulant to study the bearing capacity of lunar soil during landing process, and compared the experimental results with numerical results obtained with Terzaghi and modified Terzaghi methods. The comparison showed that the bearing behavior of Tongji-1 lunar soil simulant was overpredicted by Terzaghi and overpredicted by modified Terzaghi method. The experimental data provided in this study is expected to contribute to a better understanding of lunar ground stability for construction and landing process.

Metzger et al. developed a computer model to investigate the thermal extraction of volatiles from lunar and asteroid regolith (Metzger *et al.* (2020)). The authors presented the possibility of obtaining water through injecting heat into the lunar subsurface and collecting

the vapor or liquid that reach the surface. The thermal volatile extraction model introduced in their study was able to provide thermal conductivity and heat capacity of lunar soil with an excellent agreement with experimental data.

Kawamoto studied the in situ resource utilization with lunar regolith on the Moon, and presented a vibration transport system which can be used to transport lunar regolith more easily and efficiently (Kawamoto (2020)). According to the author, lunar regolith (whose composition includes metals, oxygen, and helium 3) is one of the ideal substances to support human activities during lunar missions, from constructing buildings to serving as energy source. The vibration transport system introduced by the author is simple, reliable, and energy efficient, therefore is considered suitable for use on lunar surface.

Gawronska et al. investigated the geologic features near the lunar south pole through photogeological analysis, in order to target potential extravehicular activities on lunar surface (Gawronska *et al.* (2020)). The author concluded that the topography in the lunar south pole is complicate, however a rover-assisted extravehicular activities will allow astronauts to traverse slopes and access to distant areas of interest.

Austin et al. presented a study of Robotic Lunar Surface Operations 2 (RLSO2), which is conducted by US experts with backgrounds on mission design, robotic surface operations, autonomy, in situ resource utilization, operations analysis, etc. (Austin *et al.* (2020)). In addition to the original study (RLSO) proposed in 1990 (Woodcock (1990)), the updated study uses contemporary tools such as CAD engineering and numerical operations model. The authors give the overviews of current understandings of lunar operations (assumptions, methodology, element design, etc.), and reveal some challenging questions which require physical experiments and demonstrations on lunar surface.

2.2.2. A Review of Lunar Surface Charging. To investigate the lunar surface charging process, Farr et al. introduced a dust mitigation technology utilizing an electron beam to shed dust off from surfaces (Farr *et al.* (2020)). The dust issues have been studied ever since it was observed during the Apollo missions (Godwin (2002)). The lofted dust

grains caused by natural process and human activities can stick to almost any surfaces under the effect of electrostatic forces, causing dust hazards including seal failure, clogging of equipment, vision obscuration, etc. The authors conducted experiments with fine size lunar dust simulant JSC-1A, and concluded that with their method, the overall cleanliness can reach 75 ~ 85% at ~100 s with an electron beam energy ~230 eV.

Żbik presented a study of morphological similarities between lunar regolith fractions and interplanetary dust particles (IDPs) collected in Earth's stratosphere (Żbik (2020)). Through comparing the morphology features of IDPs and lunar dust, the author concluded that even though it is not stated that the lunar dust grains can be presence in Earth by the study of morphology similarities, it is highly likely that the lunar dust ejected from the Moon have been grazed by Earth.

2.2.3. A Review of Dust Transport Dynamics. Investigating levitation and transport of lunar dust will provide important information to prevent the potential lunar dust hazard, highlight safety concerns for future lunar missions.

According to McCoy and Criswell (1974), a model was constructed to study the light scattering caused by lunar dust above the lunar surface. With brightness observed during Apollo missions, the dust size was chosen as 0.1×10^{-6} m with a number density of 1.0×10^{-1} cm^{-3} at 1 km, 1.0×10^{-2} cm^{-3} at 10 km, and 1.0×10^{-5} to 1.0×10^{-6} cm^{-3} at 100 to 200 km. The model works well with the presence of 1.0×10^{-3} cm^{-3} lunar dust density along the interface of shadow and sunlight region, which was proved to be possible by Gault *et al.* (1963) and Hartung *et al.* (1972). In a recent study, Sharma et al. analyzed the LADEE-UVS data and provided constraints on dust density at low altitude above lunar surface (Sharma *et al.* (2021)). According to their study, lunar dust with a size ranging from 0.3 to 1.0×10^{-6} m has an upper limit on density of ~140 m^{-3} closer to the lunar surface.

By collecting and reviewing the reports of Apollo Program, Wagner stated the details of the lunar dust issues and possible solutions (Wagner (2006)). Through this study, the author presented that though lunar dust could cause significant issues during lunar explo-

ration missions, the dust itself could be managed by good practices in engineering designs. The author recommended that in order to achieve successful lunar surface explorations, the lunar dust effects have to be considered while designing every system and interface that contact with lunar dust.

Christoffersen et al. studied the lunar dust effects on spacesuit systems (Christoffersen and Lindsay (2009)). Spacesuit protects astronaut from the critical environment on the Moon, therefore any potential damage to spacesuit should be considered and studied on the designing stage. The target sample of this study was those suits worn by astronauts for extravehicular activities during Apollo missions, which contacted with lunar dust directly. The Scanning Electron Microscopy (SEM) techniques was utilized to study the level of contamination, abrasion, function failure of spacesuit due to lunar dust. Through their study, the authors concluded that lunar dust is highly likely the reason of progressive and accelerated fabric wear of spacesuits. The penetration ability of lunar dust would likely contaminate and accelerate wear in the underlying fabric layers. On the other hand, there was not a measurably increased wear or abrasion in the gloves, even though these gloves were also worn in the dusty environment.

Baiden et al. discussed the possibility of building a permanent outpost on the moon and gave suggestions on the construction of such outpost with the consideration of current available technologies (Baiden *et al.* (2010)). According to their studies, an ideal lunar outpost would be constructed underground to protect astronauts, plants, and animals from significant environmental hazards including lunar radiation, temperature extremes, solar flares, etc. The in situ resources for constructions would be obtained through underground mining on the moon with automated or teleoperated control from earth. The authors concluded that the underground lunar outpost is necessary for long term human activities and it is feasible to be constructed with existing technologies.

Once the upward electrostatic force acting on the dust becomes greater than the gravity, the charged dust will be lofted from the lunar surface and motion will be governed by the surrounding electric field as well as the gravity. Therefore, to study the dynamics of charged dust, it is necessary to have a better understanding of both the charge accumulation on the dust and the structure of the electrostatic field around the dust grain. Hartzell et al. investigated the dynamics of charged dust lofting on celestial bodies and presented that the cohesion between the charged dust grains shows an important effect on determining the electrostatic force required to loft the dust (Hartzell and Scheeres (2011); Hartzell *et al.* (2013)). The authors assumed that the charge accumulation follows the Gauss' Law and provided a theoretical model which considered the cohesive and the gravitational force acting on the dust, and be able to calculate the electric field intensity to loft the dust. The theory in their studies has been validated by the corresponding experiments performed by the authors.

To identify the equilibrium height of the lofted charged dust, a numerically modeled nonmonotonic potential sheath was studied by Hartzell and Scheeres (Hartzell and Scheeres (2013)). Through their study, the authors concluded that the initial velocity which influences the charged dust lofting is controlled by the dust size. Their study provided a contribution to the evaluation of the importance of the charged dust lofting.

Except natural loft, the dust can also be lofted by human or construction activities. Morris et al. studied the dust transport caused by engine plume impingement (Morris *et al.* (2016)). According to their study, the dust number density within a 10 m height from lunar surface will range from 1.0×10^5 to 2.0×10^8 m^{-3} caused by the plume of one engine hovering from 3 to 20 m from the lunar surface.

Kuznetsov et al. introduced the development and applications of a software toolkit called Spacecraft Plasma Interact Software (SPIS) on simulating the electric charging on lunar dust and lunar lander, and the transport and deposition of the charged dust on the lander surface (Kuznetsov *et al.* (2018)). To simulate the dynamics of charged lunar dust, a

modification called SPIS-DUST can be used to estimate the influence of the lunar lander on the local electric environment and dust lofting near the lunar surface. The authors presented that the code can be used to gain a deeper understanding and interpretation of the dust measurements.

Carroll et al. studied the range of motion of charged dust grains by experimentally measuring the initial launch velocity associated with the dust size (Carroll *et al.* (2020)). According to their studies, the launch velocity is inversely proportional to the dust radius. For dust simulants with irregular shapes, a large velocity distribution was found even for dust grains with similar sizes, due to the variable cohesive force between dust grains. Whereas for regular shaped dust grains (silica microsphere was used as test sample in their experiments), the greatest launch velocities were tested much lower compared with irregularly shaped dust. The launch angle was found usually laying between 45° and 135° relative to the surface. Through their research, the authors concluded that the dust shape has a considerable effect on dust levitation and transport, due to the various cohesive force between dust grains and the corresponding electric repulsive force to overcome the cohesive force.

Rhodes et al. studied the triboelectric charging and grounding of a drill during a drilling process in the shadow region on the lunar surface (Rhodes *et al.* (2020)). The authors gave a first analytic estimation of the accumulated voltage generated by electrical grounding of the drill bit while drilling on the lunar regolith. According to their studies, the net voltage caused by triboelectric interaction could be high enough to trigger a potential hazard for astronauts and electric equipment. In their study, two possible solutions were provided by the authors: 1) A sun-facing surface outside the shadow region, and 2) A portable UV ionization lamp. It was concluded that both of these two solutions would work with disadvantages (requirement of a substantial initial infrastructure setup for sun-facing

surface, and a power source and an active system for the portable UV lamp). The authors also pointed out that the triboelectric charging is sensitive to material structure, geology, geometry, motion and surrounding environment.

The issues due to lunar dust were collected and evaluated by Corazzari *et al.* (2021). The adverse effect of lunar dust has become one of the major concerns for lunar exploration since the first Apollo mission. A series of engineering failures (visual obscuration, false instrument readings, thermal control problems, etc.) can be caused by lunar dust, due to its distinct physical-chemistry features. Furthermore, the lunar dust was also found to be toxic and able to cause health issues to astronauts through inhalation. The urgency of studying the lunar dust led to the formation of Lunar Airborne Dust Toxicity Advisory Group (LADTAG) in 2005, organized by NASA. Through their studies, the author concluded that in order to expand the understanding of the toxicological properties, the designing of next generation simulant of lunar dust is urgently needed, which should be considering the long-term exposure of astronauts.

2.3. SUMMARY

We presented a literature review of numerical modelings and analytic approaches focusing on surface charging, surface-plasma interactions, and dust grain transport dynamics. We introduced the difference between Cartesian and non-Cartesian mesh, and the reasons and benefits of using Cartesian mesh in this dissertation. We also investigated the mechanism behind the charged dust levitation and transport within the photoelectron sheath, and reviewed the studies on dust transport dynamics with considerations of the local electrostatic environment.

3. THE FINITE DIFFERENCE PARTICLE IN CELL FRAMEWORK

In this section, the Finite Difference (FD) Particle-in-Cell (PIC) scheme employed in the our code will be introduced. Specifically, the FD method is applied in the solver code to solve the PDE problem in each iteration in the simulations, whereas the PIC method is used in simulating the particle motion and acquiring field information in the computation domain. In Section 3.1, we will introduce the details of the FD method. In Section 3.2, we will present the application of the PIC method in the simulations. The combination of these two methods, which is known as the FD-PIC method, will be discussed in Section 3.3. A brief summary of the study in this section will be given in Section 3.4.

3.1. FINITE DIFFERENCE SCHEME

The Finite Difference (FD) scheme is one of the most widely used methods in solving boundary value problems by approximating the derivatives in differential equations with Finite Difference formulas. The 3-D FD scheme has been extensively used to solve the 3-D numerical simulation problems due to its flexibility in writing equations and the compactivity with other functions in existing codes written by different languages. Since we are using structured meshes to build the computation domain with known lengths between the mesh nodes, the 3-D FD scheme is considered as an appropriate method for writing the solver functions in the codes with accepted accuracy.

3.1.1. Governing Equations. In this section, the details of the 3-D FD equations and their applications in the simulations will be introduced. In our current codes, the FD method is employed in the solver code to solve the field information, such as electric potential, electric field, and charge density. The electric potential is obtained from the electric field by solving the governing equation as shown in Eq. (3.1).

$$\oint \varepsilon \mathbf{E} \vec{n} dA = \rho V + \sigma A \tag{3.1}$$

And the electric field can be obtained from the Poisson's equation derived by Gauss' Law, which is shown in Eq. (3.2).

$$\begin{aligned} \mathbf{E} &= -\nabla \Phi \\ \nabla \cdot \mathbf{E} &= \frac{\rho}{\varepsilon} \end{aligned} \tag{3.2}$$

When expanding Eq. (3.1) with the FD method, we need to consider the effect of the surface charge and surface area (i.e., the second term on right hand side of Eq. (3.1)). Specifically, we need to identify the location of the mesh node on which the Poisson's equation is solved. The possible locations of the mesh nodes are listed below:

- The mesh node is located inside an object.
- The mesh node is located on the surface of the object.
- The mesh node is located on the intersection of two surfaces of the object.
- The mesh node is located on the vertex of the object.
- The mesh node is located outside the object.

3.1.2. Expansion of Governing Equations. When the mesh node is located inside or outside the object in the computation domain as shown in Figure 3.1, the expanded equation of Eq. (3.1) with the Finite Difference method is obtained as Eq. (3.3).

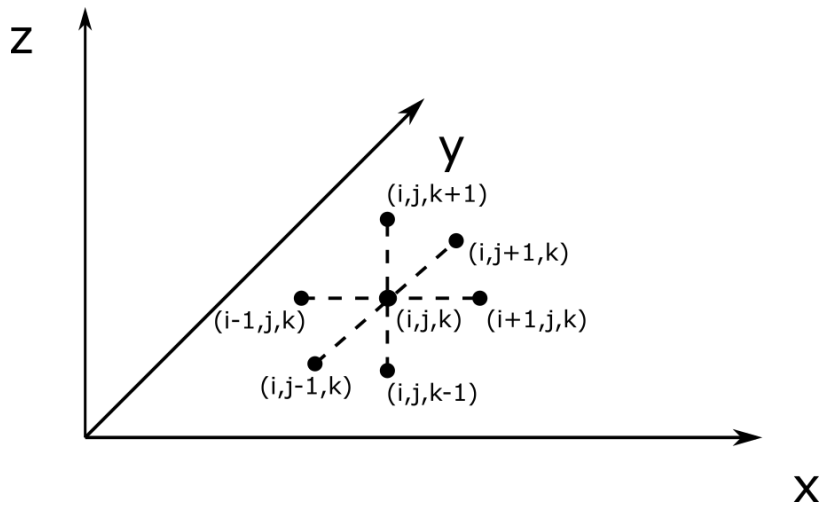

Figure 3.1. A mesh node located inside the computation domain

$$
\begin{aligned}
&- \varepsilon\phi_{(i-1,j,k)}\Delta y^2\Delta z^2 - \varepsilon\phi_{(i+1,j,k)}\Delta y^2\Delta z^2 \\
&- \varepsilon\phi_{(i,j-1,k)}\Delta x^2\Delta z^2 - \varepsilon\phi_{(i,j,k+1)}\Delta x^2\Delta z^2 \\
&- \varepsilon\phi_{(i,j,k-1)}\Delta x^2\Delta y^2 - \varepsilon\phi_{(i,j,k+1)}\Delta x^2\Delta y^2 \\
&+ 2\varepsilon\phi_{(i,j,k)}(\Delta x^2\Delta y^2 + \Delta x^2\Delta z^2 + \Delta y^2\Delta z^2) \\
&= \rho\Delta x^2\Delta y^2\Delta z^2
\end{aligned} \tag{3.3}
$$

where ε is the permittivity inside or outside of the object, and ρ is the volume density.

It should be noted that the expanded equation for mesh nodes located inside or outside of the object are the same, the difference is the permittivity ε in the equation. When the mesh node is inside the object, the object permittivity ε_{o} should be used in the equation. When the mesh node is outside the object, the environment permittivity ε_{e} instead should be used in the equation.

When the mesh node is located on the object surface, the difference of the permittivity between the object and the environment needs to be considered. The surface charge density should also be taken into account. There are in total three possible conditions for the mesh node located on the object surface: 1) on X-Y surface of the object; 2) on Y-Z

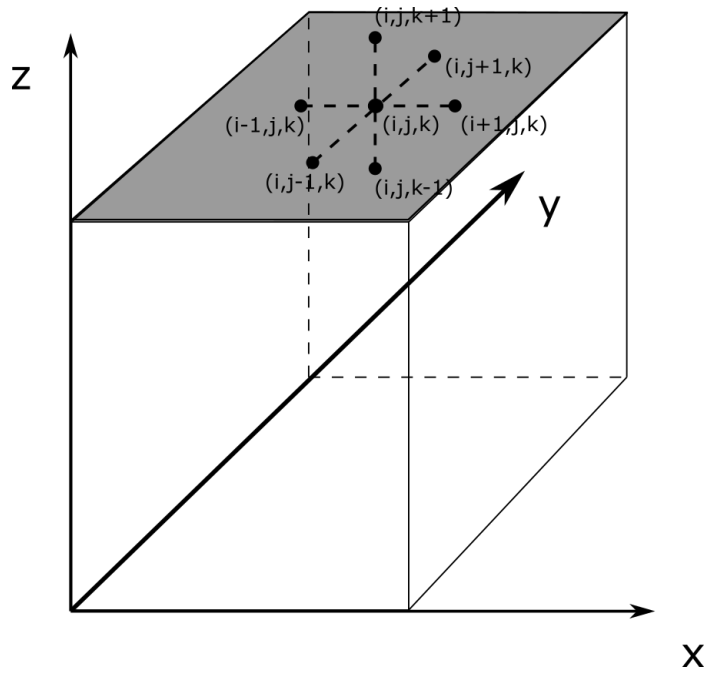

Figure 3.2. Mesh node located on X-Y surface

surface of the object; and 3) on X-Z surface of the object. The locations of such mesh node and the surrounding mesh nodes, which will be used to expand the Finite Difference equation Eq. (3.1), are shown in Figures 3.2 - 3.4.

Equations (3.4) - (3.6) show the expanded equations for the mesh nodes on X-Y, Y-Z, X-Z surfaces, respectively.

$$
\begin{aligned}
&-\frac{(1+\varepsilon)}{2}\Delta y^2\Delta z^2\phi_{(i+1,j,k)}-\frac{(1+\varepsilon)}{2}\Delta x^2\Delta z^2\phi_{(i,j+1,k)}\\
&-\Delta y^2\Delta z^2\phi_{(i,j,k+1)}+(1+\varepsilon)(\Delta y^2\Delta z^2+\Delta x^2\Delta z^2+\Delta y^2\Delta z^2)\phi_{(i,j,k)}\\
&-\frac{(1+\varepsilon)}{2}\Delta y^2\Delta z^2\phi_{(i-1,j,k)}-\frac{(1+\varepsilon)}{2}\Delta x^2\Delta z^2\phi_{(i,j-1,k)}\\
&-\varepsilon\Delta x^2\Delta z^2\phi_{(i,j,k-1)}=\Delta x^2\Delta y^2\Delta z^2\rho+\Delta x^2\Delta y^2\Delta z\sigma
\end{aligned}
\tag{3.4}
$$

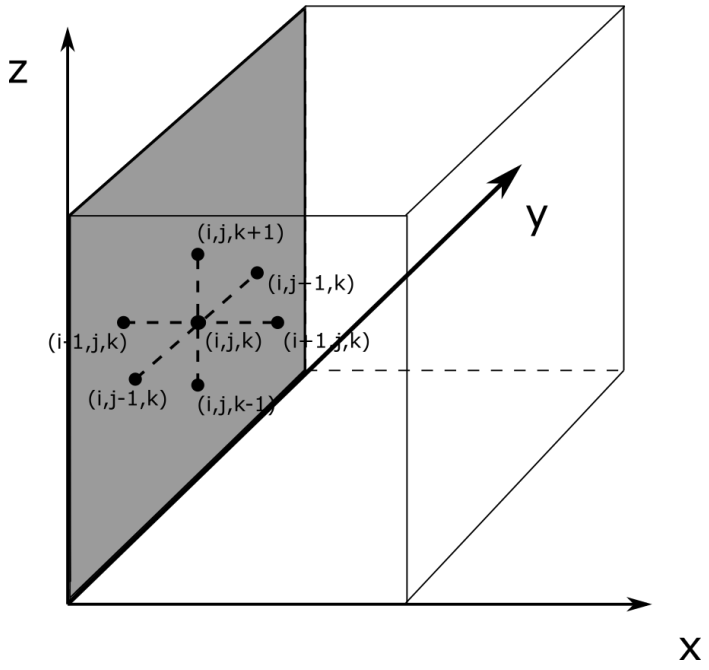

Figure 3.3. Mesh node located on Y-Z surface

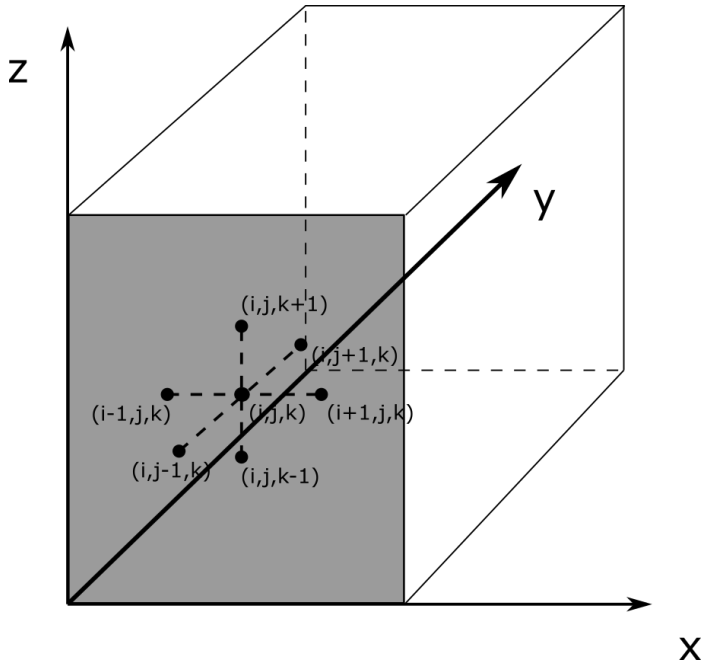

Figure 3.4. Mesh node located on X-Z surface

$$
\begin{aligned}
&-\varepsilon\Delta y^2\Delta z^2\phi_{(i+1,j,k)} - \frac{(1+\varepsilon)}{2}\Delta x^2\Delta z^2\phi_{(i,j+1,k)} \\
&-\frac{(1+\varepsilon)}{2}\Delta y^2\Delta z^2\phi_{(i,j,k+1)} + (1+\varepsilon)(\Delta y^2\Delta z^2 + \Delta x^2\Delta z^2 + \Delta y^2\Delta z^2)\phi_{(i,j,k)} \\
&-\Delta y^2\Delta z^2\phi_{(i-1,j,k)} - \frac{(1+\varepsilon)}{2}\Delta x^2\Delta z^2\phi_{(i,j-1,k)} \\
&-\frac{(1+\varepsilon)}{2}\Delta x^2\Delta z^2\phi_{(i,j,k-1)} = \Delta x^2\Delta y^2\Delta z^2\rho + \Delta x\Delta y^2\Delta z^2\sigma
\end{aligned} \tag{3.5}
$$

$$
\begin{aligned}
&-\frac{(1+\varepsilon)}{2}\Delta y^2\Delta z^2\phi_{(i+1,j,k)} - \varepsilon\Delta x^2\Delta z^2\phi_{(i,j+1,k)} \\
&-\frac{(1+\varepsilon)}{2}\Delta y^2\Delta z^2\phi_{(i,j,k+1)} + (1+\varepsilon)(\Delta y^2\Delta z^2 + \Delta x^2\Delta z^2 + \Delta y^2\Delta z^2)\phi_{(i,j,k)} \\
&-\frac{(1+\varepsilon)}{2}\Delta y^2\Delta z^2\phi_{(i-1,j,k)} - \Delta x^2\Delta z^2\phi_{(i,j-1,k)} \\
&-\frac{(1+\varepsilon)}{2}\Delta x^2\Delta z^2\phi_{(i,j,k-1)} = \Delta x^2\Delta y^2\Delta z^2\rho + \Delta x^2\Delta y\Delta z^2\sigma
\end{aligned} \tag{3.6}
$$

When the mesh node is located on the intersection of two surfaces, the possible locations for such node are shown in Figures 3.5 - 3.7. Again, we need to consider the object permittivity and surface charge density for each condition when expanding Eq. (3.1). The corresponding expanded equations for mesh nodes on X, Y, and Z intersections can be found in Eqs. (3.7), (3.8), and (3.9), respectively.

$$
\begin{aligned}
&-(\frac{1}{4}\varepsilon + \frac{3}{4})\Delta y^2\Delta z^2\phi_{(i+1,j,k)} - \Delta x^2\Delta z^2\phi_{(i,j+1,k)} \\
&-\Delta x^2\Delta y^2\phi_{(i,j,k+1)} + (1+\varepsilon)(\Delta y^2\Delta z^2 + \Delta x^2\Delta z^2 + \Delta y^2\Delta z^2)\phi_{(i,j,k)} \\
&-(\frac{1}{4}\varepsilon + \frac{3}{4})\Delta y^2\Delta z^2\phi_{(i-1,j,k)} - (\frac{1}{2}\varepsilon + \frac{1}{2})\Delta x^2\Delta z^2\phi_{(i,j-1,k)} \\
&-(\frac{1}{2}\varepsilon + \frac{1}{2})\Delta x^2\Delta y^2\phi_{(i,j,k-1)} = \Delta x^2\Delta y^2\Delta z^2\rho + \frac{1}{2}(\Delta x^2\Delta y\Delta z^2 + \Delta x^2\Delta y^2\Delta z)\sigma
\end{aligned} \tag{3.7}
$$

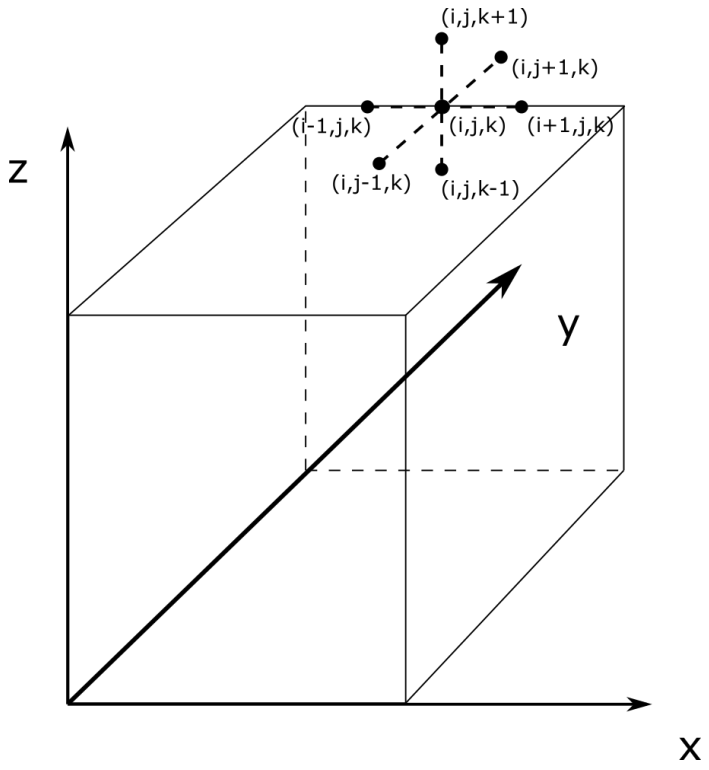

Figure 3.5. Mesh node located on X edge

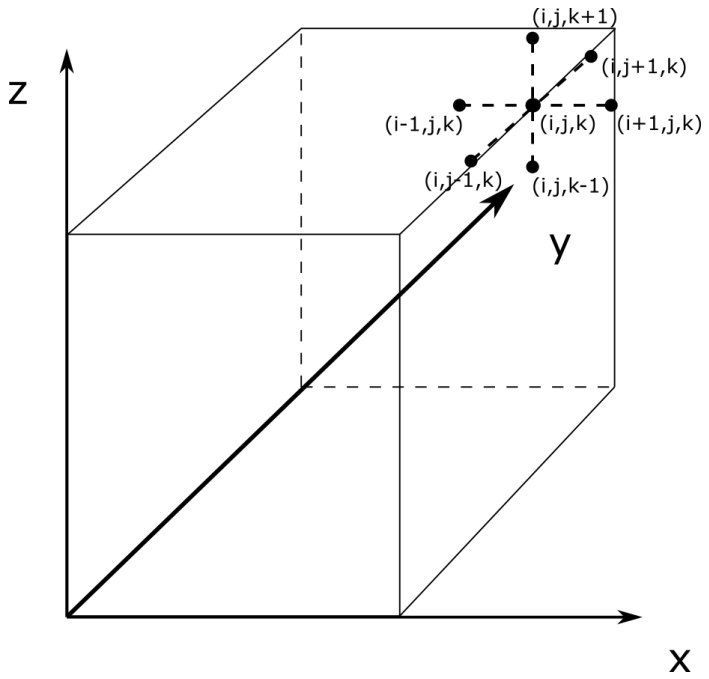

Figure 3.6. Mesh node located on Y edge

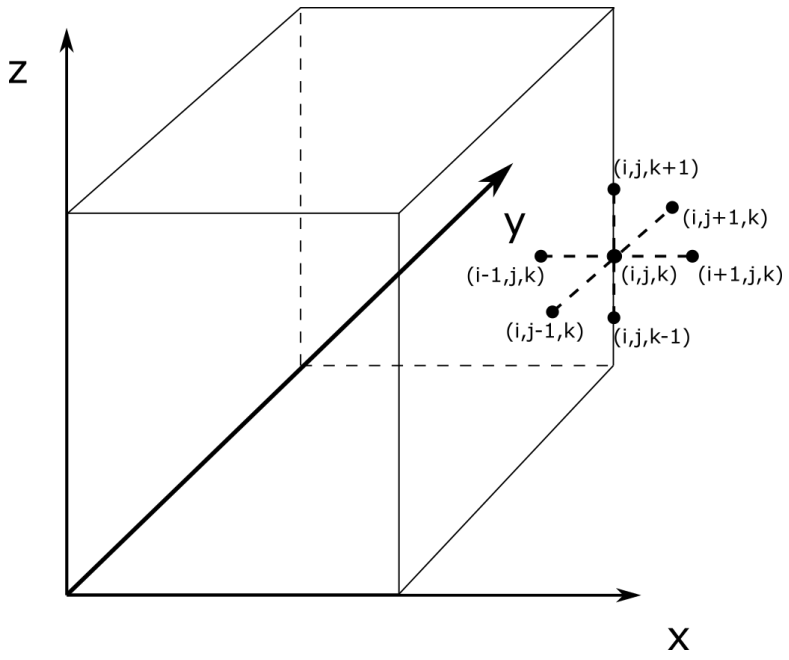

Figure 3.7. Mesh node located on Z edge

$$
\begin{aligned}
&-\Delta y^2\Delta z^2\phi_{(i+1,j,k)} - (\frac{1}{4}\varepsilon+\frac{3}{4})\Delta x^2\Delta z^2\phi_{(i,j+1,k)}\\
&-\Delta x^2\Delta y^2\phi_{(i,j,k+1)} + (1+\varepsilon)(\Delta y^2\Delta z^2+\Delta x^2\Delta z^2+\Delta y^2\Delta z^2)\phi_{(i,j,k)}\\
&-(\frac{1}{2}\varepsilon+\frac{1}{2})\Delta y^2\Delta z^2\phi_{(i-1,j,k)} - (\frac{1}{4}\varepsilon+\frac{3}{4})\Delta x^2\Delta z^2\phi_{(i,j-1,k)}\\
&-(\frac{1}{2}\varepsilon+\frac{1}{2})\Delta x^2\Delta y^2\phi_{(i,j,k-1)} = \Delta x^2\Delta y^2\Delta z^2\rho + \frac{1}{2}(\Delta x\Delta y^2\Delta z^2+\Delta x^2\Delta y^2\Delta z)\sigma
\end{aligned}
\tag{3.8}
$$

$$
\begin{aligned}
&-\Delta y^2\Delta z^2\phi_{(i+1,j,k)} - \Delta x^2\Delta z^2\phi_{(i,j+1,k)}\\
&-(\frac{1}{4}\varepsilon+\frac{3}{4})\Delta x^2\Delta y^2\phi_{(i,j,k+1)} + (1+\varepsilon)(\Delta y^2\Delta z^2+\Delta x^2\Delta z^2+\Delta y^2\Delta z^2)\phi_{(i,j,k)}\\
&-(\frac{1}{2}\varepsilon+\frac{1}{2})\Delta y^2\Delta z^2\phi_{(i-1,j,k)} - (\frac{1}{2}\varepsilon+\frac{1}{2})\Delta x^2\Delta z^2\phi_{(i,j-1,k)}\\
&-(\frac{1}{4}\varepsilon+\frac{3}{4})\Delta x^2\Delta y^2\phi_{(i,j,k-1)} = \Delta x^2\Delta y^2\Delta z^2\rho + \frac{1}{2}(\Delta x\Delta y^2\Delta z^2+\Delta x^2\Delta y\Delta z^2)\sigma
\end{aligned}
\tag{3.9}
$$

When the mesh node is located on the intersection of three surfaces (vertex node) as shown in Figure 3.8, the expanded equation after taking into account of the permittivity and the surface charge density is shown in Eq. (3.10). It should be noticed that Eq. (3.10) is for the vertex node on the intersection of X_{max}, Y_{max}, and Z_{max} surfaces, the expanded equations on other vertex nodes are different, however can be obtained in a similar way.

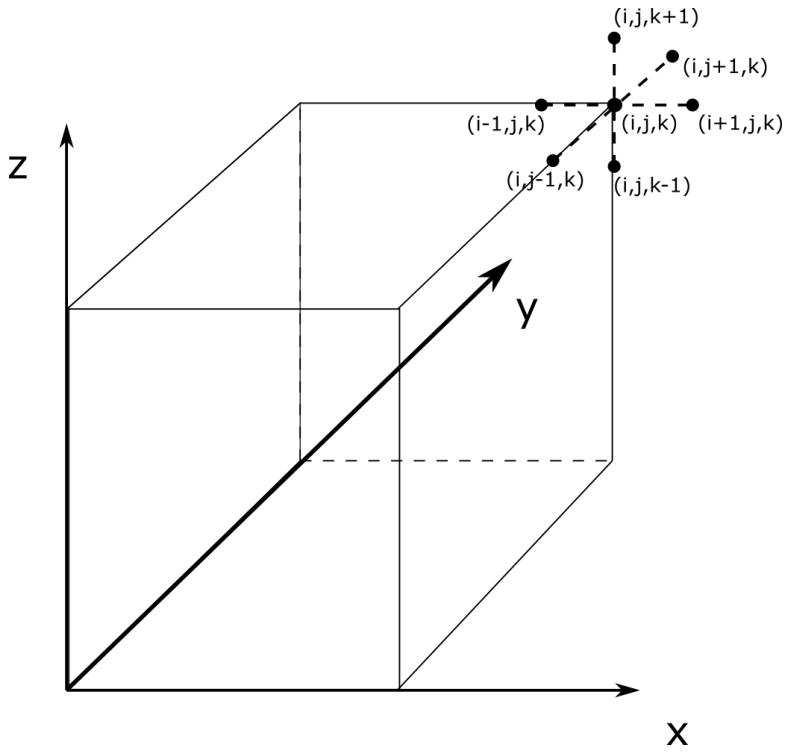

Figure 3.8. Mesh node on object vertex

$$
\begin{aligned}
&- \Delta y^2\Delta z^2\phi_{(i+1,j,k)} - \Delta x^2\Delta z^2\phi_{(i,j+1,k)} - \Delta x^2\Delta y^2\phi_{(i,j,k+1)} \\
&+ (\frac{7}{4}\Delta x^2\Delta y^2 + \varepsilon\frac{1}{4}\Delta x^2\Delta y^2 + \frac{7}{4}\Delta x^2\Delta z^2 + \varepsilon\frac{1}{4}\Delta x^2\Delta z^2 + \frac{7}{4}\Delta y^2\Delta z^2 \\
&+ \varepsilon\frac{1}{4}\Delta y^2\Delta z^2)\phi_{(i,j,k)} + (-\frac{3}{4}\Delta y^2\Delta z^2 - \varepsilon\frac{1}{4}\Delta y^2\Delta z^2)\phi_{(i-1,j,k)} \\
&+ (-\frac{3}{4}\Delta x^2\Delta z^2 - \varepsilon\frac{1}{4}\Delta x^2\Delta z^2)\phi_{(i,j-1,k)} + (-\frac{3}{4}\Delta x^2\Delta y^2 \\
&- \varepsilon\frac{1}{4}\Delta x^2\Delta y^2)\phi_{(i,j,k-1)} = \Delta x^2\Delta y^2\Delta z^2\rho + \frac{1}{2}(\Delta x^2\Delta y\Delta z^2 + \Delta x\Delta y^2\Delta z^2)\sigma
\end{aligned}
\tag{3.10}
$$

3.2. PARTICLE-IN-CELL SCHEME

In this dissertation, a standard numerical scheme called Particle-in-Cell (PIC) is utilized to simulate the transport dynamics of the charged particles. With the PIC scheme, the field information and particle trajectories in the simulations can be solved self-consistently. The computation domain is consist of Cartesian mesh cells with certain dimensions. The charge information from each charged particle is stored on the surrounding mesh nodes, which will then be used in the solver code to calculate field information, such as electric potential, electric field, and electrostatic force.

3.2.1. Charge Scatter. The quantity of the net charge stored on the mesh nodes are scaled with the consideration of the length between the particle and the mesh node, as well as the total number of the injected simulation particles, to ensure the calculated field information are not affected by the absolute quantity of injected particles in each iteration. The description of the scaling process is shown in Figure 3.9(b).

A sketch to describe the PIC charge scattering process in a 2-D scheme is shown in Figure 3.9(a). The total charge of a particle (located at N(x, y)) is represented by the area of the cell, $A_1 = l_x \cdot l_y$. The charge quantity that stored on each surrounding mesh node is scaled by the ratio of the square area on the opposite direction of the particle to the total area of the mesh cell. e.g., in Figure 3.9(a), the total charge of the particle located at N(x, y) is represented by A_1, the charge that should be distributed to the node N(i, j) is calculated as $\rho_{i,j} = a_{i,j}/A_1$ where $a_{i,j} = (x_{i+1} - x)(y_{j+1} - y)$.

3.2.2. Field Solve. After the charge from all simulation particles has been stored on the mesh nodes, the solver code will be ran to solve the field information (electric potential, electric field, etc.) on the mesh nodes by solving the Poisson's equation. The FD scheme introduced in Section 3.1 was employed to build the solver code. The details of the field solving process will be introduced below in Section 4.2.

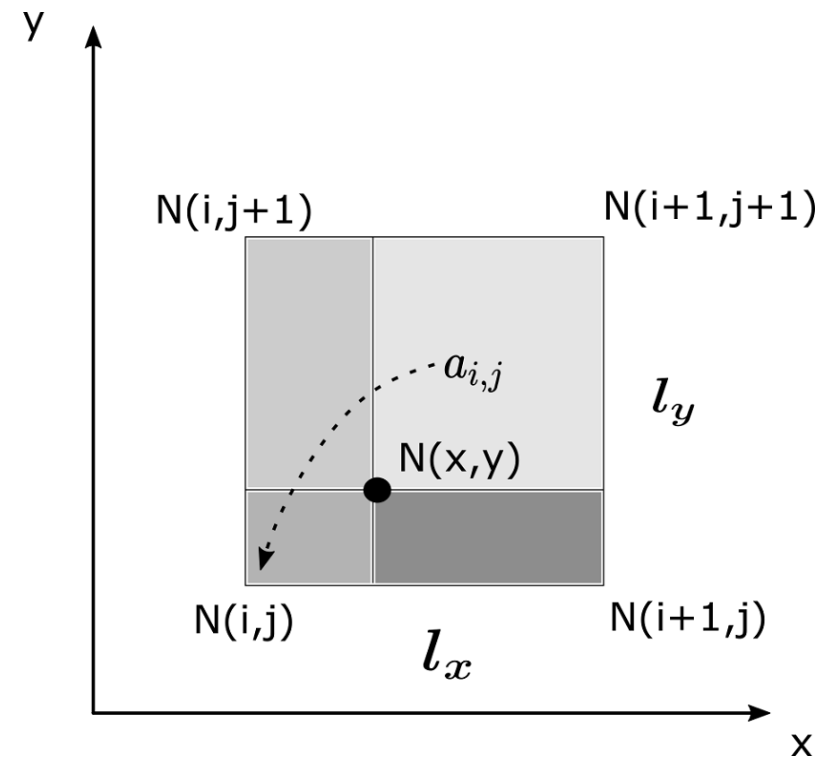

(a) 2-D Scheme

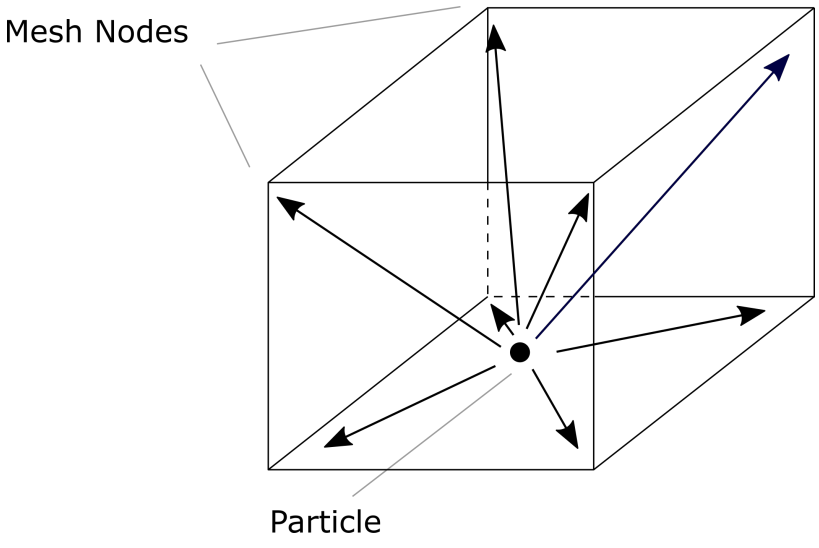

(b) 3-D Scheme

Figure 3.9. The scatter process in a PIC loop

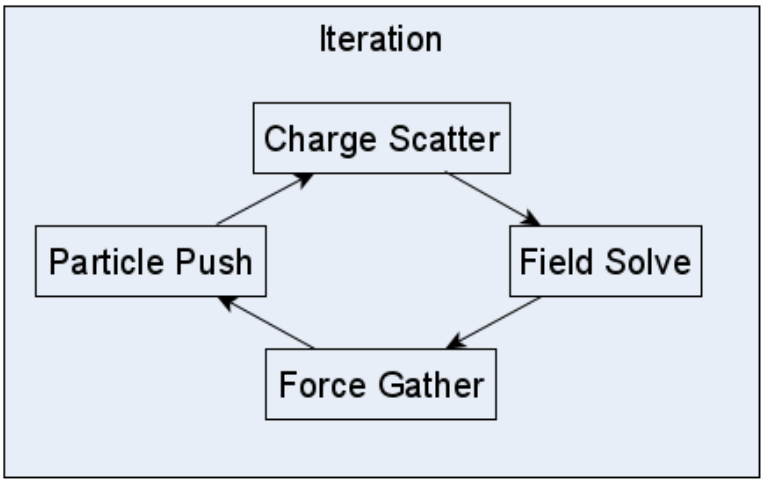

Figure 3.10. A complete PIC loop

3.2.3. Force Gather. The motion of the charged particles inside the computation domain depends on the forces acting on the particles, including gravity and electrostatic force. While the gravity acting on each particle is constant through the simulation, the electrostatic force is determined by the net charge on the particle and the surrounding electric field. Therefore, after obtaining the field information in the computation domain, the electric field quantity on mesh nodes will be gathered to the charged particles located inside the mesh to calculate the specific electrostatic force.

3.2.4. Particle Push. The acceleration in each direction of the particle will then be calculated through the electrostatic force, and the distance in each direction that the particle will move in an iteration can be determined with the time step dt.

3.2.5. PIC Loop. In each iteration of the numerical simulation, a complete PIC loop will run to obtain the field quantities self-consistently. A complete PIC loop is consist of the steps introduced above, which is Charge Scatter, Field Solve, Force Gather, and Particle Push. The procedure of a complete PIC loop are presented in Figure 3.10.

3.3. THE FD-PIC METHOD

The fully kinetic simulation code used in this dissertation combines the FD and PIC methods. The FD method is applied in the solver code, used to solve the Poisson's equation in each iteration. The PIC method is applied to resolve the transport dynamics of the particles.

3.3.1. FD Solver. To obtain the electric potential and electric field in the computation domain, the Preconditioned Conjugate Gradient (PCG) method was used in the solver code to solve the Poisson's equation on each mesh node in each time step in the simulations. A description of the procedure of the PCG solver is shown in Eq. (3.11), where r is the residual; C is the preconditioner matrix; and t is the preset tolerance. r will be compared with t in each loop iteration, and the loop will stop once it satisfies the convergence criterion ($r < t$).

3.3.2. The FD-PIC Flowchart. The whole procedure of the FD-PIC simulation are presented in the flowchart in Figure 3.11. At the beginning of the simulation, the electrostatic environment conditions will be set up, including the boundary conditions, convergence criterion, and physical parameters. Then the iteration of the PIC loop will start running until the result reaches the steady state or the total iteration number reaches the preset limit iteration number. The data of the quantities of interest will be generated every certain iterations.

Choose the initial value of x_0

$$r_0 = b - Ax_0$$

$$z_0 = C^{-1} r_0$$

$$d_0 = z_0$$

Start the PCG loop

$$a_k = \frac{r_k^T z_k}{d_k^T A d_k}$$

$$x_{k+1} = x_k + a_k d_k$$

$$r_{k+1} = r_k - a_k A d_k$$

$$z_{k+1} = C^{-1} r_{k+1}$$

$$\beta_{k+1} = \frac{r_{k+1}^T z_{k+1}}{r_k^T z_k}$$

$$d_{k+1} = z_{k+1} + \beta_{k+1} d_k$$

where $k = 0, 1, 2, ...$

Stop loop when $r < t$ (3.11)

3.4. SUMMARY

In this section, we introduced the FD-PIC code we used for the simulations. We presented the FD method which applied in the solver code to solve the PDE problem in each iteration in the simulations. Specifically, Poisson's equation is solved through FD method to obtain the electrostatic environment information in the computation domain in each iteration, then the electrostatic environment information is used to govern the motions of the charged particles, including solar wind electrons, solar wind ions, photoelectrons, and charged dust grains. The PCG method is applied in our code to solve the governing equations.

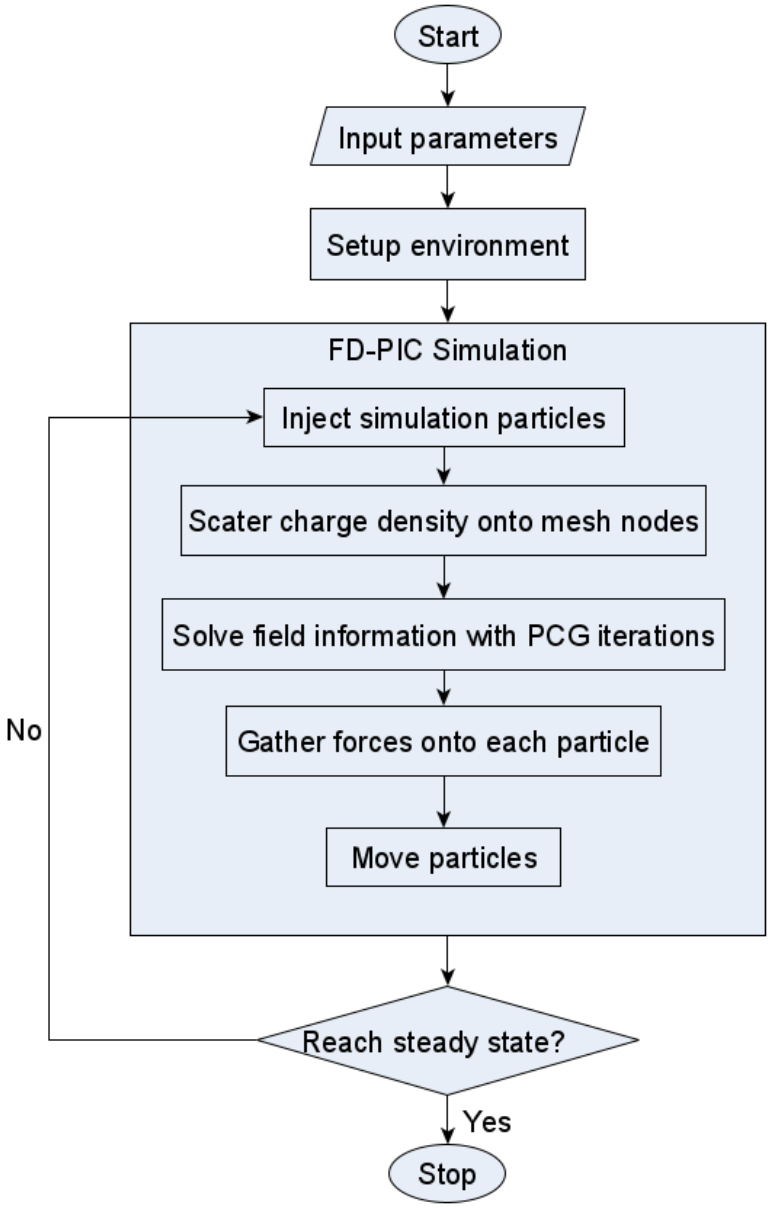

Figure 3.11. The FD-PIC simulation flowchart

We also presented the PIC method which is used to simulate the particle motions through steps including Charge Scatter, Field Solve, Force Gather, and Particle Push. With the combination of the FD and PIC methods, our code is able to resolve the electrostatic environment near the lunar surface self-consistently.

4. CODE VALIDATION

In this section, we will introduce the details of the setup of the simulations, and the derivation of the 1-D semi-analytic model of the photoelectron sheath. We will also validate the code by comparing the simulation results with the 1-D semi-analytic solutions. In Section 4.1, we will introduce the particle loading and injection. In Section 4.2, we will test the field solver in the code. In Section 4.3, we will show the details of the derivation of the 1-D semi-analytic model. And in Section 4.4, we will present the validation of the FD-PIC code and show the influence of the drifting electrons. A brief summary of this section will be given in Section 4.5.

4.1. PARTICLE LOADING AND INJECTION

In this section, we will introduce the particle loading and injection in our simulations. Specifically, we will present the velocity distribution of electrons, the velocity sampling methods, and the verification of the particle loading and injection.

4.1.1. Velocity Distribution. For pre-loaded solar wind electrons in the computation domain, we considered both *Maxwellian* and *Kappa* velocity distribution and compared the difference between these two distributions. If the computation domain contains the surface with "inject" boundary conditions, meaning that a certain number of particles will be injected into the computation domain in each iteration, we will also need to sample the injected particles. In the simulations we used the Acceptance-Rejection approach to generate different distributions. The algorithm of the Acceptance-Rejection approach is shown in Eq. (4.1), where W is the width of the interval of the generated velocity; $f(v)$ is the probability function of the velocity; R_i is a uniform set of random numbers between 0 and 1; v_{th} is the thermal velocity; and v_{d} is the drifting velocity.

$$
\begin{aligned}
& r = 2W \cdot R_1 - W \\
& \text{IF} \quad r - \frac{v_{\mathrm{d}}}{v_{\mathrm{th}}} <= 0 \\
& \qquad \text{GO TO THE BEGINNING} \\
& \text{ELSE} \\
& \qquad sol = \frac{(r - \frac{v_{\mathrm{d}}}{v_{\mathrm{th}}}) f(r - \frac{v_{\mathrm{d}}}{v_{\mathrm{th}}})}{g} \\
& \qquad \text{IF} \quad sol <= R_2 \\
& \qquad\qquad \text{GO TO THE BEGINNING} \\
& \qquad \text{ELSE} \\
& \qquad\qquad v_a = r \cdot v_{\mathrm{th}} \\
& \text{END}
\end{aligned}
\tag{4.1}
$$

4.1.1.1. *Maxwellian* distribution. There are two species of electrons considered in the 1-D semi-analytic model: the solar wind electrons from the ambient plasma and the photoelectrons emitting from the lunar surface. In the *Maxwellian* distribution cases, we assume that both of the two electron populations follow the *Maxwellian* distribution. Particularly, the photoelectrons emitting from the lunar surface are approximated as *Maxwellian* due to the following reasons: 1) The energy distribution of photoelectrons can be complicated because it is related to a number of parameters including work function, quantum yield, photon energy, and the corresponding photon numbers. The quantum yield, which decides the energy distribution, has a large range of uncertainty (Popel *et al.* (2014)). 2) According to Popel *et al.* (2013), when neglecting the effects of the photoelectrons generated from the lofted lunar dust grains, the velocity distribution of photoelectrons at the lunar surface can be approximated by the *Maxwellian* distribution. Therefore, in this dissertation, we have limited the photoelectron species to those originated from the lunar surface in order to derive the 1-D semi-analytic model.

It is noted here that although photoelectrons originated from surfaces of dust grains exist in the sheath as well (Popel *et al.* (2013)), it is not easy to determine the magnitude of such influence due to the large uncertainty of concentration of dust grains above the lunar surface and the number of generated photoelectrons (Popel *et al.* (2014)). In addition, it was found that the concentration of lofted dust grains is considerable only in the region of about 2 m above the lunar surface, which is much smaller than the scale of the photoelectron sheath considered here (tens of meters). Therefore, the influence of photoelectrons originated from dust grains is neglected in the sheath model.

The unperturbed solar wind electrons follow the 1-D drifting *Maxwellian* velocity distribution as in Eq. (4.2), whereas the unperturbed photoelectrons originating from the lunar surface follow the 1-D stationary *Maxwellian* velocity distribution as in Eq. (4.3):

$$f_{\mathrm{swe}}(v) = \frac{1}{\sqrt{\pi} v_{\mathrm{th}}} \exp\left[- \frac{(v - v_{\mathrm{d}})^2}{{v_{\mathrm{th}}}^2} \right] \tag{4.2}$$

$$f_{\mathrm{phe}}(v) = \frac{1}{\sqrt{\pi} v_{\mathrm{th}}} \exp\left(- \frac{v^2}{{v_{\mathrm{th}}}^2} \right) \tag{4.3}$$

where $v_{\mathrm{th}} = \sqrt{2kT/m}$ is the thermal velocity (k is the Boltzmann constant) and v_{d} is the drifting velocity.

In order to obtain the velocity distribution as a function of the distance from the lunar surface, we apply the conservation of energy along z-direction as in Eq. (4.4):

$$\frac{1}{2} m v_z^2(z) - e\phi(z) = \left[\frac{1}{2} m v_z^2 - e\phi \right]_j \tag{4.4}$$

where $\phi(z)$ is the electric potential at position z, and the right-hand side should be evaluated at the location of electron origin (denoted by j), i.e., $j = \infty$ for ambient solar wind electrons and $j = 0$ for photoelectrons. Solving for v_z at electron origin from Eq. (4.4), one can get:

$$v_z^2\big|_j = v_z^2(z) - \frac{2e}{m} \left[\phi(z) - \phi\big|_j \right] \tag{4.5}$$

where the vertical bar denotes "evaluated at" as in Eq. (4.4). Therefore, the distribution functions in Eq. (4.2) and Eq. (4.3) at any position along z will be rewritten as Eq. (4.6) and Eq. (4.7), respectively.

$$f_{\mathrm{swe}}(z,v) = \frac{1}{\sqrt{\pi}v_{\mathrm{th}}} \exp\left[-\frac{(v-v_{\mathrm{d}})^2}{{v_{\mathrm{th}}}^2} \right] \exp\left[\frac{e(\phi(z)-\phi_\infty)}{kT} \right] \tag{4.6}$$

$$f_{\mathrm{phe}}(z,v) = \frac{1}{\sqrt{\pi}v_{\mathrm{th}}} \exp\left(-\frac{v^2}{{v_{\mathrm{th}}}^2} \right) \exp\left[\frac{e(\phi(z)-\phi_0)}{kT} \right] \tag{4.7}$$

4.1.1.2. κ-distribution. According to the measurements data of the solar wind, the velocity of the solar wind electrons can be better described by κ-distribution than *Maxwellian* (Christon *et al.* (1989, 1988); Halekas *et al.* (2005b); Slavin *et al.* (1985); Vasyliunas (1971)). Thus in this assumption, we consider that the solar wind electrons are following κ-distribution. Except the velocity distribution, the other parameters are all kept the same as those in the last assumption.

The analytic expression of the 1-D stationary κ-distribution is shown in Eq. (4.8), and in Eq. (4.9) when considering the drifting velocity.

$$f_\kappa(v) = \frac{1}{\sqrt{\pi}\theta\kappa^{\frac{3}{2}}} \frac{\Gamma(\kappa+1)}{\Gamma(\kappa-\frac{1}{2})} \left(1+\frac{v^2}{\kappa\theta^2}\right)^{-\kappa} \tag{4.8}$$

$$f_\kappa(v) = \frac{1}{\sqrt{\pi}\theta\kappa^{\frac{3}{2}}} \frac{\Gamma(\kappa+1)}{\Gamma(\kappa-\frac{1}{2})} \left[1+\frac{(v-v_{\mathrm{d}})^2}{\kappa\theta^2}\right]^{-\kappa} \tag{4.9}$$

where κ is the spectral index, v_{d} is the drifting velocity, v_{th} is the thermal velocity, and θ is expressed as in Eq. (4.10) (Summers and Thorne (1991)).

$$\theta = \sqrt{\frac{(2\kappa-3){v_{\mathrm{th}}}^2}{2\kappa}} \tag{4.10}$$

In most situations (including the average solar wind conditions that we focused on in this dissertation), the *Maxwellian* distribution can describe the physical velocity distribution of electrons (both solar wind electrons and photoelectrons) quiet well, therefore in order to compare the simulation results with analytic solutions, we only derive the semi-analytic solutions following the *Maxwellian* distribution in this dissertation.

4.1.2. Velocity Sampling for Loaded Particles. In FD-PIC simulations, a certain amount of particles representing solar wind protons and electrons will be pre-loaded into the computation domain. These particles are called "loaded particles". In this dissertation, we considered two velocity distributions, *Maxwellian* and κ-distribution, for the pre-loaded particles.

4.1.2.1. Loaded *Maxwellian*. The approach to generate sample velocities that following *Maxwellian* distribution for loaded particles can be found in Birdsall and Langdon (2018). It involves a work directly with a set of uniform random numbers between 0 and 1. The equation that used to generate a random *Maxwellian* distribution is shown below:

$$v_M = v_t\left(\sum_{i=1}^{N} \cdot R_i - \frac{N}{2}\right) \cdot \left(\frac{N}{12}\right)^{-0.5} \tag{4.11}$$

where v_{th} is the thermal velocity; R_i is a uniform set of random numbers between 0 and 1; $N = 12$; v_M is the generated velocity that follow *Maxwellian* distribution; and v_{d} is the drifting velocity.

4.1.2.2. Loaded κ-distribution. The approach to sample the velocities of loaded particles for κ-distribution is as follows (Abdul and Mace (2014)), where R_1 and R_2 are random numbers uniformly taken between 0 and 1; κ is the κ-distribution coefficient; v_{th} is the thermal velocity; and v_{d} is the drifting velocity.

$$\theta = \sqrt{\frac{(2\kappa - 3)v_{\text{th}}^2}{2\kappa}}$$
$$a_1 = \sqrt{(2\kappa - 1)\left(R_1^{\frac{-2}{(2\kappa-1)}} - 1\right)}\cos(2\pi R_2)$$
$$a_2 = \sqrt{\frac{\kappa\theta^2}{(2\kappa - 1)}}$$
$$v_\kappa = v_{\text{d}} + a_1 \cdot a_2 \tag{4.12}$$

To validate the accuracy of (4.12), we compared the probability distribution of the generated velocities with the analytic expression. Figure 4.1 shows an example of the comparisons of the loaded particle velocities (κ-distribution). In this case, both electrons (stationary) and ions (drifting, $v_{\text{d}}/v_{\text{th}} = -3.0$) are considered thermal (to compare with the analytic distribution function). In addition to the approach introduced in Abdul and Mace (2014), we also used the Accept-Reject approach to sample the velocities for loaded particles and compared with the analytic expression on the same plot. Both comparisons show good agreement.

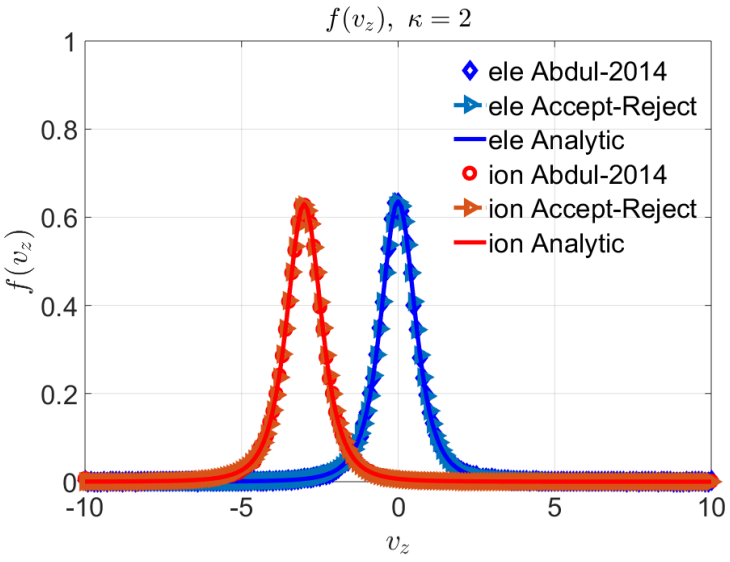

Figure 4.1. The comparison between the generated velocities and the calculated velocities

4.1.3. Velocity Sampling for Injected Particles. Within each PIC step, the particles representing ambient solar wind protons and electrons, and photoelectrons are injected into the computation domain from the corresponding domain boundaries. When the drifting velocity is taken into account, we will need to consider the one-sided velocity at these boundaries.

Figure 4.2 shows the theoretical profiles of the probability distribution of the one-sided velocity for a case of $v_d < 0$, where Figure 4.2(a) shows the overall probability distribution; Figure 4.2(b) shows the probability distribution of the velocity along z; and Figure 4.2(c) shows the probability distribution of the velocity along -z. As it shows, the distribution profiles of the velocity have different shapes for positive and negative velocities. This difference will affect the value of the one-sided velocity, $< v >_+$ and $< v >_-$, which are calculated below. This one-sided velocity will be used to calculate the total number of the injected particles in PIC simulations.

Again, we used the Acceptance-Rejection approach to sample the one-sided velocities for injected particles in the code.

4.1.3.1. Injected *Maxwellian*. To create *Maxwellian* distribution for injected particles, we need to consider whether the particles are stationary or drifting. For stationary particles, the one-sided velocity can be obtained by Eq. (4.13).

$$< v >_+ = < v >_- = \frac{v_{th}}{2\sqrt{\pi}} \tag{4.13}$$

where v_{th} is the thermal velocity.

For drifting particles, the one-sided velocity can be obtained by Eqs. (4.14) and (4.15).

$$< v >_+ = \frac{1}{2}\left\{\frac{v_{th}}{\sqrt{\pi}} \exp\left(- \frac{v_d^2}{v_{th}^2} + v_d\left[1 + \mathrm{erf}\left(\frac{v_d}{v_{th}}\right)\right]\right\}\right. \tag{4.14}$$

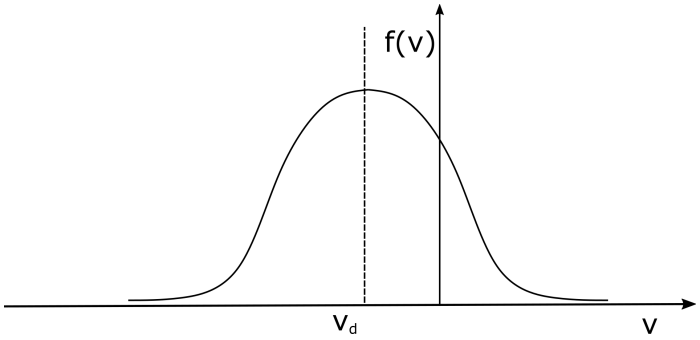

(a) Drifting velocity profile

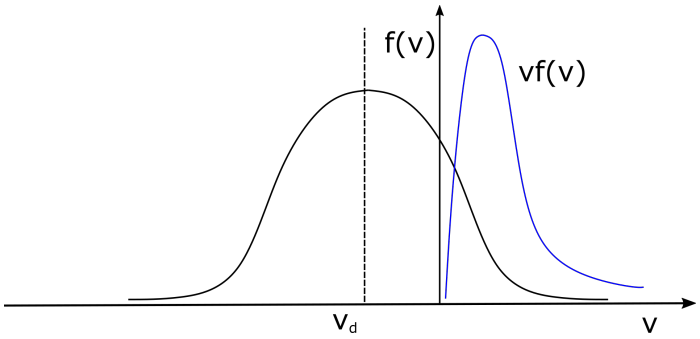

(b) Velocity profile along z

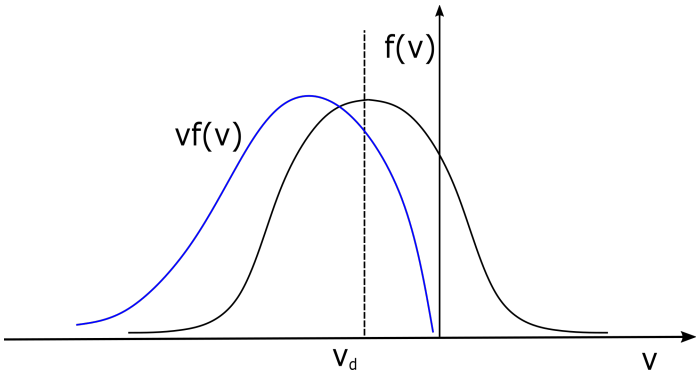

(c) Velocity profile along -z

Figure 4.2. The sketch of the probability distributions of the one-sided velocity

$$< v >_{-} = -\frac{1}{2}\left\{\frac{v_{\rm th}}{\sqrt{\pi}}\exp\left(-\frac{v_{\rm d}^2}{v_{\rm th}^2}\right) + v_{\rm d}\left[{\rm erfc}\left(\frac{v_{\rm d}}{v_{\rm th}}\right)\right]\right\} \tag{4.15}$$

where $v_{\rm d}$ is the drifting velocity.

4.1.3.2. Injected κ-distribution. The equation to obtain the one-sided velocities for stationary particles that following κ-distribution is shown in Eq. (4.16).

$$< v >_+ = < v >_- = c_1\Big[- c_2 \frac{1}{(1-\kappa)}\Big] \tag{4.16}$$

$$\begin{aligned} c_1 &= \frac{1}{\sqrt{\pi}\kappa^{\frac{3}{2}}\theta}\frac{\Gamma(\kappa+1)}{\Gamma(\kappa-\frac{1}{2})} \\ c_2 &= \frac{\kappa\theta^2}{2(1-\kappa)}(1+\frac{{v_\mathrm{d}}^2}{\kappa\theta^2})^{1-\kappa} \end{aligned} \tag{4.17}$$

where κ is the κ-distribution coefficient.

For the drifting particles, the equations to obtain the one-sided velocities are shown in Eqs. (4.18) and (4.19).

$$\begin{aligned} < v >_+ &= \int_0^\infty v f_\kappa(v)\, dv \\ &= c_1\left\{(v-v_\mathrm{d})\ {}_2F_1\Big[\frac{1}{2},\kappa;\frac{3}{2};-\frac{(v-v_\mathrm{d})^2}{\kappa\theta^2}\Big]\right\}\Bigg|_0^\infty \end{aligned} \tag{4.18}$$

$$\begin{aligned} < v >_- &= \int_{-\infty}^0 v f_\kappa(v)\, dv \\ &= c_1\left\{(v-v_\mathrm{d})\ {}_2F_1\Big[\frac{1}{2},\kappa;\frac{3}{2};-\frac{(v-v_\mathrm{d})^2}{\kappa\theta^2}\Big]\right\}\Bigg|_{-\infty}^0 \end{aligned} \tag{4.19}$$

where ${}_2F_1[a,b;c;z]$ is the hypergeometric function.

Here we use an example to show the distribution profiles of the one-sided velocities. Figure 4.3 shows the one-sided velocities for stationary electrons and drifting ions along z and -z. For stationary electrons in this example, the velocity distribution is symmetric with respect to the $v_z = 0$, which results in $< v >_+ = < v >_-$. However, if the drifting velocity

is not zero, $< v >_+ \neq < v >_-$. Figure 4.4 shows all the one-sided velocities in one plot for comparison. Figure 4.5 and Figure 4.6 show the loaded and injected particle velocities following the *Maxwellian* and κ-distribution, respectively.

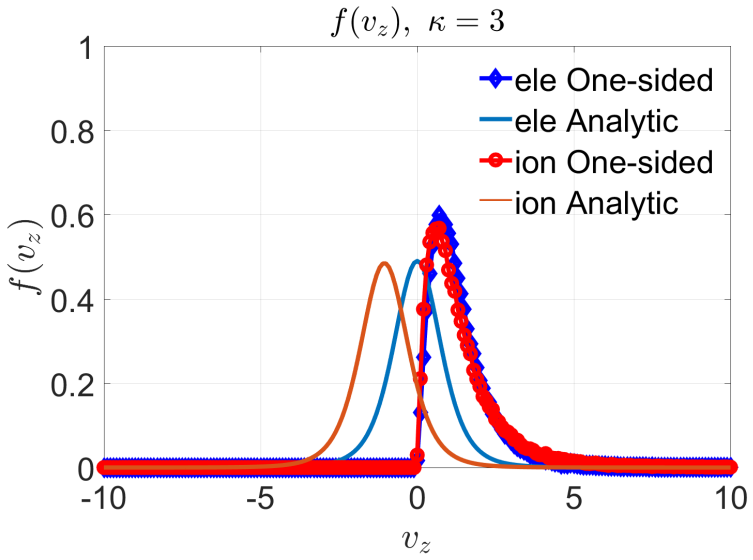

(a) Along z

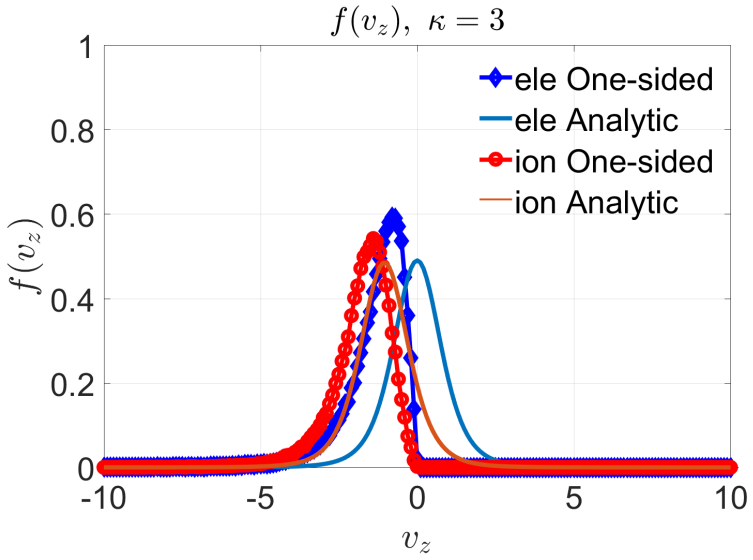

(b) Along -z

Figure 4.3. One-sided velocities for stationary electrons and drifting ions

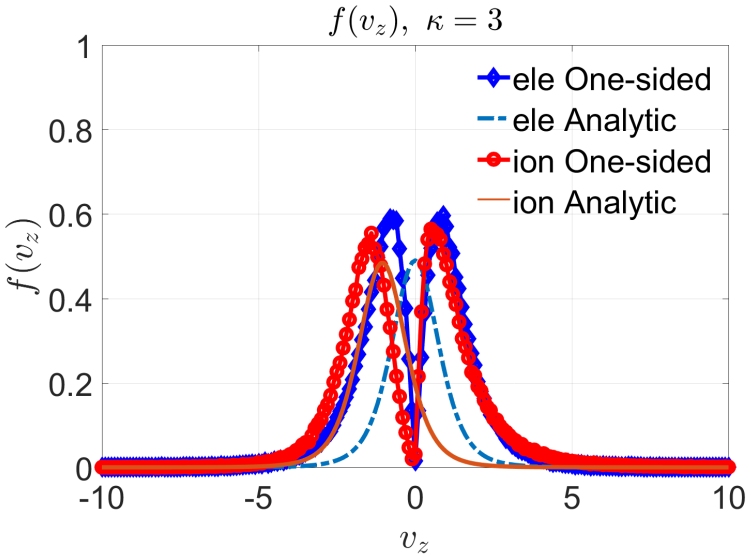

Figure 4.4. One-sided velocities for stationary electrons and drifting ions, plotted together

4.1.4. Verification of Particle Loading and Injection. In order to accurately sample the velocities for loaded and injected particles, we conducted a "test run" of particle loading/injection in the FD-PIC code without updating particles' velocities, thus all particles were moving through the simulation domain with their sampled velocities. In this "test run", the boundary condition of both the bottom and the top surfaces of the computation domain were set as "ambient inject", which means the particles were injected from both the bottom surface (velocity distribution follows Figure 4.6(a)), and the top surface (velocity distribution follows Figure 4.6(b)). The solar wind electrons were considered as stationary with $v_{\text{th}} = 1.0$, and the solar wind ions were considered as thermal and drifting with $v_{\text{th}} = 1.0$ and $v_{\text{d}}/v_{\text{th}} = -3.0$. In total 60,000 simulation particles (30,000 electrons and 30,000 ions) were pre-loaded into the computation domain as the initial condition, another 100 electrons and ions were injected into the $2 \times 2 \times 200$ computation domain in each time step (dt = 0.002, mesh size = 0.1). The simulation ran about 100 steps, the wall clock time was about 3 seconds. With a correct sampling method, the velocities of loaded and injected particles should follow the κ-distribution *at any time*.

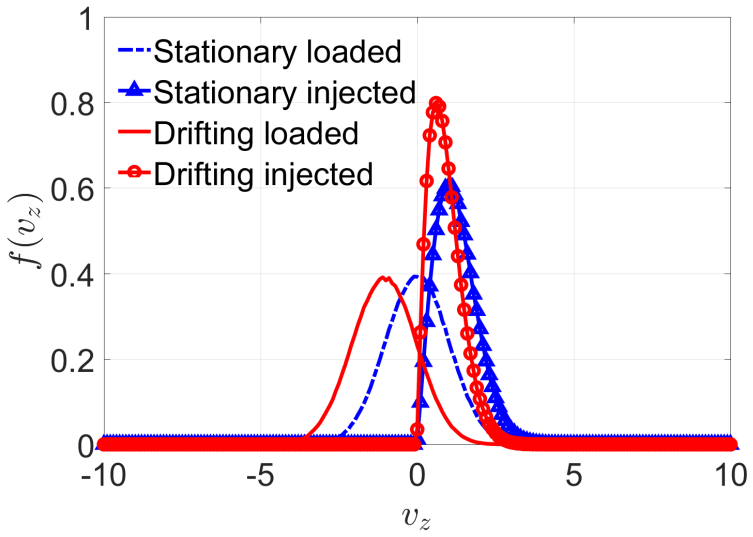

(a) Particle injected along z

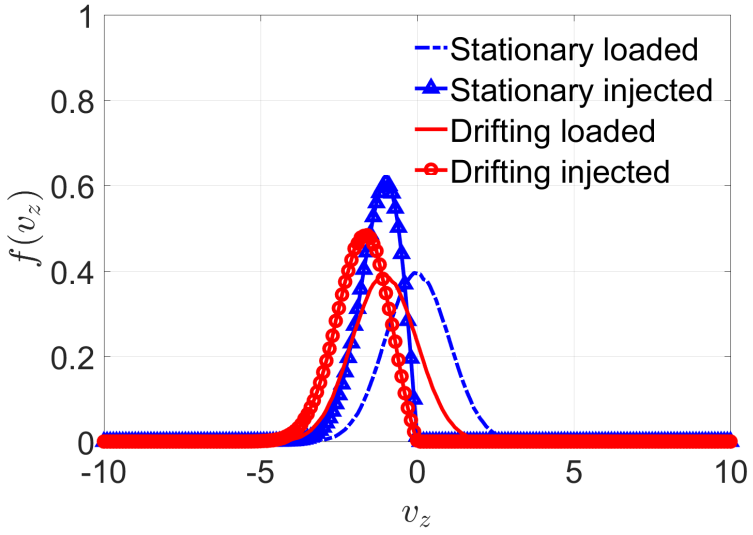

(b) Particle injected along -z

Figure 4.5. *Maxwellian*

Figure 4.7 shows the velocity distribution functions of both ions and electrons at two time steps ($\hat{t} = 0$ and $\hat{t} = 100$). The analytic solutions were also included for comparison on each of the plots. It can be seen from the comparison that, both the loaded and the injected particle velocities show good agreement with the analytic distribution at different time steps, which verifies the sampling method.

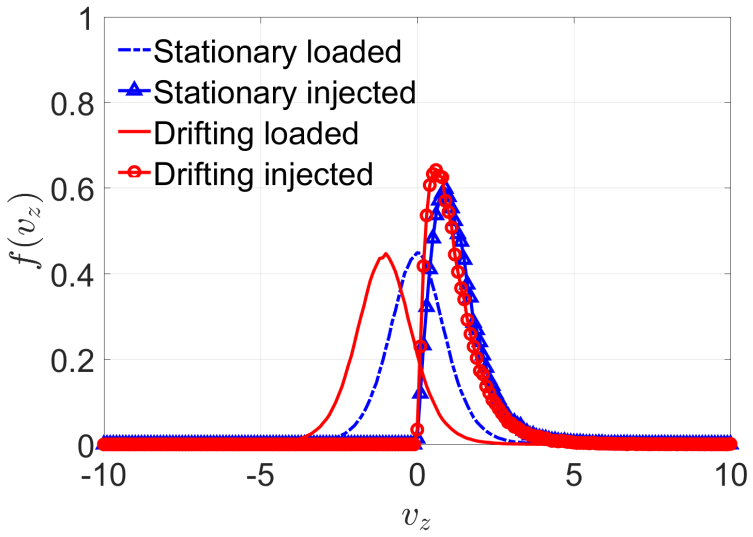

(a) Particle injected along z

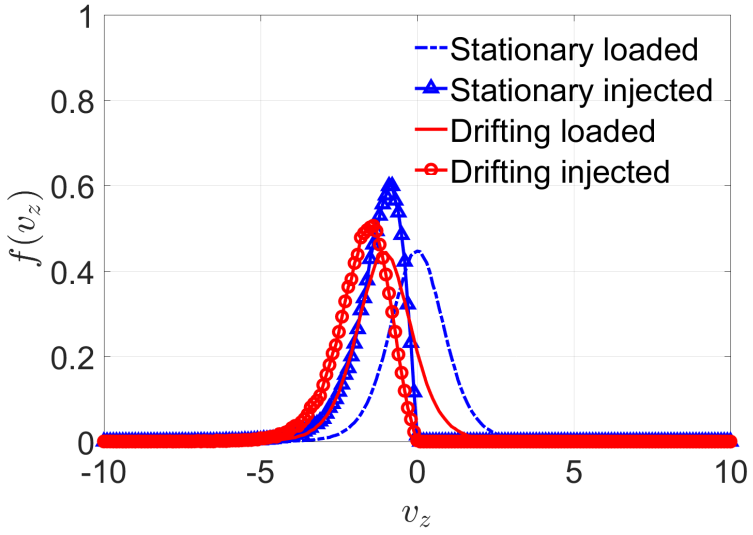

(b) Particle injected along -z

Figure 4.6. κ-distribution, κ = 4.5

It is noted here that in PIC simulations, we only set the top (Z_{max}) surface of the computation domain as "ambient inject" (the top surface is considered as the infinity area, and the bottom surface is considered as the lunar surface), hence the distribution function of the injected particle velocities will follow the profile as shown in Figure 4.5(b) for *Maxwellian*, and Figure 4.6(b) for κ-distribution.

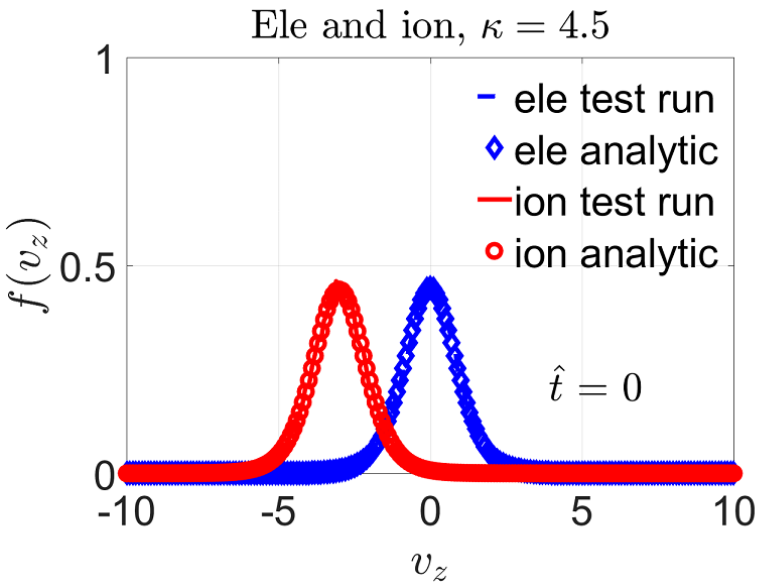

(a) Loaded electrons and ions at t = 0

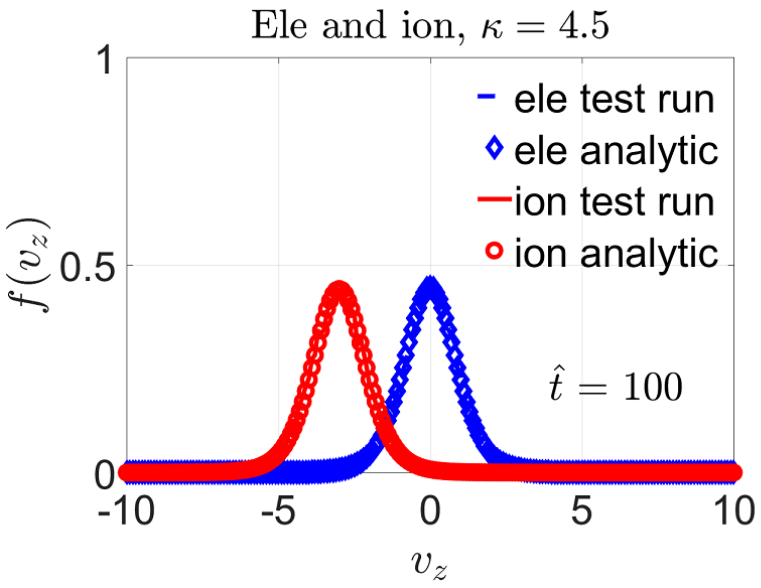

(b) Injected electrons and ions at t = 100

Figure 4.7. Distribution of loaded and injected electrons and ions

4.2. FIELD SOLVING

In this section, we will verify the accuracy of the solver code with some testing cases. All these testing cases are in 1-D condition, since the semi-analytic solutions can only be obtained for 1-D situations.

4.2.1. Potential Profile Without Plasma. We hardwired the object permitivity ε in this case, in order to obtain the potential profile in the computation domain without charged particles. In this situation, the analytic solutions used for comparisons can be calculated, and the shape of the potential profile should be a straight line due to the completely neutral electric field.

4.2.1.1. Without object. We did not consider the influence of the object to the potential profiles in this case, so there were no object in the computation domain. The size of the computation domain is 2×2×200 PIC cells, we collected the data on the central line along z in order to simulate the 1-D situation. The bottom surface of the computation domain is considered as the lunar surface, whereas the top surface is considered as infinity. The computation domain is shown in Figure 4.8.

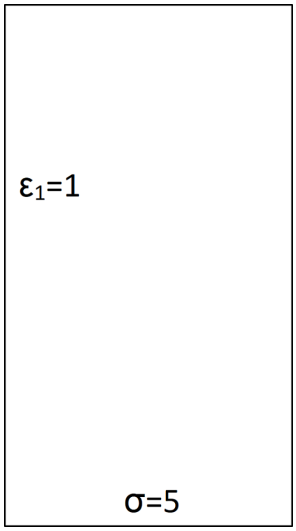

Figure 4.8. Computation domain

The boundary condition at the top surface is $\phi = 0$, and the boundary condition at the bottom surface is $\frac{\partial \phi}{\partial z} = 0$. To obtain the analytic solution, it is needed to specify the surface charge density on the lunar surface. We set the surface density to be 5.0 and 10.0

in the testing cases. Then the analytic solution of the potential profile can be obtained with Eq. (4.20). According to the assumed boundary conditions, Eq. (4.20) can be written as Eq. (4.21).

$$\phi(z) = a \cdot z + b \tag{4.20}$$

$$\begin{aligned} a \times 20.0 + b &= 0 \\ -(-a \cdot \varepsilon) &= -5 \end{aligned} \tag{4.21}$$

Then the analytic expression of the potential profile in this case was obtained as Eq. (4.22).

$$\phi(z) = -5 \cdot z + 100 \tag{4.22}$$

Figure 4.9 shows the comparison between the analytic solution and the simulation, It can be seen that the results agree well with each other, validating the accuracy of the code.

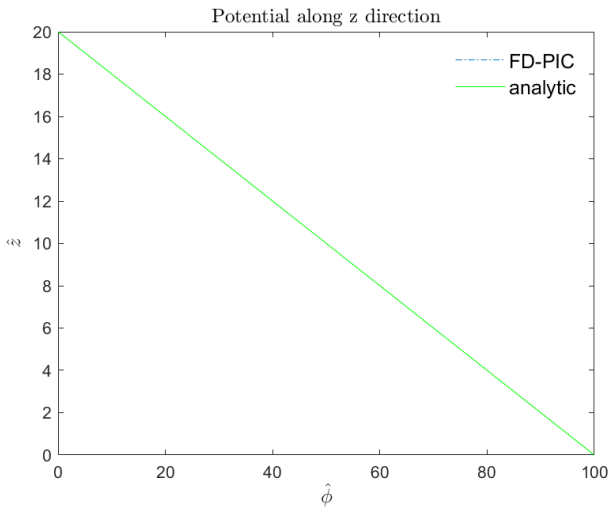

Figure 4.9. Comparison between analytic and numerical solutions with $\sigma = 5$

In another case, the surface density was set as 10.0, the analytic expression is shown in Eq. (4.23). The comparison of the potential between the analytic solution and the simulation is shown in Figure 4.10. Again, the agreement is well, indicating the code is accurate.

$$\phi(z) = -10 \cdot z + 200 \tag{4.23}$$

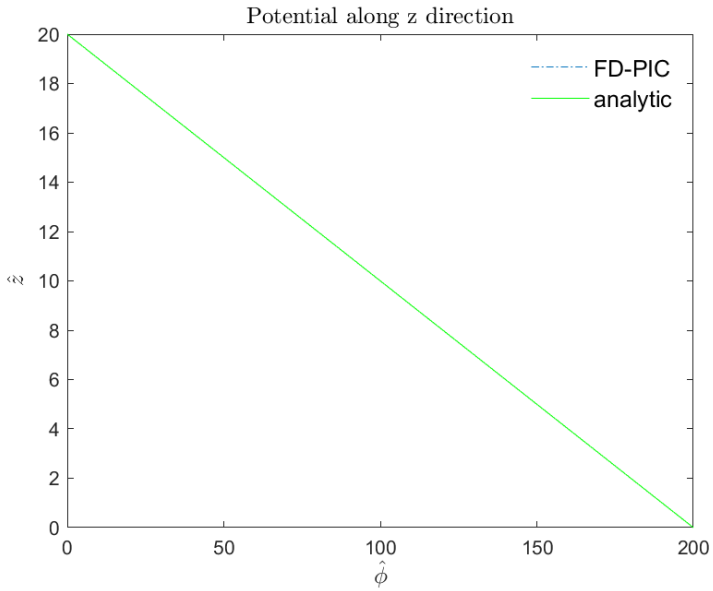

Figure 4.10. Comparison between analytic and numerical solutions with $\sigma = 10$

In order to validate the code for 3-D simulations, we need to test the results in all directions. The computation domains of these testing cases are shown in Figures 4.11, 4.12, and 4.13. The comparisons of potential between simulations and analytic solutions in these testing cases are shown in Figures 4.14, 4.15, and 4.16. It can be seen that the agreements between the analytic solutions and the simulations are very well for all testing cases.

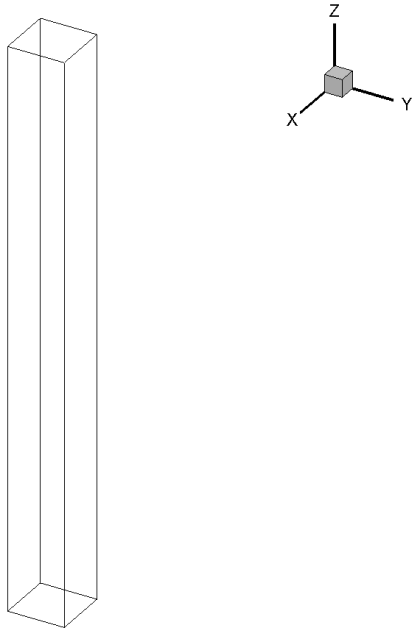

Figure 4.11. Computation domain in z direction

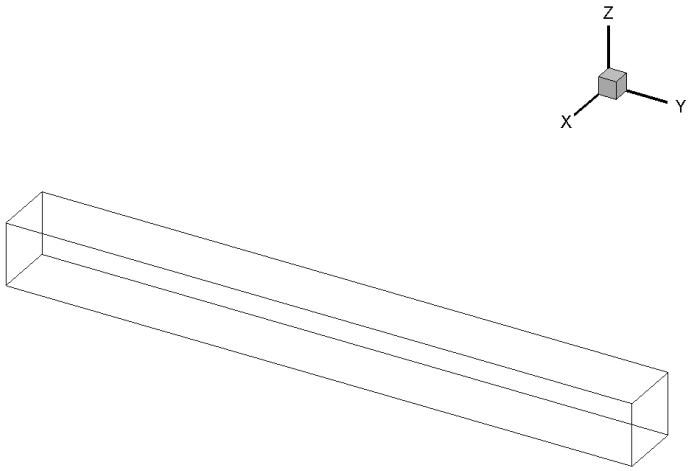

Figure 4.12. Computation domain in y direction

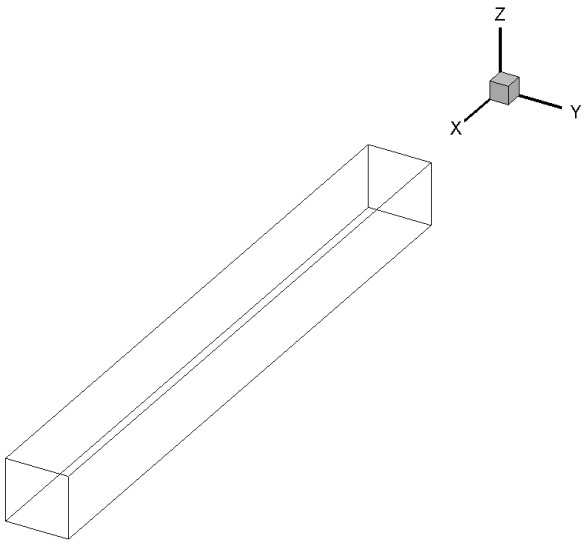

Figure 4.13. Computation domain in x direction

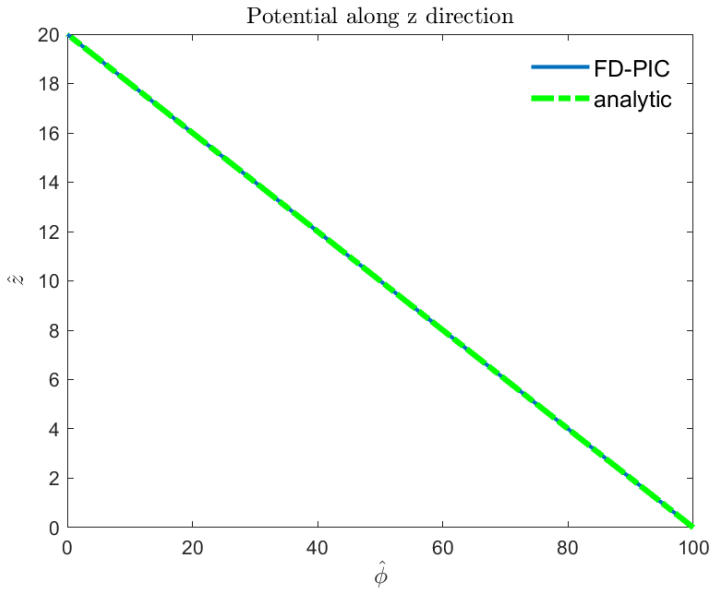

Figure 4.14. Potential along z without object

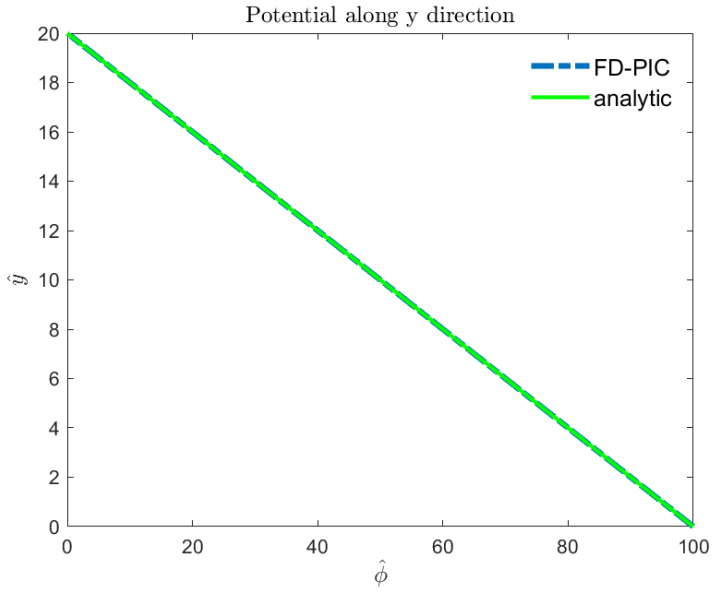

Figure 4.15. Potential along y without object

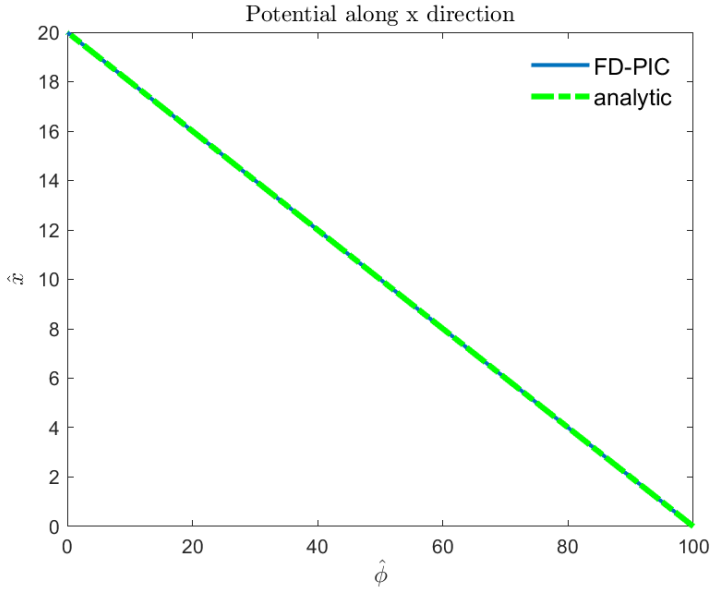

Figure 4.16. Potential along x without object

4.2.1.2. With object. In the next test, we considered an object located inside the computation domain. The existence of the object with a different permitivity influences the electrostatic environment inside the computation.

In this case, the position of the object surface is $z = 2.0$, the computation domain is 2×2×200 PIC cells, the boundary condition at the top surface is $\phi = 0$, and the boundary condition at the bottom surface is $\frac{\partial \phi}{\partial z} = 0$. The object permitivity is $\varepsilon_2 = 4.0$, the surface density on the object surface is kept as $\sigma = 5.0$. The computation domain is shown in Figure 4.17.

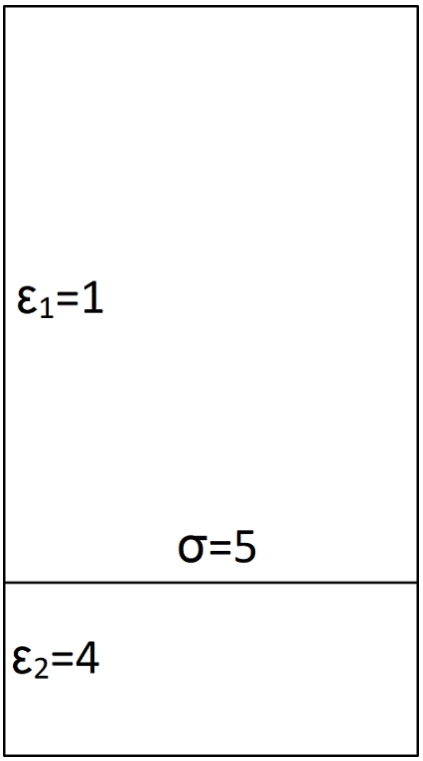

Figure 4.17. The computation domain with object surface

The analytic expression of the potential profile is listed below:

$$\phi(z) = a \cdot z + b \tag{4.24}$$

Since there are two subareas in this computation domain, we need two equations to solve the two unknowns of the entire potential profile. The two equations used in this case are listed in Eq. (4.25).

$$\begin{aligned} \phi_1(z) &= a_1 \cdot z + b_1 \\ \phi_2(z) &= a_2 \cdot z + b_2 \end{aligned} \tag{4.25}$$

The analytic expression of the potential profile will then be obtained as Eq. (4.26) with the assumed boundary conditions.

$$\begin{aligned} a_1 \times 20.0 + b_1 &= 0 \\ a_1 \times 2.0 + b_1 &= a_2 \times 2.0 + b_2 \\ a_2 \times 2.0 + b_2 &= a_2 \times 0.0 + b_2 \\ -(-a_1 \cdot \varepsilon_1 - a_2 \cdot \varepsilon_2) &= -5 \end{aligned} \tag{4.26}$$

The solution of Eq. (4.26) is:

$$\begin{aligned} a_1 &= -5 \\ b_1 &= 100 \\ a_2 &= 0 \\ b_2 &= 90 \end{aligned} \tag{4.27}$$

Then we can obtain the analytic solutions as shown in Eq. (4.28).

$$\begin{aligned} \phi_1(z) &= -5 \cdot z + 100 \ (20.0 \geq z \geq 2.0) \\ \phi_2(z) &= 90 \ (2.0 \geq z \geq 0.0) \end{aligned} \tag{4.28}$$

Figure 4.18 shows the good agreement of the potential obtained with analytic calculations and simulations, validating the accuracy of the code.

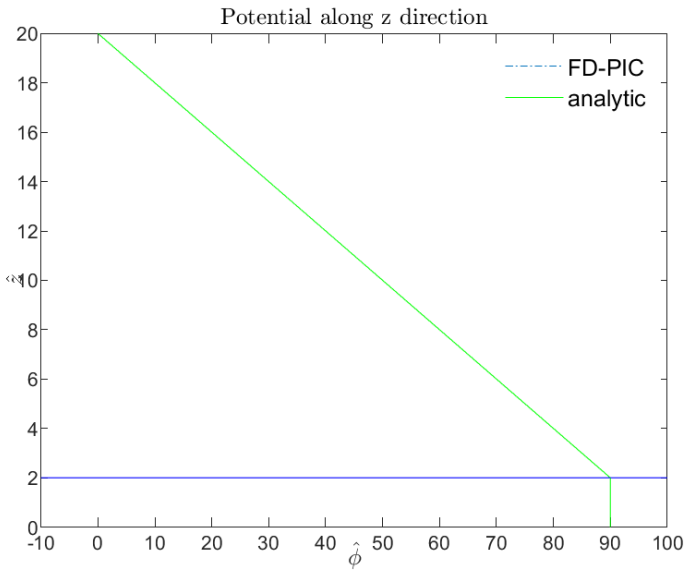

Figure 4.18. Comparison between analytic and numerical solutions with object surface when $\sigma = 5$

Again, to validate the accuracy of the code in 3-D simulations, we need to test the code in all directions. The computation domains for all directions are shown in Figures 4.19, 4.20, and 4.21. Comparisons of potential profiles between analytic solutions and simulations for all testing cases are shown in Figures 4.22, 4.23, and 4.24. Again, the agreements are very well.

4.2.2. Potential Profile With Plasma. After validating the code for the situations without plasma, here we will need to continue testing the accuracy of the code for situations with plasma. In this section, we will also consider two scenarios, one with no object inside the computation domain, the other one with an object located on the surface.

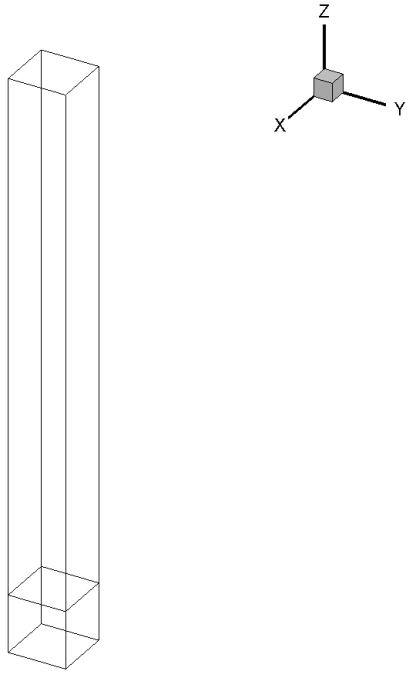

Figure 4.19. Computation domain in z direction with object

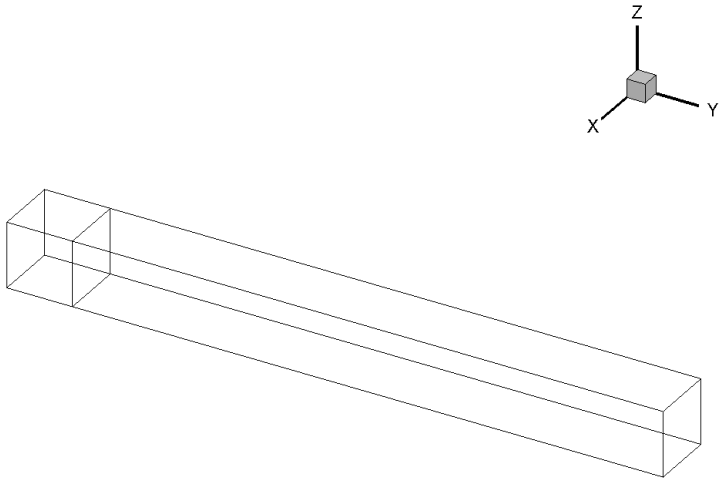

Figure 4.20. Computation domain in y direction with object

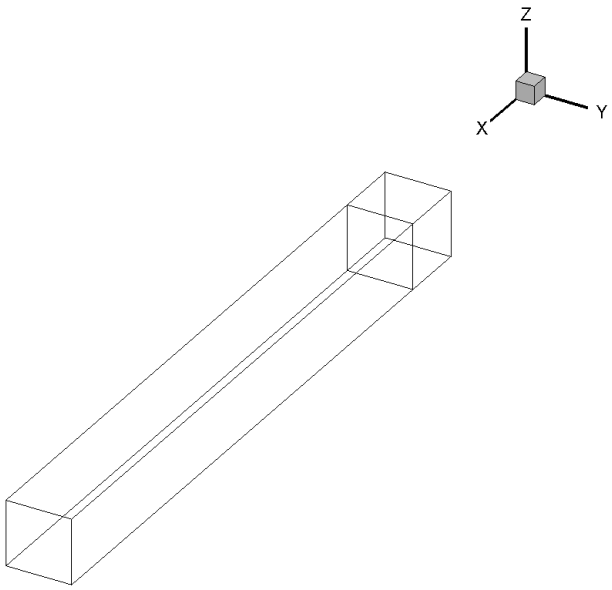

Figure 4.21. Computation domain in x direction with object

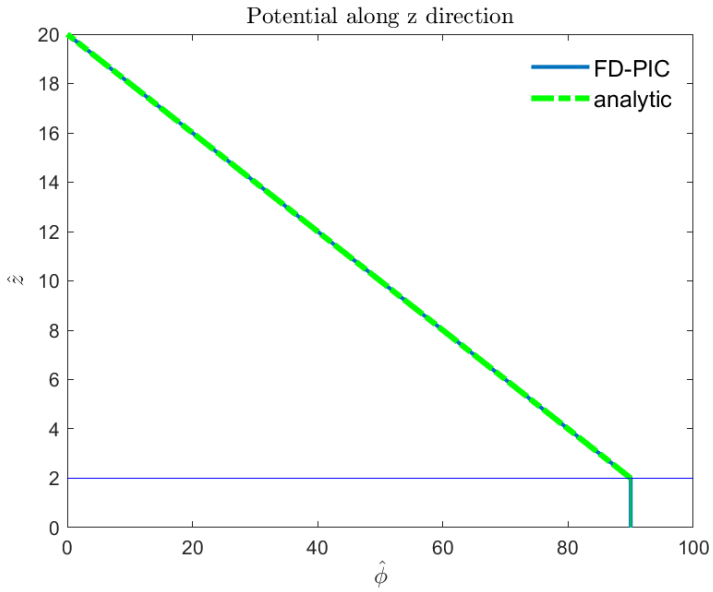

Figure 4.22. Potential along z with object

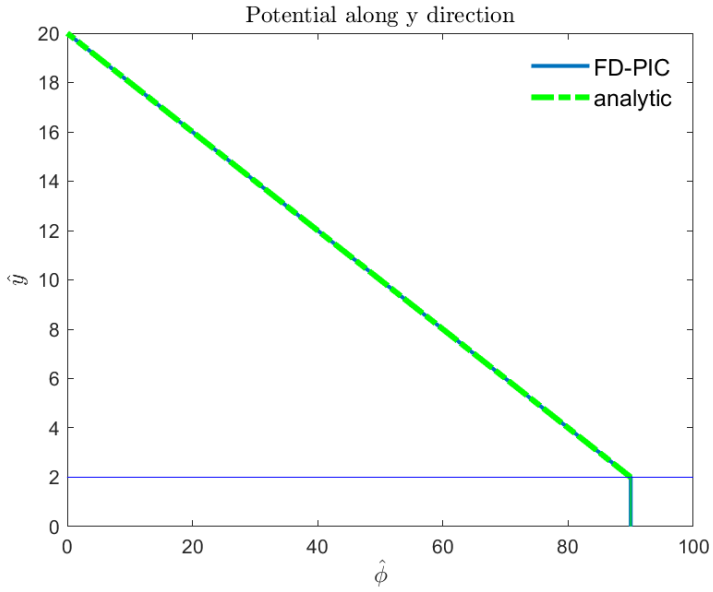

Figure 4.23. Potential along y with object

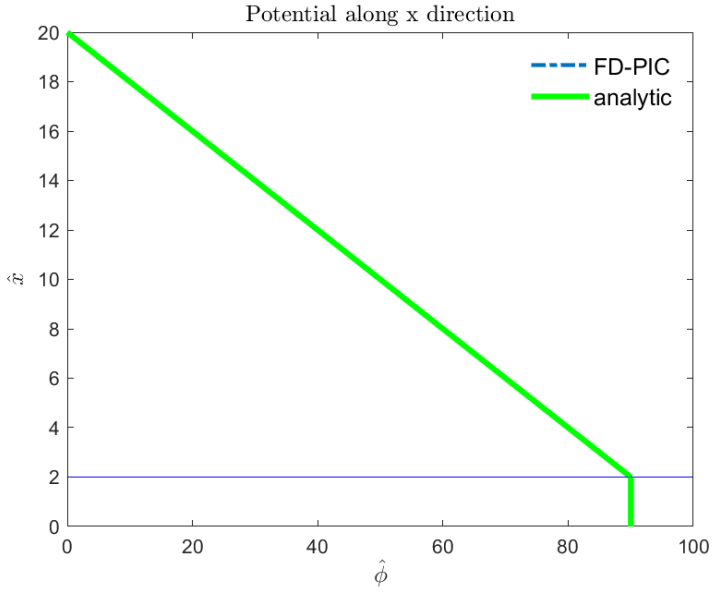

Figure 4.24. Potential along x with object

4.2.2.1. Without object. In this case, the dimension of the computation domain is 2×2×200 PIC cells, the surrounding boundaries are all "periodic" boundaries, which means once the particles travel across the boundary, it will enter the computation domain from the opposite boundary, so the computation domain can be used to represent a larger area. The solar wind electrons and ions are injected from the top surface, since in reality the thermal velocity of the solar wind electrons is much larger than the solar wind ions, in this simulation, the solar wind ions can be considered "cold" (no thermal velocity) and the drafting velocity is dominant on the dynamics of ions. In the simulation, in total 200,000 simulation particles (100,000 solar wind electrons and 100,000 solar wind ions) were pre-loaded into the computation domain as the initial condition, another 100 solar wind electrons and 100 solar wind ions were injected into the computation domain in each time step (dt = 0.01). The simulation ran about 50,000 steps, which was about 250 seconds in physical units. The wall clock time was about 1 hour.

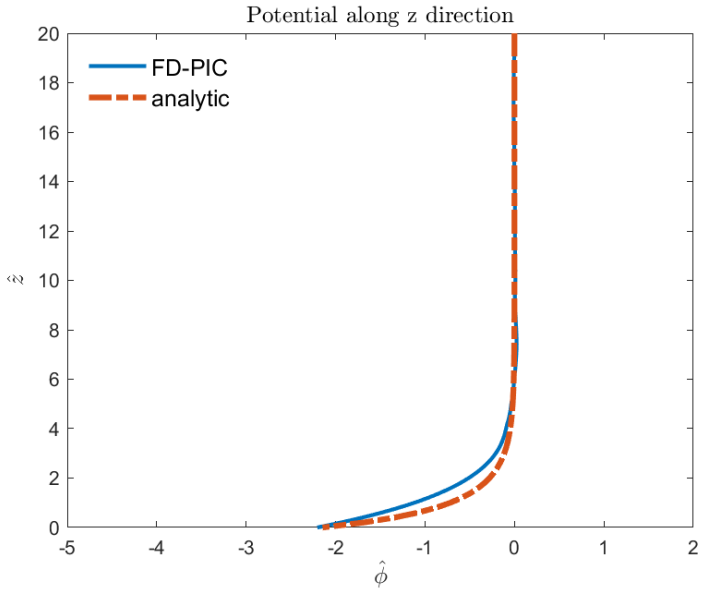

Figure 4.25. Potential along z without object

The comparisons of potential profile between analytic solutions and simulations can be seen in Figures 4.25 - 4.27. From the comparisons we can see that the simulations agree with the analytic solutions very well, which validated the accuracy of the codes.

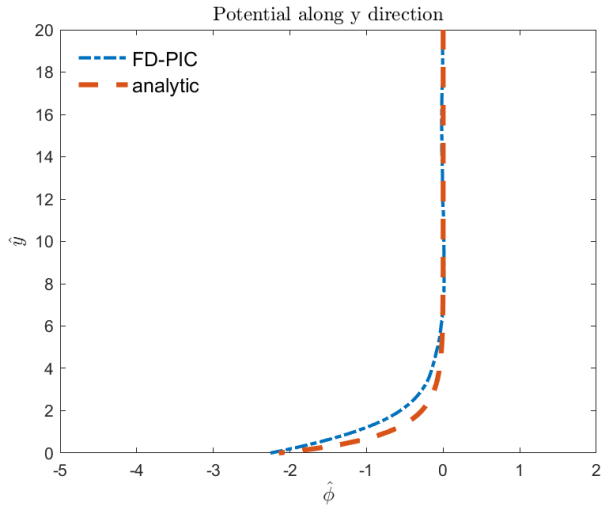

Figure 4.26. Potential along y without object

4.2.2.2. With object. In this section, we will consider a scenario with a cubic object located on an even lunar surface. Since this is a 1-D condition, only the top surface of the object is presented in the computation domain. Again, all surrounding boundaries were considered as "periodic", the top surface of the object was an "absorb" boundary, meaning that once the particle hits this surface, it will be absorbed by the surface and the carried charge will accumulate on the surface. The dimension of the domain was still 2×2×200 PIC cells, the size of the object was 2×2×2 PIC cells, the permittivity of the object was 4.0, the solar wind electrons and ions were injected from the top surface of the computation domain. In total 200,000 simulation particles (100,000 solar wind electrons and 100,000 solar wind ions) were pre-loaded into the computation domain as the initial condition, another 100 solar wind electrons and 100 solar wind ions were injected into the computation domain in each time step (dt = 0.01). The simulation ran about 50,000 steps, which was about 250 seconds in physical units. The wall clock time was about 1 hour.

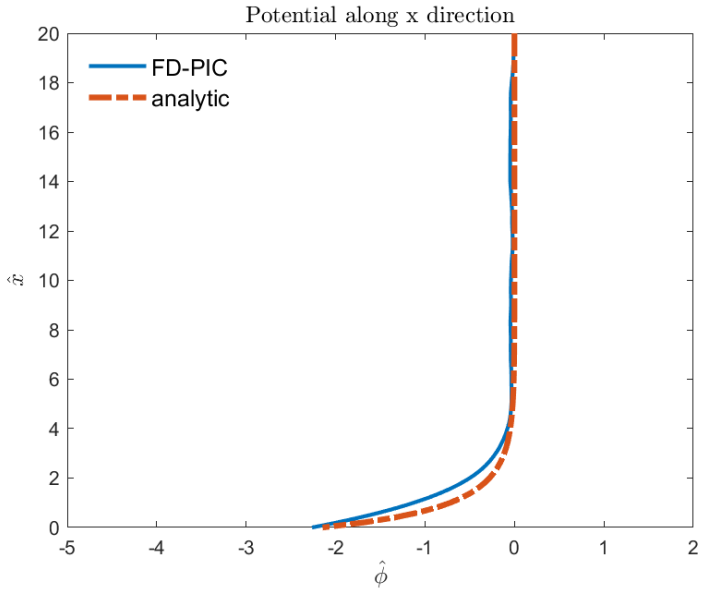

Figure 4.27. Potential along x without object

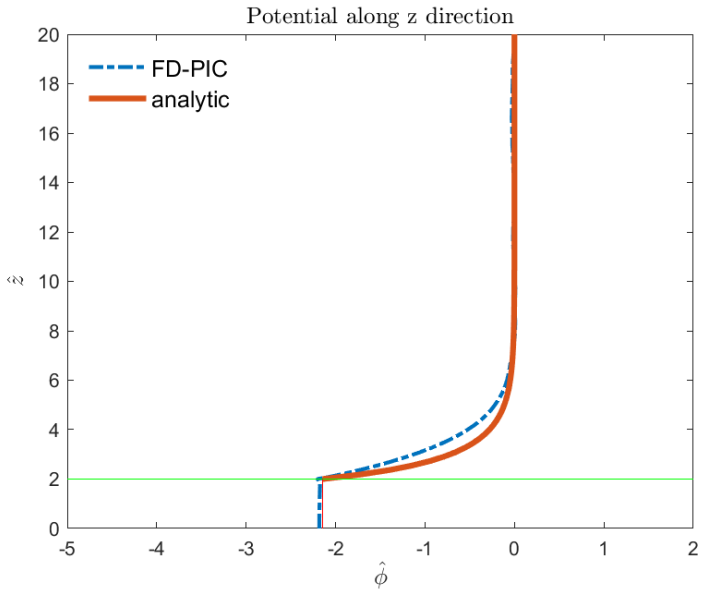

Figure 4.28. Potential along z with object surface

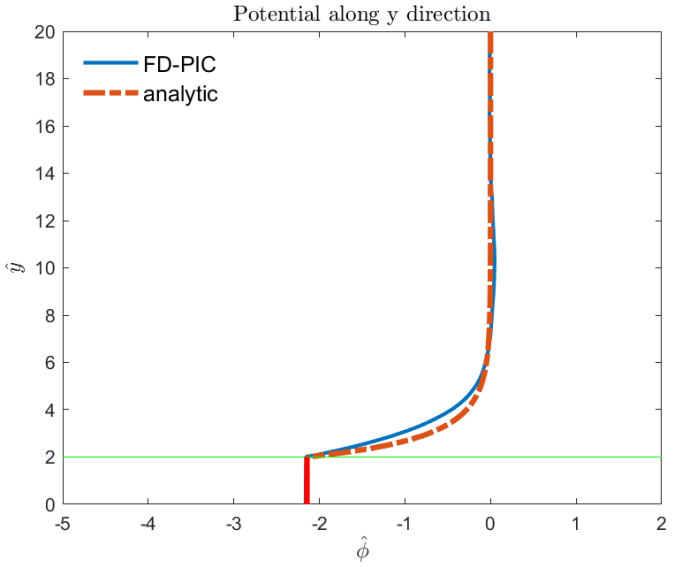

Figure 4.29. Potential along y with object surface

The comparisons of potential profile between simulations and analytic solutions in three directions are shown in Figures 4.28 - 4.30. The good agreements validated the accuracy of the codes.

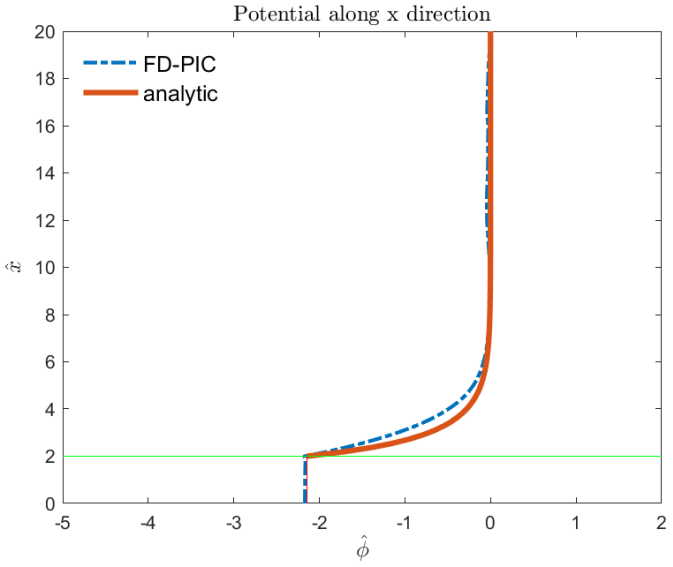

Figure 4.30. Potential along x with object surface

4.3. DERIVATION OF THE 1-D SEMI-ANALYTIC MODEL

In order to investigate the 1-D photoelectron sheath configuration near the lunar surface, we derived a 1-D semi-analytic model to obtain the profiles of quantities of interest as functions of the distance from the lunar surface. The semi-analytic model derived in this section will also be used to validate the FD-PIC code.

In this dissertation, the plasma species include the drifting solar wind protons and electrons, as well as photoelectrons emitted from the lunar surface. It is noted here that although the semi-analytic solution is not *explicit*, it is numerically solvable and thus called "semi-analytic", which also distinguishes itself from the solution with the FD-PIC code.

The derivation process of the governing equations is presented in the following sections. The extensions of each equation can be seen in Appendix A.

4.3.1. Number Densities. The densities of each population of electrons are given in Eq. (4.29).

$$
\begin{aligned}
n_{\mathrm{swe,f}}(z) &= \int_{v_{\mathrm{m}}}^{\infty} n_{\mathrm{swe},\infty} f(v)\mathrm{d}v \\
n_{\mathrm{phe,f}}(z) &= \int_{v_{\mathrm{m}}}^{\infty} n_{\mathrm{phe},0} f(v)\mathrm{d}v \\
n_{\mathrm{swe,r}}(z) &= 2\int_{0}^{v_{\mathrm{m}}} n_{\mathrm{swe},\infty} f(v)\mathrm{d}v \\
n_{\mathrm{phe,c}}(z) &= 2\int_{0}^{v_{\mathrm{m}}} n_{\mathrm{phe},0} f(v)\mathrm{d}v
\end{aligned}
\tag{4.29}
$$

where $n_{\mathrm{swe,f}}$, $n_{\mathrm{phe,f}}$, $n_{\mathrm{swe,r}}$, and $n_{\mathrm{phe,c}}$ represent the densities of free solar wind electrons, free photoelectrons, reflected solar wind electrons, and captured photoelectrons, respectively; $n_{\mathrm{swe},\infty}$ and $v_{\mathrm{swe,th}}$ are density at infinity and thermal velocity of solar wind electrons; $n_{\mathrm{phe},0}$ and $v_{\mathrm{phe,th}}$ are density at the surface and thermal velocity of photoelectrons; $v_{\mathrm{m}} = \sqrt{2e(\phi_{(z)} - \phi_{\mathrm{m}})/m_{\mathrm{swe}}}$ is the minimum velocity required to travel over the potential barrier; The ion density is obtained from continuity as in Eq. (4.30):

$$n_{\mathrm{swi}}(z) = \frac{n_{\mathrm{swi},\infty} v_{\mathrm{swi},\infty}}{v_{\mathrm{swi}}(z)} \tag{4.30}$$

where $n_{\mathrm{swi},\infty}$ and $v_{\mathrm{swi},\infty}$ are density and velocity of solar wind ions at infinity, respectively.

Therefore, Poisson's equation which will be utilized to calculate the potential can be written as Eq. (4.31):

$$\frac{\mathrm{d}^2\phi}{\mathrm{d}z^2} = -\frac{e}{\varepsilon_0}\left[n_{\mathrm{swi}}(z) - n_{\mathrm{swe,f}}(z) - n_{\mathrm{swe,r}}(z) - n_{\mathrm{phe,f}}(z) - n_{\mathrm{phe,c}}(z)\right] \tag{4.31}$$

where ε_0 is the vacuum permittivity.

4.3.2. Charge Neutrality at Infinity. We assume the total charge density at infinity is zero in the sheath model, which can be described as Eq. (4.32):

$$\begin{aligned} &n_{\mathrm{swe}}(\infty) + n_{\mathrm{phe}}(\infty) - n_{\mathrm{swi}}(\infty) = \\ &n_{\mathrm{swe,f}}(\infty) + n_{\mathrm{swe,r}}(\infty) + n_{\mathrm{phe,f}}(\infty) - n_{\mathrm{swi}}(\infty) = 0 \end{aligned} \tag{4.32}$$

4.3.3. Net Current Neutrality at Infinity. We assume there is no net current flow at infinity when the photoelectron sheath reaches the steady state. The zero current density at infinity can be expressed as Eq. (4.33):

$$J_{\mathrm{swe,f}}(\infty) + J_{\mathrm{phe,f}}(0) - J_{\mathrm{swi}}(\infty) = 0 \tag{4.33}$$

It is noted here that the reflected solar wind electrons and the captured photoelectrons have no contribution to the net current at infinity because they both have counterparts traveling in opposite directions.

4.3.4. Electric Field Neutrality at Infinity. Specifically for Type A, there is a minimum potential ϕ_{m} at a distance above the surface z_{m} (Figure 1.2). Therefore, we need another equation to solve it. This additional equation can be obtained from the condition of zero electric field at infinity. The electric field in z-direction can be obtained by integrating Poisson's equation Eq. (4.31).

$$\nabla \cdot \mathbf{E} = \frac{\rho}{\varepsilon_0} \tag{4.34}$$

$$\mathbf{E} = -\nabla\phi \tag{4.35}$$

Applying Gauss' Law as shown in Eqs. (4.34) and (4.35), we can obtain the equations for electric field as shown in Eq. (4.36).

$$\begin{aligned}
E^2_{\mathrm{swe,f}}(z) &= 2\int_{\phi_{\mathrm{m}}}^{\phi_{(z)}} n_{\mathrm{swe,f}}\mathrm{d}\phi \\
E^2_{\mathrm{phe,f}}(z) &= 2\int_{\phi_{\mathrm{m}}}^{\phi_{(z)}} n_{\mathrm{phe,f}}\mathrm{d}\phi \\
E^2_{\mathrm{swe,r}}(z) &= 2\int_{\phi_{\mathrm{m}}}^{\phi_{(z)}} n_{\mathrm{swe,r}}\mathrm{d}\phi \\
E^2_{\mathrm{phe,c}}(z) &= 2\int_{\phi_{\mathrm{m}}}^{\phi_{(z)}} n_{\mathrm{phe,c}}\mathrm{d}\phi \\
E^2_{\mathrm{swi}}(z) &= -2\int_{\phi_{\mathrm{m}}}^{\phi_{(z)}} n_{\mathrm{swi}}\mathrm{d}\phi
\end{aligned} \tag{4.36}$$

where $E_{\mathrm{swe,f}}$, $E_{\mathrm{phe,f}}$, $E_{\mathrm{swe,r}}$, $E_{\mathrm{phe,c}}$, and E_{swi} is the electric field of free solar wind electrons, free photoelectrons, reflected solar wind electrons, captured photoelectrons, and solar wind ions, respectively;

The zero electric field condition at infinity can then be described as Eq. (4.37):

$$E^2(\infty) = E^2_{\mathrm{swe,f}}(\infty) + E^2_{\mathrm{swe,r}}(\infty) + E^2_{\mathrm{phe,f}}(\infty) + E^2_{\mathrm{swi}}(\infty) = 0 \tag{4.37}$$

4.3.5. Solving Poisson's Equation. In order to obtain the profiles of quantities of interest, such as potentials and electric fields, within the photoelectron sheath as a function of the distance from the lunar surface z, we need to numerically solve Poisson's equation as given in Eq. (4.31).

For Type B and Type C photoelectron sheath structure as introduced in Section 1.1.2.3, there are two unknowns, which are the surface potential, ϕ_0, and the density of solar wind electron at infinity, $n_{\mathrm{swe},\infty}$. These two unknowns can be obtained from the charge neutrality equation Eq. (4.32), and the zero current density equation Eq. (4.33).

For Type A photoelectron sheath structure as introduced in Section 1.1.2.3, since the potential is non-monotonic, there will be one more unknown which is the potential at the potential barrier, ϕ_{m}. Therefore we need to solve one more equation which is the zero electric field equation Eq. (4.37) to get all the unknowns.

Once both/all unknowns are obtained, we can evaluate the property profiles as functions of distance from the surface.

After obtaining the semi-analytic solutions, we utilize a FD-PIC code (Wang *et al.* (2008); Zhao *et al.* (2020a)) to perform fully-kinetic particle simulations of the photoelectron sheath. The trajectories of charged species (solar wind ions, solar wind electrons, and photoelectrons), as well as the electrostatic field including surface charging, are solved self-consistently.

4.4. VALIDATION OF THE FD-PIC CODE

In this section, we will compare the profiles of quantities of interest that obtained with the semi-analytic model and the FD-PIC simulations of 1-D photoelectron sheath configuration. A fully-kinetic particle simulation was ran to self-consistently solve the trajectories of charged species (solar wind ions, solar wind electrons, and photoelectrons) as well as the electrostatic field including surface charging (Wang *et al.* (2008); Zhao *et al.* (2020b)).

In a typical FD-PIC simulation, 180,000 macro-particles representing each species of the solar wind, i.e., ions and electrons, 360,000 macro-particles total, were pre-loaded into the computation domain as the initial condition, and another about 100 macro-particles representing each charged species, including photoelectrons, were injected into the computation domain at each PIC time step. A typical simulation ran till at about 100,000 PIC steps ($\simeq$ 900 seconds in physical units) when results were taken to do post-processing. The wall-clock time was typically about 6 hours for each case.

4.4.1. Solar Wind and Photoelectron Conditions. For 1-D photoelectron sheath structure, the solar wind condition and photoelectron parameters are chosen the same as that introduced in Gosling (2007). The drifting velocity of the solar wind electrons and ions are both 468 km/s. The densities of the electrons (solar wind electrons and photoelectrons in total) and ions at infinity are both 8.7 cm^{-3}, and the thermal temperatures are 12 eV and 10 eV, respectively. The parameters used in these calculations are listed in Table 4.1 ((α is the Sun elevation angle)). Since the study in this section focuses on a 1-D sheath problem, the lunar surface is considered as an even surface.

Table 4.1. Solar wind and photoelectron parameters

	electrons	ions	photoelectrons
Drifting Velocity, km/s	468	468	-
Density, cm^{-3}	8.7	8.7	64 $\sin(\alpha)$
Temperature, eV	12	10	2.2

4.4.2. Computation Domain and Normalization. In order to simulate a 1-D photoelectron sheath, a rectangular computation domain is set up as shown in Figure 4.31. The solar wind electrons and ions are traveling into the computation domain through the X-Y plane, along -z-direction.

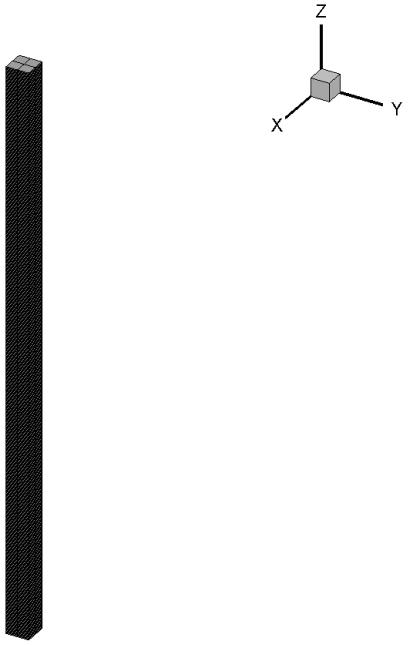

(a) The entire computation domain

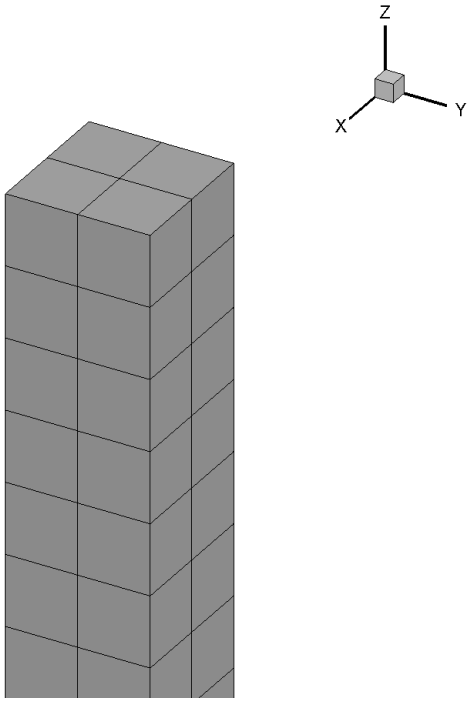

(b) Top surface zoom-in view of the computation domain

Figure 4.31. 1-D computation domain of the FD-PIC simulations

Length is normalized by the Debye length of the photoelectron at 90° Sun elevation angle, which is $\lambda_d = \sqrt{\varepsilon_0 k T_{\text{phe}} / n_{\text{phe,ref}} e^2} \simeq 1.38$ m. The mesh size is $0.1\lambda_{\text{d}}$. The PIC time is normalized by $1/\omega_{\text{phe}}$, where ω_{phe} is the plasma frequency of the photoelectron at normal incidence condition (90°). Table 4.2 shows the normalization references used in this dissertation, where λ_d is the Debye length of the photoelectron at 90° Sun elevation angle, ε_0 is the vacuum permittivity, k is the Boltzmann constant, T_{phe} is the temperature of the photoelectron, $n_{\text{phe,ref}}$ is the photoelectron number density at 90° Sun elevation angle, e is the electric charge, m_{phe} is the mass of the photoelectron, and $v_{\text{phe,t}} = \sqrt{kT_{\text{phe}}/m_{\text{phe}}}$ is the reference for velocity.

Table 4.2. Normalization references

L_{ref}	T_{ref}	m_{ref}	ϕ_{ref}	v_{ref}	n_{ref}	t_{ref}
λ_d	T_{phe}	m_{phe}	$\frac{kT_{\text{phe}}}{e}$	$v_{\text{phe,t}}$	$n_{\text{phe,ref}}$	$\frac{1}{\omega_{\text{phe}}}$

4.4.3. Boundary Conditions. Zero-Dirichlet boundary condition $\phi = 0$ is applied to the Z_{max} boundary, which is treated as the reference of the electric potential. At the Z_{min} boundary, surface charging is taken into account from the charge deposition. At the four boundaries along x- and y-directions, zero-Neumann boundary condition such that $\frac{\partial \phi}{\partial n} = 0$ is applied.

Macro-particles representing solar wind electrons and ions are pre-loaded into the domain and injected at Z_{max} boundary. Macro-particles representing photoelectrons are emitted at the lunar surface at Z_{min}. Particles hitting Z_{min} are absorbed and taken into account for surface charging. Particle hitting Z_{max} are removed from the computation. Periodic particle boundary conditions are applied at boundaries along x-direction, while reflective particle boundary conditions are applied at boundaries along y-direction. Since the photoelectron sheath problem in this study is 1-D, the results are not sensitive to particle boundary conditions along x- or y-directions.

4.4.4. FD-PIC Simulation Results and Discussions. In order to validate the FD-PIC code and test the accuracy of the 1-D semi-analytic model derived in Section 4.3, the profiles of quantities of interest obtained with the numerical simulations were compared with that of the semi-analytic model. Since the two approaches are independent to each other, a good agreement of the comparisons between these two results can be utilized to verify the accuracy of both the FD-PIC code and the semi-analytic model.

4.4.4.1. Type A photoelectron sheath. Figure 4.32 shows the comparisons of the potential profiles between semi-analytic solutions and FD-PIC simulations for Sun elevation angles of 60° and 90°. Good agreement is observed. For 60° Sun elevation angle, the Type A sheath potential reaches zero near $\hat{z} = 50$ (about 69 m) above the surface, whereas for 90° Sun elevation angle (lunar equator), the Type A sheath potential reaches zero near $\hat{z} = 40$ (about 55 m) above the surface.

We also compared the profiles of total charge density, solar wind electron density, solar wind ion density, photoelectron density, and vertical electric field obtained from the semi-analytic solutions and the FD-PIC simulations for Type A at 60° and 90° Sun elevation angles. These comparisons are shown in Figure 4.33 and Figure 4.34. These results of the comparisons show that all densities and electric fields obtained from semi-analytic solutions and the FD-PIC simulations match very well for both 60° and 90° Sun elevation angles. This validates our new 1-D photoelectron sheath model as well as verifies the FD-PIC simulations.

4.4.4.2. Type B photoelectron sheath. When the Sun elevation angle is large enough, the profiles of Type A and Type B can co-exist at the same time in both semi-analytic solution and the particle simulation. Figure 4.35 shows the Type B potential profiles within the sheath at the same Sun elevation angles as for Type A. Again good agreement is shown. Compared with Type A sheaths at the same Sun elevation angles, the Type B sheaths are much thinner, i.e., sheath potentials reach zero at about $\hat{z} = 10$ (about

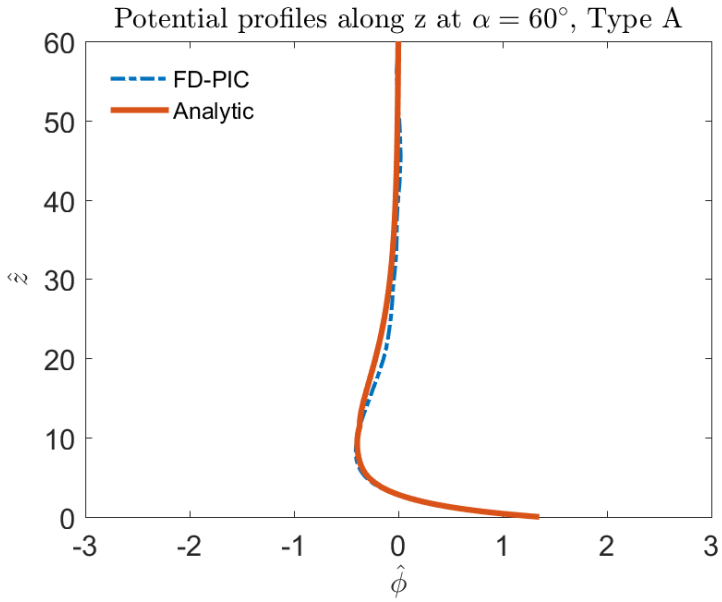

(a) α = 60°

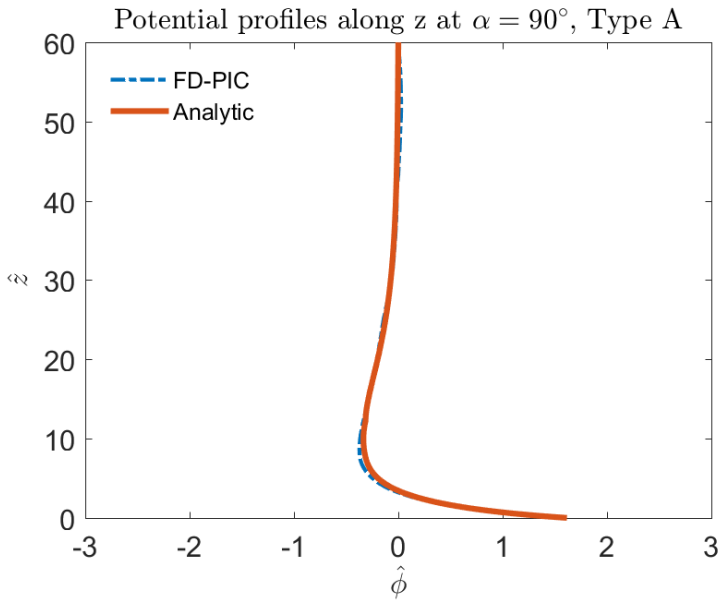

(b) α = 90°

Figure 4.32. Comparisons of Type A potential profiles obtained from semi-analytic solutions and FD-PIC simulations

14 m) for both 60° and 90° Sun elevation angles. The reason of the difference of potential between Type A and Type B is that, according to the assumption, at infinity the solar wind

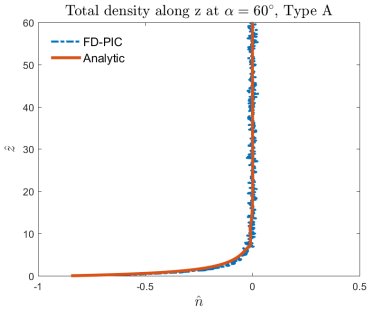

(a) Total density at $\alpha = 60°$

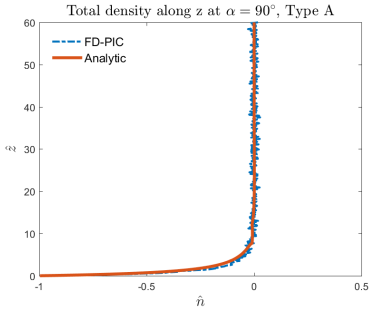

(b) Total density at $\alpha = 90°$

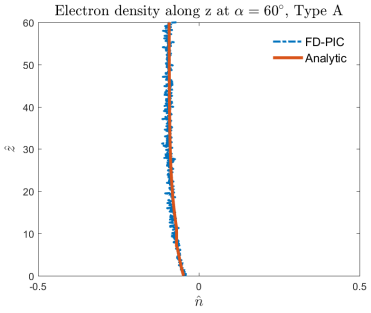

(c) Electron density at $\alpha = 60°$

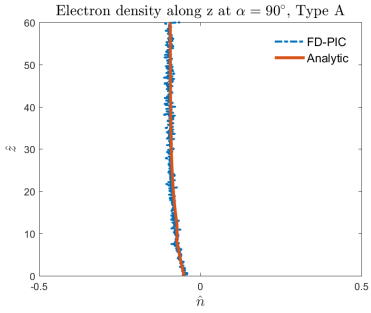

(d) Electron density at $\alpha = 90°$

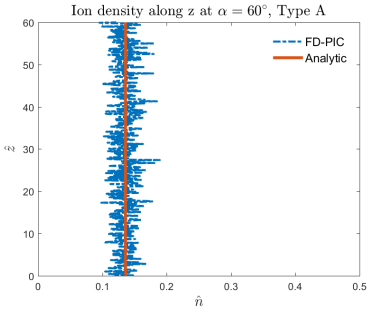

(e) Ion density at $\alpha = 60°$

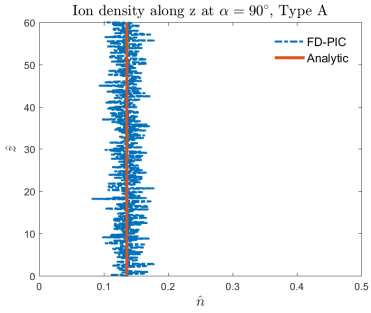

(f) Ion density at $\alpha = 90°$

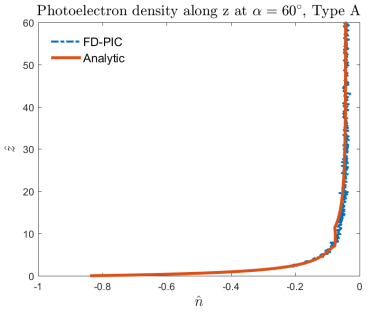

(g) Photoelectron density at $\alpha = 60°$

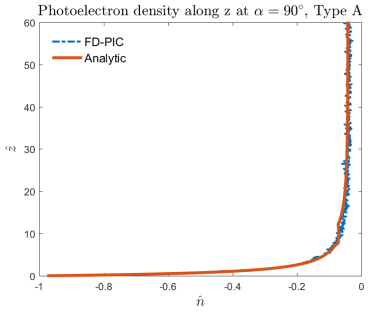

(h) Photoelectron density at $\alpha = 90°$

Figure 4.33. Comparisons of the Type A densities at different Sun elevation angles

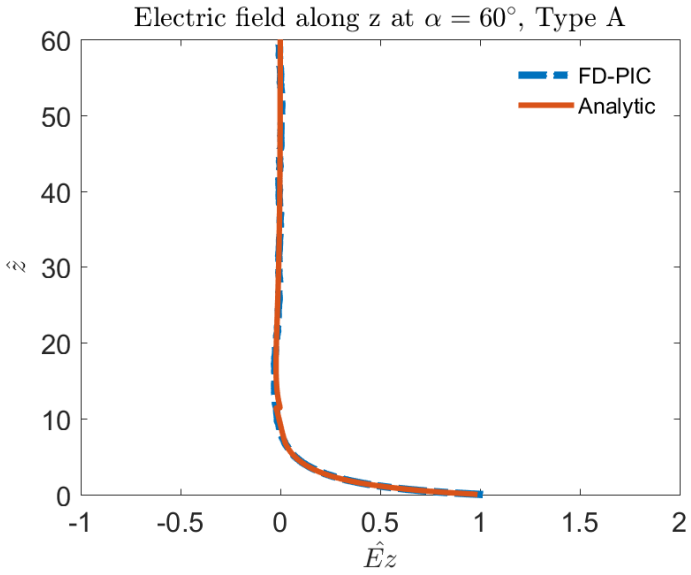

(a) Electric field at $\alpha = 60°$

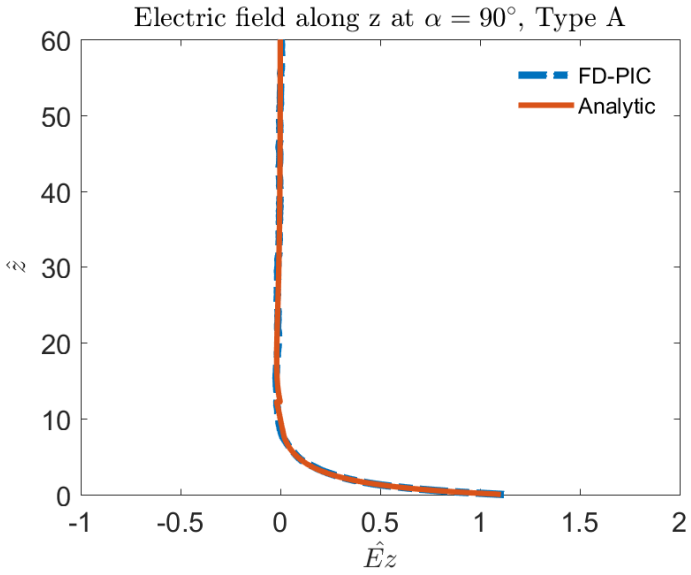

(b) Electric field at $\alpha = 90°$

Figure 4.34. Comparisons of the Type A electric fields at different Sun elevation angles

electron density $n_{\text{swe},\infty}$ is not equivalent to the solar wind ion density $n_{\text{swi},\infty}$. In Type A, $n_{\text{swe},\infty}$ is larger than that in Type B, leading to an overall lower potential profile (see Figure 4.32).

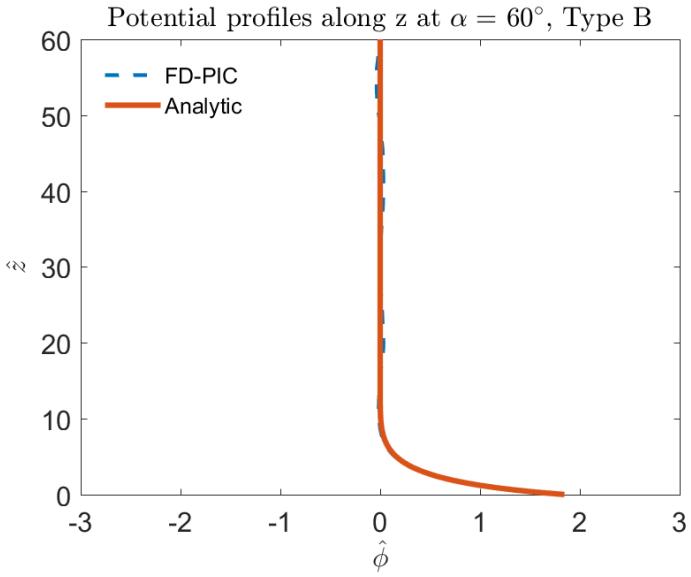

(a) $\alpha = 60°$

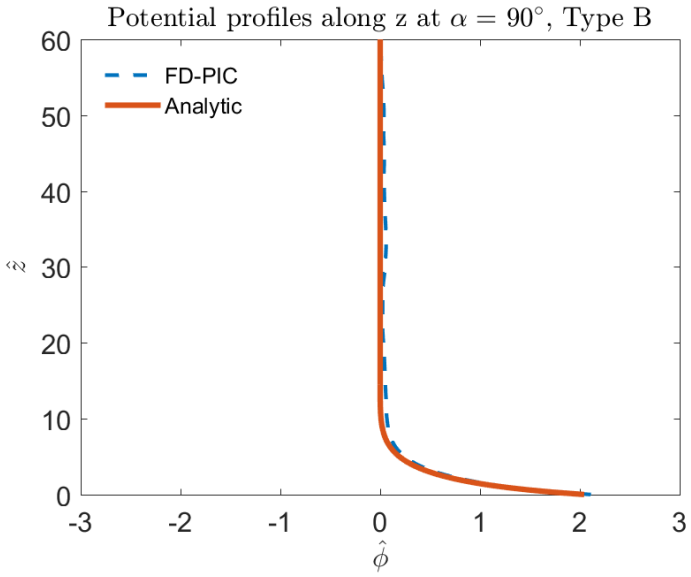

(b) $\alpha = 90°$

Figure 4.35. Comparisons of Type B potential profiles obtained from semi-analytic solutions and FD-PIC simulations

4.4.4.3. Type C photoelectron sheath. Figure 4.36 shows the comparisons of the Type C potential profiles between semi-analytic solutions and FD-PIC simulations for Sun elevation angles of 5° and 10°. Again good agreement is shown as for Type A and Type B profiles. At 5° Sun elevation angle, the Type C sheath potential reaches zero near $\hat{z} = 60$

(about 83 m) above the surface, whereas for 10° Sun elevation angle, the Type C sheath potential reaches zero near $\hat{z} = 30$ (about 41 m) above the surface, due to a less-negative surface potential.

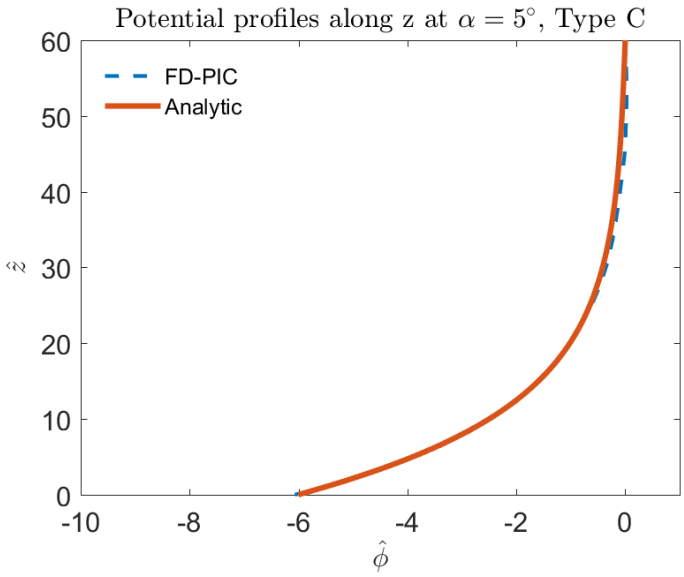

(a) $\alpha = 5°$

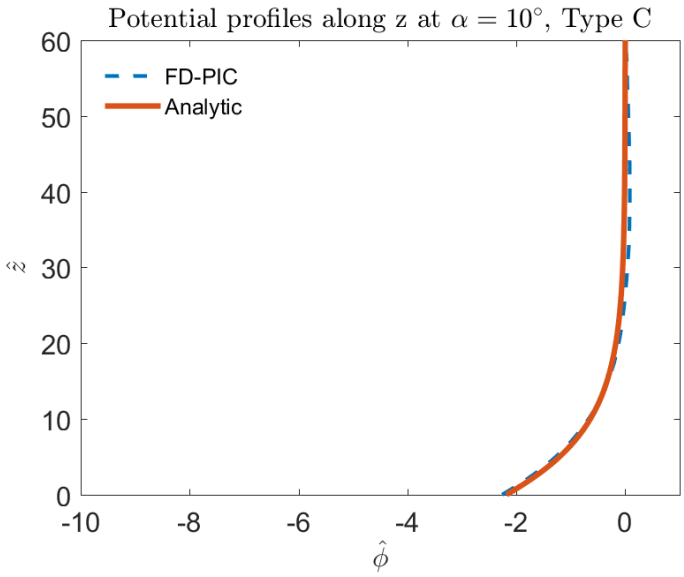

(b) $\alpha = 10°$

Figure 4.36. Comparison of Type C potential profiles obtained from semi-analytic solutions and FD-PIC simulations

Overall, for all three types of photoelectron sheaths considered in our model, good agreements between semi-analytic solutions and FD-PIC simulations are obtained. Results show that under average solar wind condition, the photoelectron sheath may reach as high as close to 100 m above the flat lunar surface near the terminator region, and up to about 50 m near the equator region.

4.4.5. Influence of Drifting Electrons. As introduced in the derivation of the semi-analytic model in Section 4.3, one of the contributions of this dissertation is the consideration of the drifting velocity of solar wind electrons when resolving the electrostatic environment in the photoelectron sheath near the lunar surface. In this section, we will show some comparisons of the potential profile between stationary and drifting solar wind electrons at different Sun elevation angles to demonstrate the importance of taking into account of the drifting electrons.

The potential profiles with and without the consideration of the drifting electrons at different Sun elevation angles are shown in Figures 4.37 - 4.39.

The comparisons show that there is a clear difference in the potential profile when taking into account of drifting solar wind electrons for all Sun elevation angles. When the drifting velocity is considered, the potential decreases compared with those of the stationary electrons. It is reasonable because the drifting velocity at the boundaries will increase the quantity of electrons injected into the computation domain, and more electrons leads to decreased potential within the photoelectron sheath.

4.5. SUMMARY

In this section, we presented the details of the setup of the simulations, and validated the code by comparing the simulations of the 1-D photoelectron sheath configurations with the solutions obtained with the 1-D semi-analytic model we derived in Section 4.3.

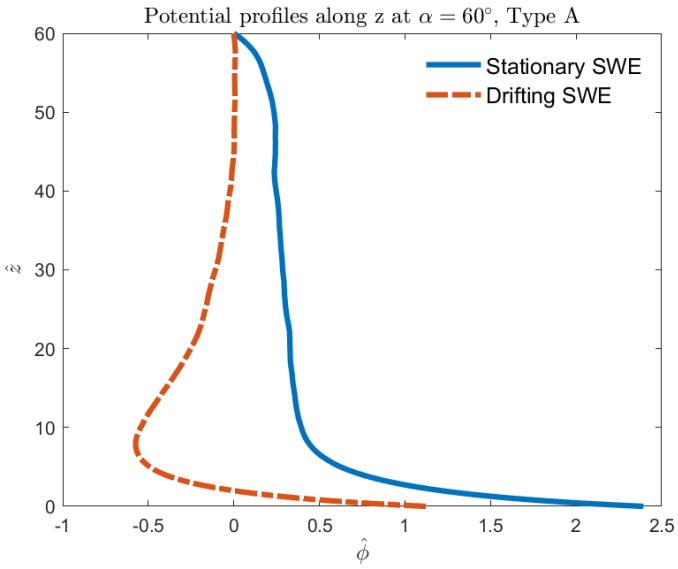

(a) $\alpha = 60°$

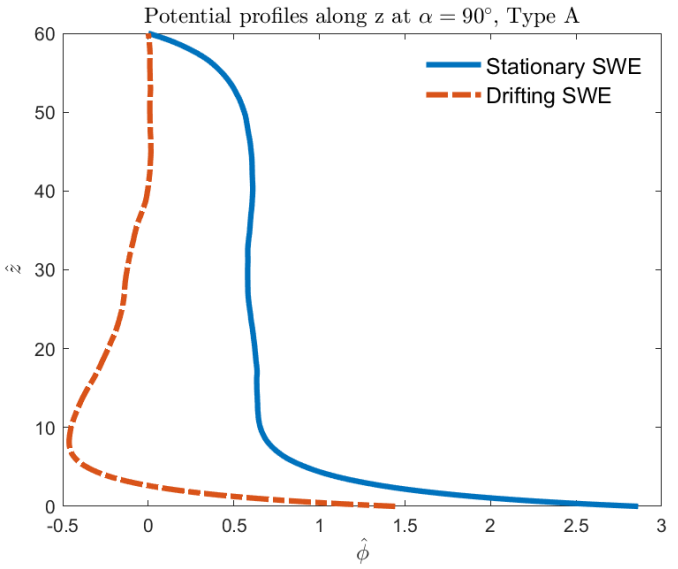

(b) $\alpha = 90°$

Figure 4.37. Potential obtained with stationary and drifting solar wind electrons, Type A

Two velocity probability distributions, *Maxwellian* and κ-distribution were discussed in this section for both loaded and injected particles. The specific methods to generate velocities that following these distributions in simulations were introduced and tested.

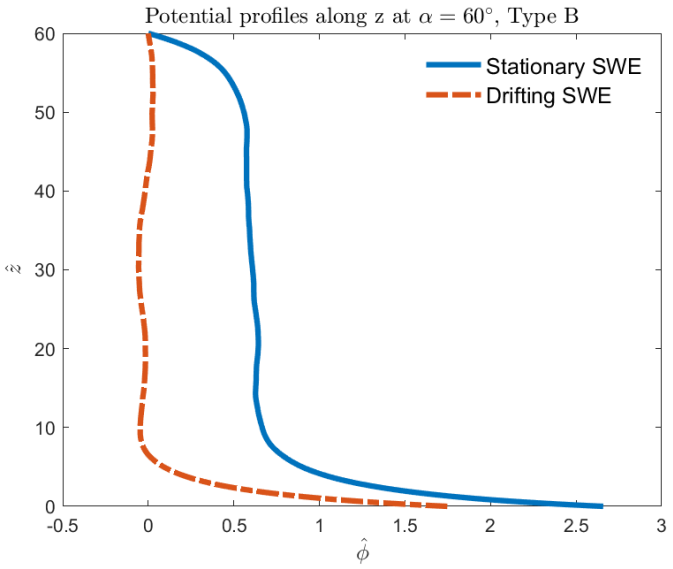

(a) $\alpha = 60°$

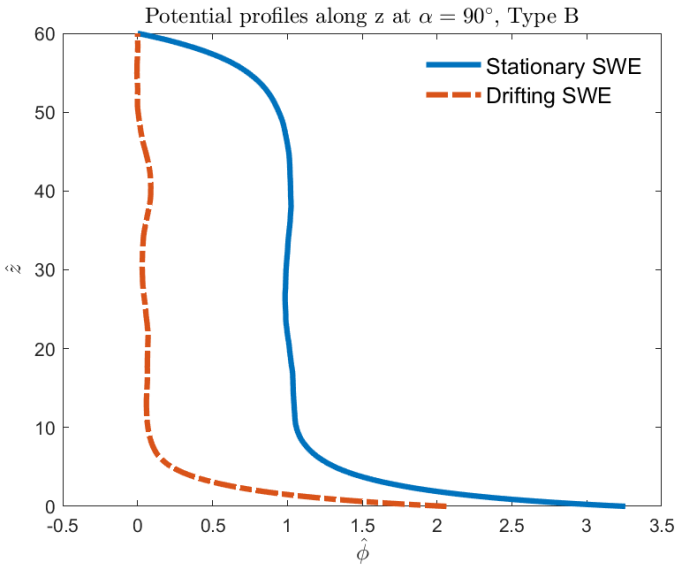

(b) $\alpha = 90°$

Figure 4.38. Potential obtained with stationary and drifting solar wind electrons, Type B

We also tested the accuracy of the field solver in the code by comparing the simulations with analytic solutions under different conditions, good agreements were obtained, which validated the accuracy of the solver code.

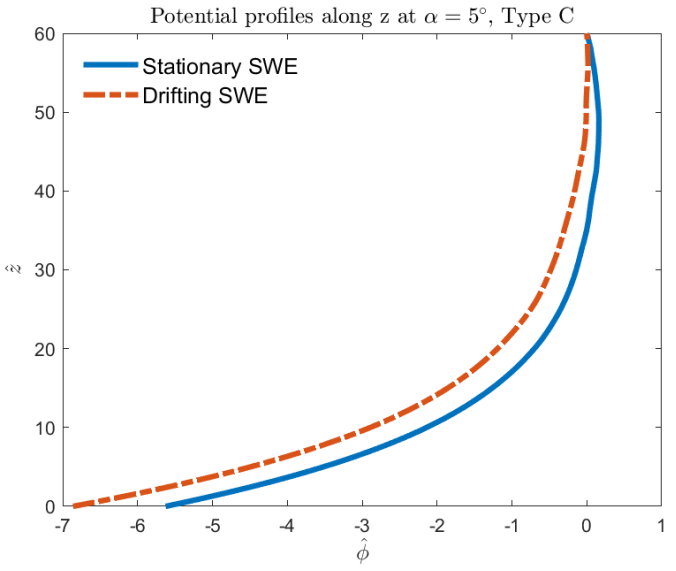

(a) $\alpha = 5°$

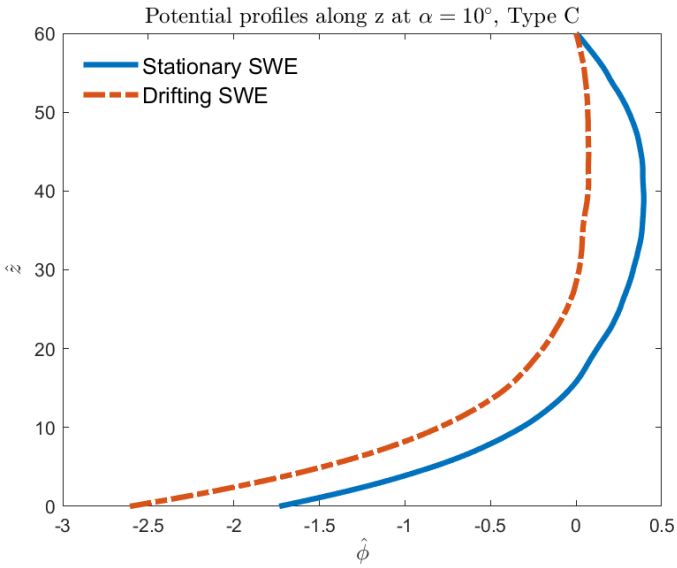

(b) $\alpha = 10°$

Figure 4.39. Potential obtained with stationary and drifting solar wind electrons, Type C

We also showed the necessity of taking into account of the drifting velocity of the solar wind electrons in the simulations by comparing the profiles of quantities of interest obtained with and without considering the drifting electrons. The significant difference between the potentials showed how important it is to account for the influence of drifting solar wind electrons.

5. SURFACE-PLASMA INTERACTIONS ON THE MOON

In this section, we will present the investigation of the plasma environment near the lunar surface with the semi-analytic 1-D photoelectron sheath model and the FD-PIC simulations. The plasma species include the cold solar wind protons, drifting *Maxwellian* solar wind electrons, and *Maxwellian* photoelectrons emitted from sunlit surfaces. The 1-D semi-analytic model will be used to numerically obtain the profiles of quantities of interest as functions of the vertical distance from the surface. The FD-PIC code will be used to simulate electrostatic environment within the 1-D photoelectron sheath configuration. A κ-distribution of solar wind electrons will also be implemented to the FD-PIC code to compare with the *Maxwellian* velocity distribution. Then the FD-PIC code will be used to simulate the 2-D photoelectron sheath configuration. In Section 5.1, we will introduce the considerations of the *Maxwellian* and κ-distribution in the simulations, and show the comparisons between these two distributions. In Section 5.2, we will present the simulations of 2-D configurations of the photoelectron sheath. A brief summary of this section will be given in Section 5.3.

5.1. *MAXWELLIAN* AND κ-DISTRIBUTION

In our simulations, we considered both *Maxwellian* and κ-distribution of solar wind electrons. In this sections, we will introduce the details and compare the difference between theses two distributions.

5.1.1. *Maxwellian* Distribution of Solar Wind Electrons. The velocity distribution of solar wind electrons were assumed following the *Maxwellian* distribution in the first round of our simulations. The details of the *Maxwellian* velocity distribution has been introduced in Section 4.1. Furthermore, the electrons in our semi-analytic model were also following the *Maxwellian* velocity distribution.

The structure of the photoelectron sheath for this specific 1-D simulation was introduced in Section 1.1.2.3. All three types of photoelectron sheath as presented in Figure 1.2 were considered in this dissertation, and the 1-D profiles of quantities of interest at certain Sun elevation angles that obtained with simulations were compared with the semi-analytic solutions to validate the simulation codes. The details of the derivation of the semi-analytic model for this 1-D photoelectron sheath (the governing equations were introduced in Section 4.3) can be found in Appendix A.

In order to obtain the profiles of the quantities of interest, such as potentials and electric fields, within the photoelectron sheath as functions of the distance from the lunar surface, we need to numerically solve Poisson's equation. For Type B and Type C photoelectron sheath, there are two unknowns: the surface potential ϕ_0, and the density of solar wind electrons at infinity $n_{\mathrm{swe},\infty}$. These two unknowns can be obtained by solving the charge neutrality equation (Eq. (4.32)) and the zero current density equation (Eq. (4.33)). For Type A, since the potential is non-monotonic, there is one more unknown variable which is the potential at the potential barrier ϕ_{m}. Therefore, we need to solve one more equation which is the zero electric field equation (Eq. (4.36)) to obtain all the unknowns. Figure 5.1 shows a flowchart of detailed steps to numerically derive the semi-analytic sheath model.

Once both/all unknowns are obtained, we can evaluate the property profiles as functions of vertical distance from the surface. Figure 5.2 shows an example of the potential profiles for a Type C photoelectron sheath. Two domain lengths in z-direction, one of $Z_{\mathrm{max}} = 100$ and the other of $Z_{\mathrm{max}} = 200$, are compared. It is noticed that the potential reaches zero beyond *normalized* height $\hat{z} = 50$, thus there is negligible difference between the results obtained with $Z_{\mathrm{max}} = 100$ and $Z_{\mathrm{max}} = 200$. Therefore, the computation cost can be reduced by decreasing the height of the computation domain to a range within which the top surface can be properly considered as "infinity" in the simulations.

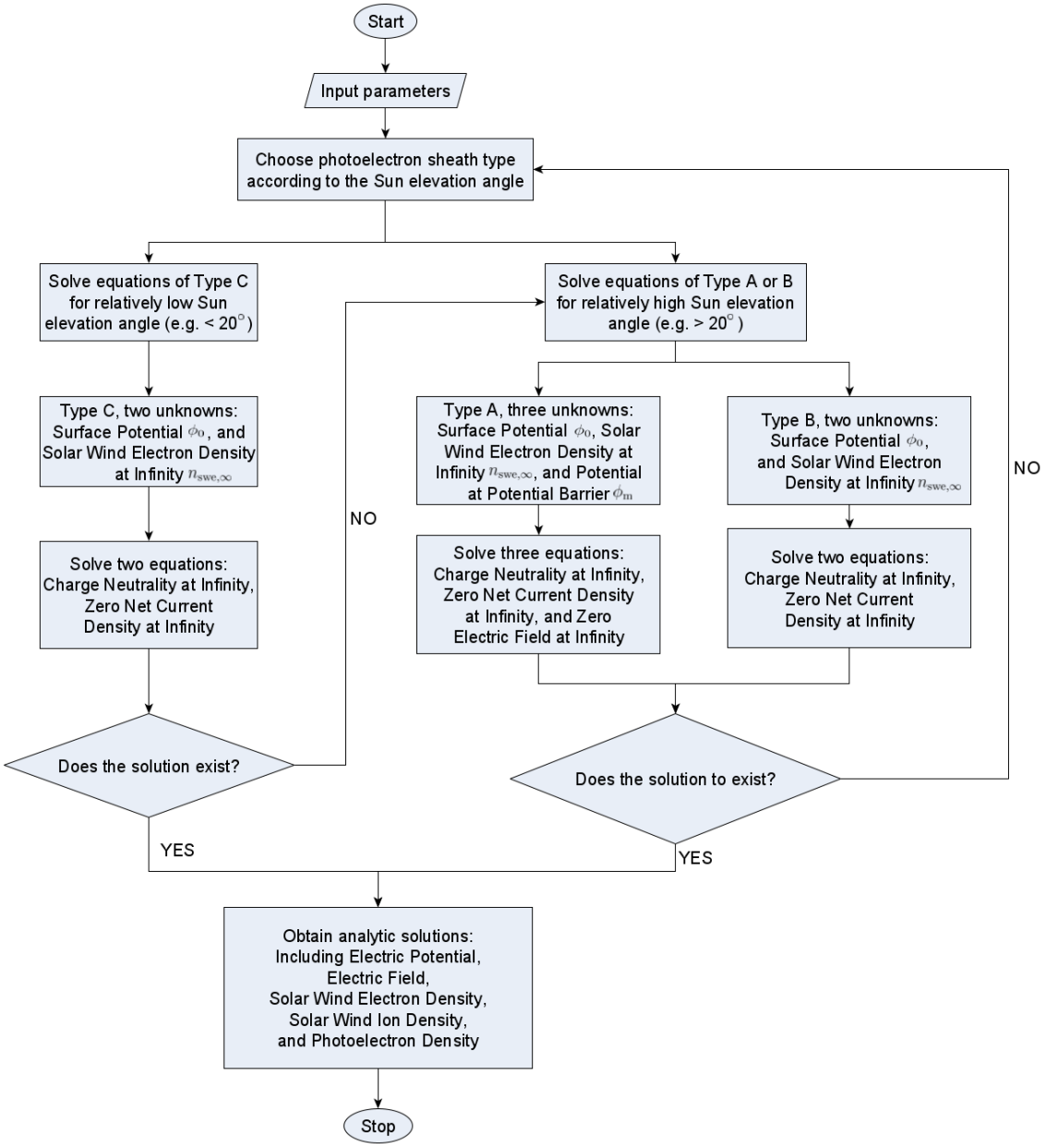

Figure 5.1. Flowchart to solve the semi-analytic sheath model.

5.1.2. κ-distribution of Solar Wind Electrons. In addition to the *Maxwellian* velocity distribution, we also considered the κ-distribution, as introduced in 4.1.1.2, to describe the motion of the solar wind electrons in our second round of simulations, and investigated the difference of these two distributions by comparing the results with each

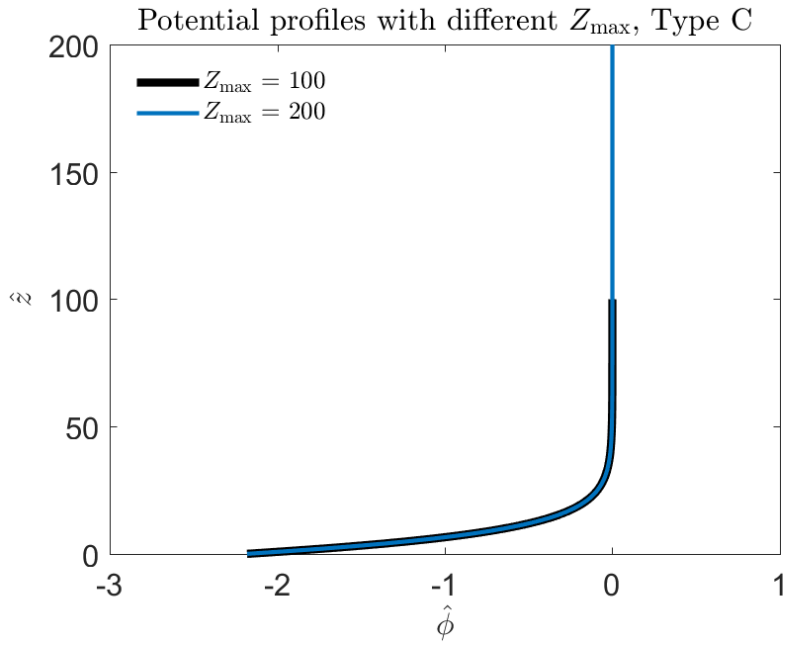

Figure 5.2. Example potential profiles for Type C photoelectron sheath. The "hat" on ϕ and z denotes "normalized".

other in this dissertation. As introduced in Section 4.1.1.2, the analytic expressions of the 1-D stationary and drifting κ-distribution are shown in Eqs. (4.8) and (4.9). Different from the *Maxwellian* velocity distribution, whose probability curve is always the same for certain drifting velocities, the probability curve of the κ-distribution can be influenced by the κ coefficient. Figure 5.3 shows a comparison of a few κ-distributions with different κ coefficient and *Maxwellian* velocity distribution (all with the same v_{th}). It should be noted that, in the limiting case of $\kappa \longrightarrow \infty$, the profile of the κ-distribution approaches to that of the *Maxwellian*, which is considered as a special case, and provides an easy way to compare the results with the semi-analytic solution obtained with *Maxwellian* electrons.

5.1.3. Comparison of *Maxwellian* and κ-distribution. After running two rounds of simulations, we compared the property quantities obtained with κ-distribution with that obtained with the *Maxwellian*. The setup of the FD-PIC simulations was exactly the same as

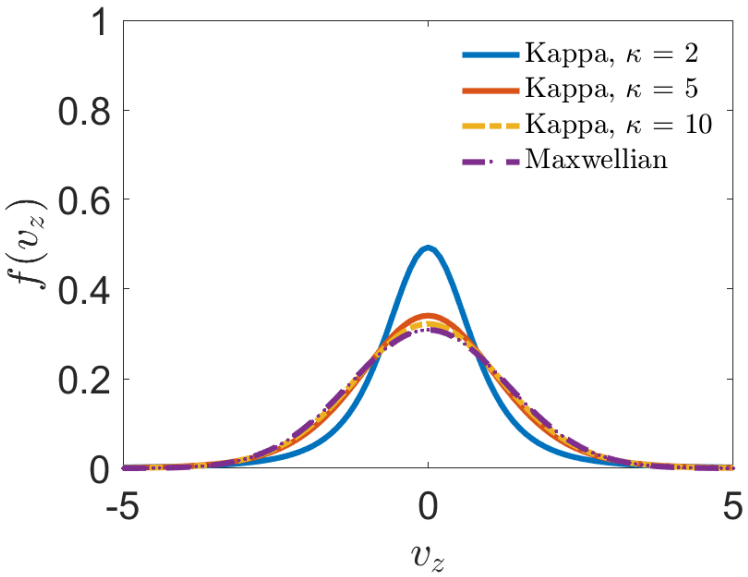

Figure 5.3. The comparison between the *Maxwellian* and κ-distribution

the validation cases described in Section 4.4, except that in the second round of simulations, the velocity distribution was changed from *Maxwellian* to κ-distribution with $\kappa = 4.5$ for the average solar wind condition (Farrell *et al.* (2007); Halekas *et al.* (2005a, 2014)).

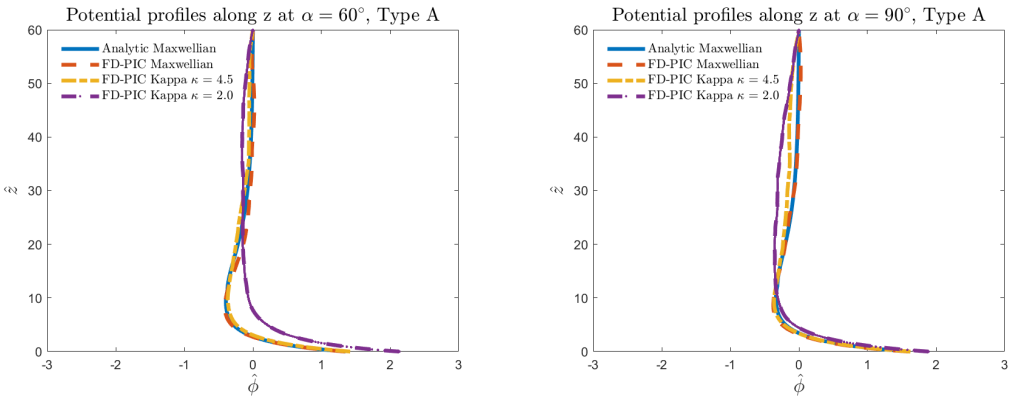

(a) Type A, $\alpha = 60°$ (b) Type A, $\alpha = 90°$

Figure 5.4. Comparison of the electric potential profiles for Type A between *Maxwellian* and κ distributions

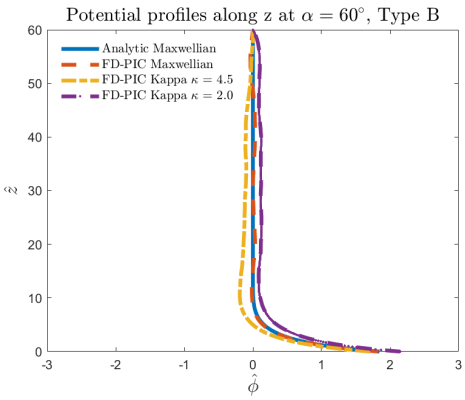

(a) Type B, $\alpha = 60°$

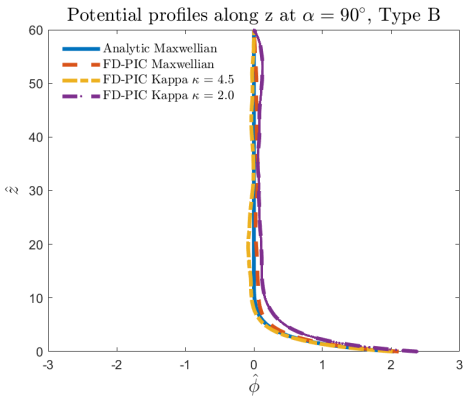

(b) Type B, $\alpha = 90°$

Figure 5.5. Comparison of the electric potential profiles for Type B between *Maxwellian* and κ distributions

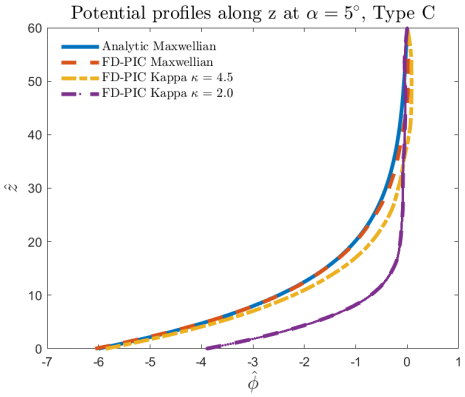

(a) Type C, $\alpha = 5°$

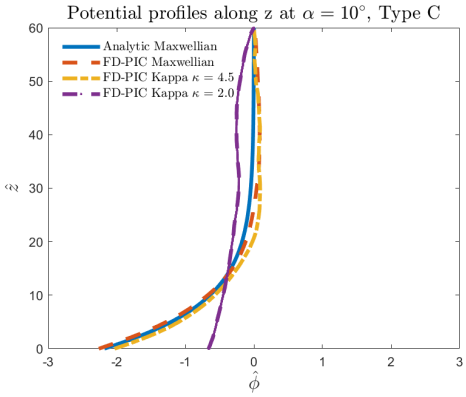

(b) Type C, $\alpha = 10°$

Figure 5.6. Comparison of the electric potential profiles for Type C between *Maxwellian* and κ distributions

Figures 5.4 - 5.6 show the comparisons of the electric potential profiles between the *Maxwellian* and the κ-distribution for Type A, B, and C photoelectron sheath at various Sun elevation angles. As it can be seen from the comparisons, the overall electric potential profiles of the κ-distribution for all three types of photoelectron sheath show similar properties as those of the *Maxwellian*. The reason is that, as the spectral index κ increases, the

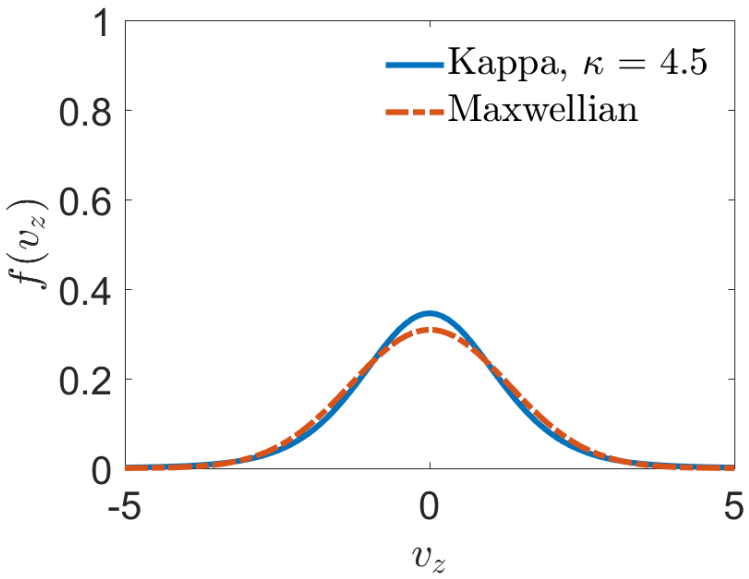

Figure 5.7. *Maxwellian* and κ distributions for solar wind electrons under average solar wind condition

probability profile of the κ-distribution approaches to that of the *Maxwellian*. And for the average solar wind condition, the two probability profiles will only show a slight difference with respect to the change of the Sun elevation angle, which is shown in Figure 5.7.

However in detail, there are still some differences between *Maxwellian* and κ-distribution results. For Type A, the electric potential calculated from the κ-distribution is slightly larger than that calculated from the *Maxwellian* above a certain height near $\hat{z} = 15$ (about 21 m) from the lunar surface for both 60° and 90° Sun elevation angle. Below this certain height, the electric potential obtained with the *Maxwellian* becomes a little larger.

For Type B, the potential calculated from the *Maxwellian* is larger than that calculated from the κ-distribution within the entire photoelectron sheath (up to about 83 m). This tendency is more obvious for the situation of a lower Sun elevation angle.

For Type C, as is similar for Type A, the potential profiles of the *Maxwellian* and the κ-distribution intersect at a certain height near $\hat{z} = 20$ (about 27 m). The potential of the *Maxwellian* is a little larger than that of the κ-distribution above this certain height. Below this certain height, the electric potential of the κ-distribution becomes larger.

In summary, in the average solar wind situation, the electric potential profile (and other quantities of interest) of the *Maxwellian* is very close to those of the κ-distribution.

5.2. SIMULATIONS OF 2-D CONFIGURATIONS

In this section, we will investigate the 2-D photoelectron sheath configurations at the lunar terminator region with the considerations of the two distributions. Specifically, we will study the plasma charging of a box-shaped object on a convex lunar surface, and a rectangular pit on a concave lunar surface under the Sun elevation angle of 10°. Such configurations represent typical surface infrastructures for future lunar colonies.

Similar to the study of 1-D configuration of photoelectron sheath, the objective of investigating the 2-D configuration is to determine the 2-D profiles of quantities of interest within the photoelectron sheath. Furthermore, in the 2-D studies, the parameters of each quantities can be presented by the 2-D contours, providing a more obvious photoelectron sheath structure.

5.2.1. Computation Domain. In the simulations of convex surface, a box-shaped object is located on a flat lunar surface with a shadow region behind, as shown in Figure 5.8(b). Whereas in the simulations of concave surface, a rectangular pit is located in the center of the lunar surface, and nearly half of the bottom surface inside the pit is covered in shadow, as shown in Figure 5.9(b). The solar wind electrons and ions are traveling into the computation domain through the X-Y plane, along -z-direction.

5.2.2. Solar Wind Parameters. Since the study in this dissertation focuses on the terminator region, the Sun elevation angle in the simulations was set as 5° ~10°. The low Sun elevation angle will provide a horizontal component of solar wind velocity (the reason

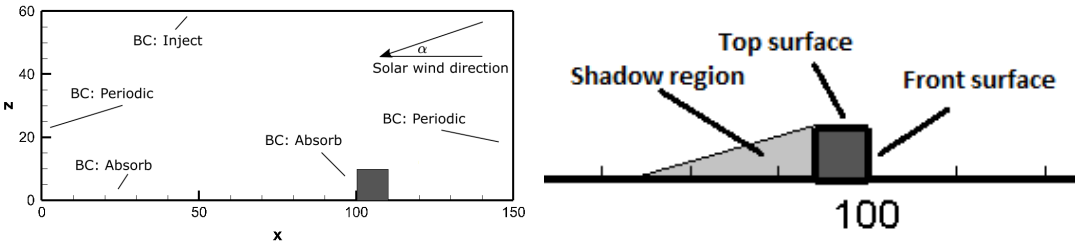

(a) Computation domain of the convex surface (b) Zoom-in view of the box-shaped object

Figure 5.8. Convex surface

why the boundary condition along y was set as "periodic" instead of "reflective"). The photoelectron is also considered in this case with a temperature of 2.2 eV. The parameters of the solar wind and photoelectrons are listed in Table 5.1 (where α is the Sun elevation angle).

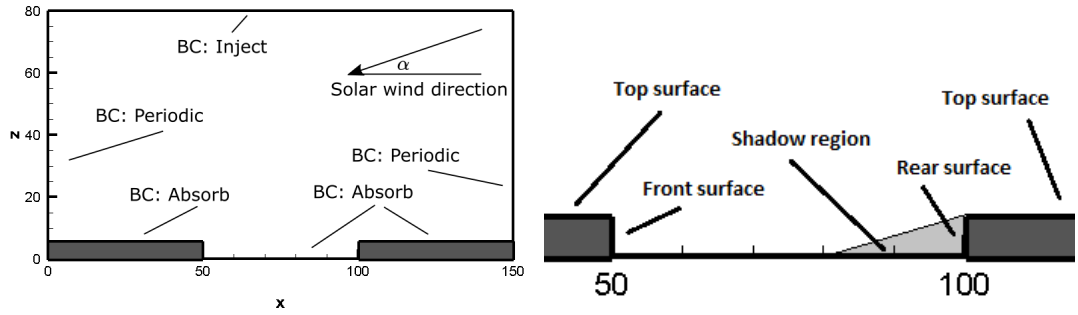

(a) Computation domain of the concave surface (b) Zoom-in view of the rectangular pit

Figure 5.9. Concave surface

5.2.3. Normalization. Same as the 1-D study of the photoelectron sheath, the parameters used in the numerical simulations were normalized by the same references listed in Table. 4.2 in Section 4.4.2.

5.2.4. Convex Lunar Surface. For convex lunar surface, a square object with a certain dimension, representing a lunar surface construction, is located on the surface in the simulations. The details of the simulations will be presented in the following sections.

Table 5.1. Solar wind parameters

	Solar wind electrons	Solar wind ions	Photoelectrons
Drifting Velocity, km/s	468	468	-
Density, cm^{-3}	8.7	8.7	64 $\sin(\alpha)$
Temperature, eV	12	10	2.2

5.2.4.1. Simulation setup. The dimension of the computation domain is 150 × 2 × 60 PIC cells (physical dimension of 207.0 × 2.76 × 82.2 m). The box-shaped object was set to be of dimension 10 × 2 × 10 PIC cells (physical dimension of 13.8 × 2.76 × 13.8 m), and located on a flat lunar surface with a shadow region, as shown in Figure 5.8(b).

Zero-Dirichlet boundary condition of $\phi = 0$ was applied at the $Z_{\max}$ boundary, which was considered as the potential reference. The other boundaries were all applied with the zero-Neumann boundary condition where $\frac{\partial \phi}{\partial n} = 0$.

Similar to the 1-D simulation, the boundary condition along y was set as "periodic", which means once the particle travels across the boundary, it will enter the computation domain from the opposite boundary with the same velocities, thus the whole domain is able to represent a relatively large area with low computation cost. The boundary condition along x was set as "reflective". The bottom surface (lunar surface and object surfaces) was set as "absorb", and the top surface of computation domain was set as "inject". The parameters of the computation domain are listed in Table 5.2. The vacuum relative permittivity ε_V was set as 1.0 (normalized by the vacuum permittivity ε_0), whereas the relative permittivity of the box-shaped object ε_B and the lunar surface ε_G were both set as 4.0 (Heiken *et al.* (1991)). In total 3,600,000 simulation particles (1,800,000 solar wind electrons and 1,800,000 solar wind ions) were pre-loaded into the computation domain as the initial condition, another 6,000 solar wind electrons and 6,000 solar wind ions, and 7,500 photoelectrons were injected

into the computation domain in each time step (dt = 0.02). The simulation ran about 50,000 steps, which was about 500 seconds in physical units. The wall clock time was about 3 hours.

Table 5.2. Computation domain parameters for 2-D structure

Space ε	Object ε	Ground ε	BC along x	BC along y	Bottom BC	Top BC
1.0	4.0	4.0	reflective	periodic	absorb	inject

5.2.4.2. Simulation results. In this 2-D simulations, we also took into account of the two distributions of the solar wind electron thermal velocity (*Maxwellian* and κ-distribution), and compare the simulation results. Figure 5.10 compares the potential contours obtained with the two distributions. Similar to what we observed in Section 4.4 for 1-D photoelectron sheath, the overall potential contours obtained with *Maxwellian* and κ-distribution are quite close for the 2-D configuration. For both distributions, the potential is nearly zero in most areas above the lunar surface, due to the charge neutrality in these areas (see Figure 5.11 and Figure 5.14). The emission of photoelectrons from the sunlit surfaces leads to a positive potential inside the box-shaped object and on the ground surface outside the shadow region, whereas the lack of sunlight leads to a negative potential on the ground surface inside the shadow region due to collection of mobile electrons.

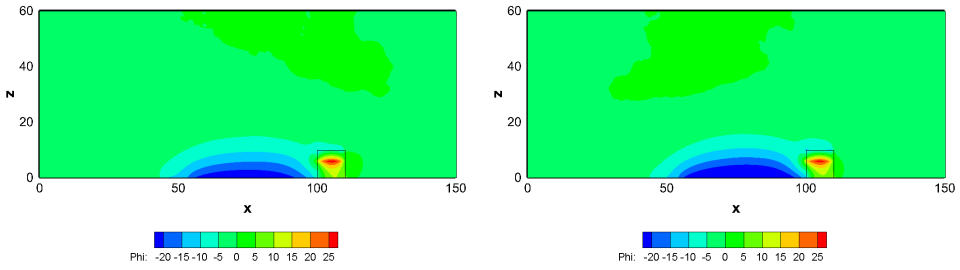

(a) *Maxwellian* (b) κ-distribution

Figure 5.10. Potential contours (normalized by 2.2 V)

The density contours of each species (i.e. solar wind electrons, solar wind ions, and photoelectrons) are shown in Figure 5.11 (*Maxwellian*), and Figure 5.14 (κ-distribution). Similar to the potential contours, the overall densities do not show too much difference between these two distributions. It can be seen that the total density is nearly neutral in most areas above the lunar surface, which leads to a near-zero potential region in these areas (see Figure 5.10).

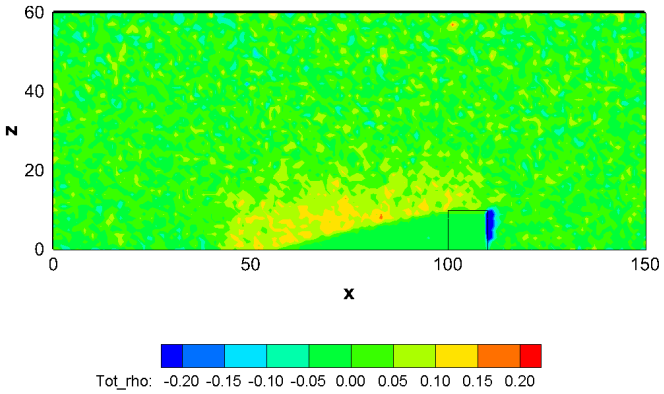

Figure 5.11. Total charge densities of convex surface (normalized by 64 cm^{-3}) obtained with *Maxwellian* velocity distribution

The solar wind electron density is lower inside and above the shadow region (Figure 5.12(a) and 5.14(a)), because the electrons within this region could easily hit and deposit charge onto the ground and object surfaces, leading to negative surface potentials. The negative surface potential then repels the nearby electrons, creating a region with lower electron density. It should be noted that the area of this low-electron region is larger in the κ-distribution case (Figure 5.14(a)) than that in the *Maxwellian* case (Figure 5.12(a)), which is also the reason of a larger wake region of potential in Figure 5.10(b). On the other hand, the solar wind ions avoid the shadow region behind the object and create a clear wake of an ion void region (Figure 5.12(b) and 5.14(b)), due to the cold temperature and larger mass of solar wind ions.

The photoelectrons are generated from the sunlight surfaces of the lunar surface and object surface. The greater local sunlight condition on the front side of the object results in a larger photoelectron emission, whereas in the shadow region behind the object, the photoelectron density is nearly zero (Figure 5.12(c) and 5.14(c)).

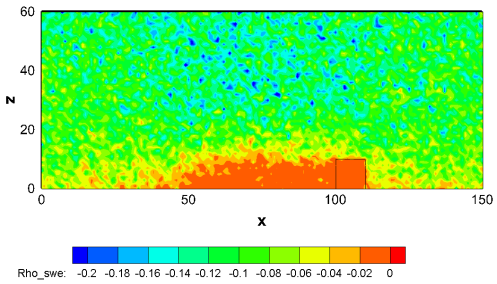

(a) Solar wind electron density

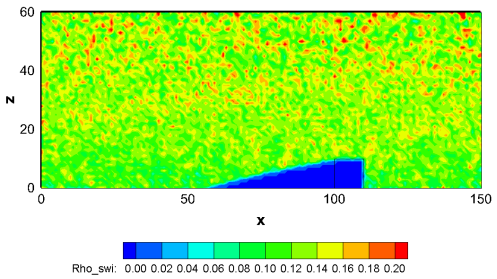

(b) Solar wind ion density

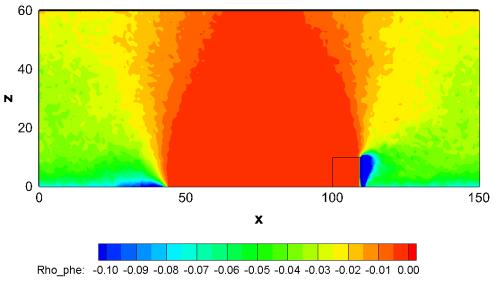

(c) Photoelectron density

Figure 5.12. Densities of solar wind and photoelectrons (normalized by 64 cm^{-3}) obtained with *Maxwellian* velocity distribution

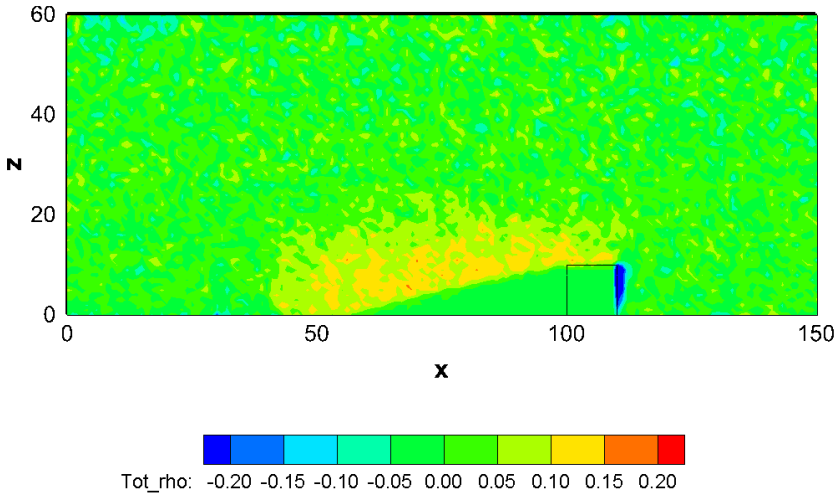

Figure 5.13. Total charge density of convex surface (normalized by 64 cm^{-3}) obtained with κ-distribution

We also analyzed the potential profiles along z at different locations along x-direction. In the following, we present the vertical potential profiles at locations of $\hat{x}$ = 20, 50, 75, 101, 111, and 130, as shown in Figure 5.15, and in Figure 5.16 we compared the potential profiles at different locations obtained with *Maxwellian* and κ- distributions. It can be seen that the potential profiles are similar at locations relatively far away from the object and the shadow region (see Figure 5.16(a) and 5.16(f)). The photoelectrons emitted from the exposed surfaces lead to a non-zero photoelectron density above the surfaces (i.e. the green and yellow region above the surface in Figure 5.12(c) and 5.14(c)). This non-zero photoelectron density will then lead to a relatively negative potential, creating the potential gradients as shown in Figure 5.16(a) and 5.16(f). On the other hand, at locations near the object, the potentials have a small gradient above the shadow region (Figure 5.16(c)) due to the charge neutrality at these regions.

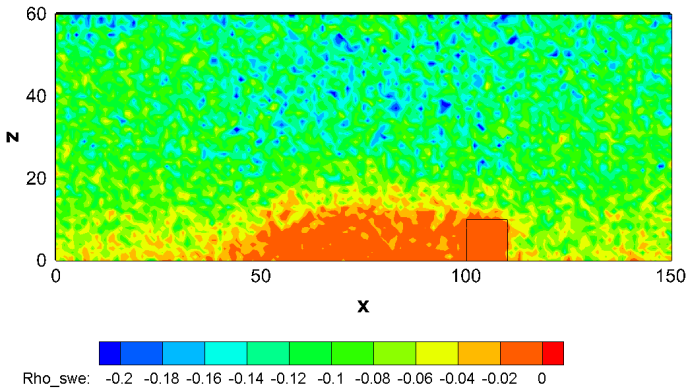

(a) Solar wind electron density

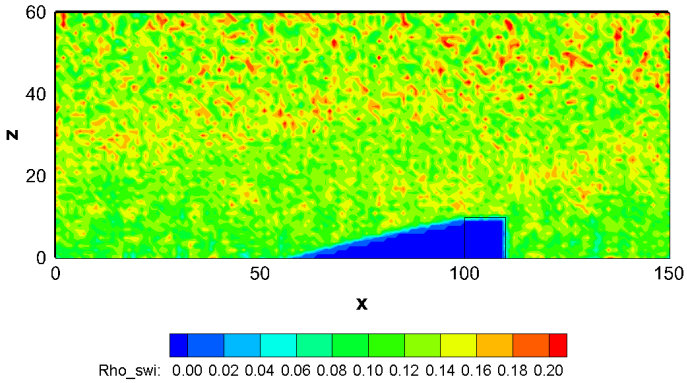

(b) Solar wind ion density

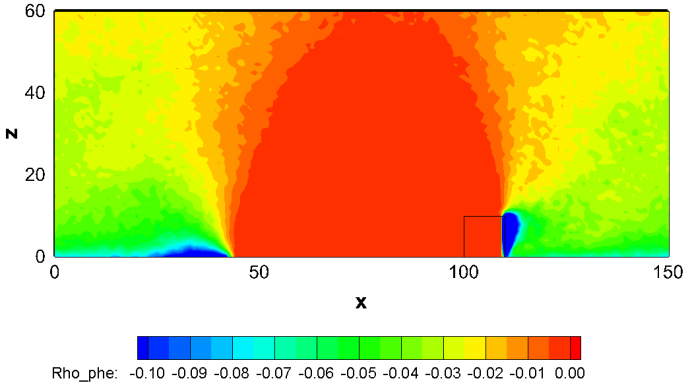

(c) Photoelectron density

Figure 5.14. Densities of solar wind and photoelectrons (normalized by 64 cm^{-3}) obtained with κ-distribution

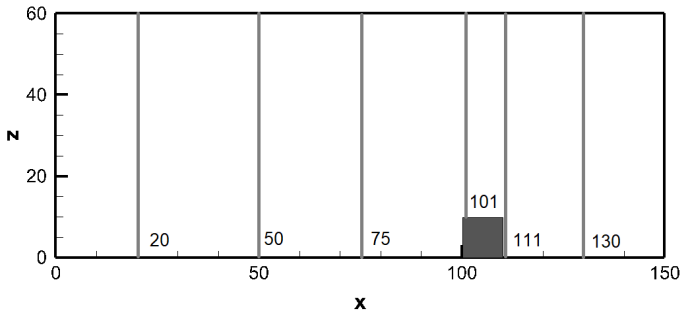

Figure 5.15. Locations to plot vertical potential profiles

The potential on the top surface of the object, as shown in the potential contour in Figure 5.10, and potential profiles in Figure 5.16(d), is slightly negative, due to the accumulation of negatively charged solar wind electrons (see Figure 5.10). However, the surface potential will become positive near the front surface of the building, due to the large local photoelectron generation caused by the larger incidence angle (i.e., 80°).

The emission of photoelectrons also results in a positive potential inside the object, which is shown in Figure 5.10. The large density of photoelectron near the front surface of the object, together with the high thermal velocity of electrons, results in a highly "irregular" potential profile compared with those in other regions (Figure 5.16(e)).

As we noticed in Section 5.1.2, the overall potential profiles of the 2-D case are quite similar for both *Maxwellian* and κ- distributions, which is consistent with the 1-D configuration. The difference between the *Maxwellian* and κ-distribution is relatively more obvious at locations of $\hat{x}$ = 20 and 130, where the negative potential is dominated by both solar wind electrons and photoelectrons. The total potential obtained with *Maxwellian* is more negative compared with that obtained with κ-distribution behind the shadow region (see Figure 5.16(a) and 5.16(b)), the possible reason is that the more negatively charged lunar surface in the shadow region behind the building caused by κ-distribution (which can be proven and seen in Figure 5.10 and 5.16(c)) repels more solar wind electrons, leading to a slightly higher electron density and more negative potential in the *Maxwellian* case. On

the other hand, the potential obtained with κ-distribution is more negative compared with *Maxwellian* inside the shadow region (see Figure 5.16(c) and 5.16(d)), and in front of the building (see Figure 5.16(e) and 5.16(f)), which is not affected by the negatively charged lunar surface in the shadow region.

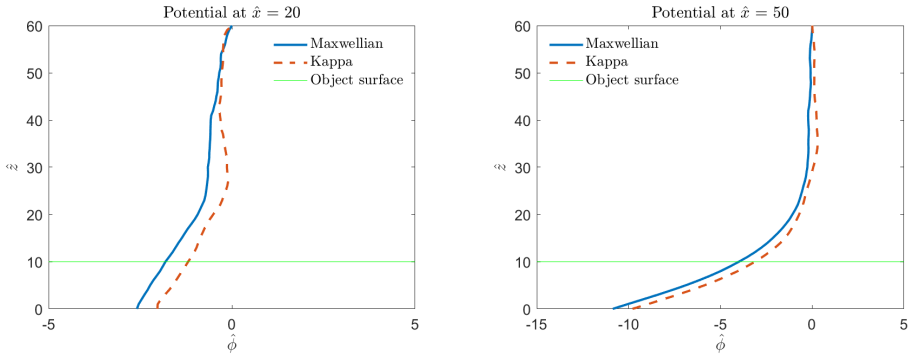

(a) Potential profile at $\hat{x}$ = 20

(b) Potential profile at $\hat{x}$ = 50

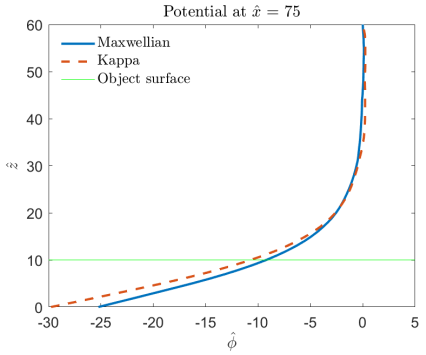

(c) Potential profile at $\hat{x}$ = 75

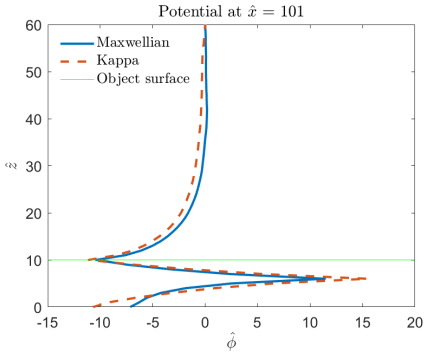

(d) Potential profile at $\hat{x}$ = 101

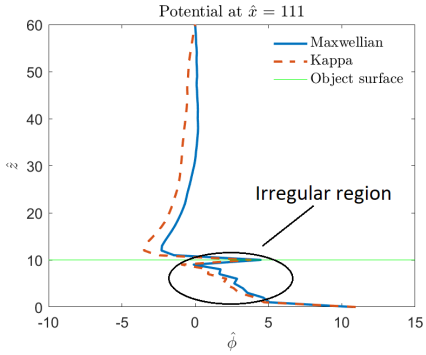

(e) Potential profile at $\hat{x}$ = 111

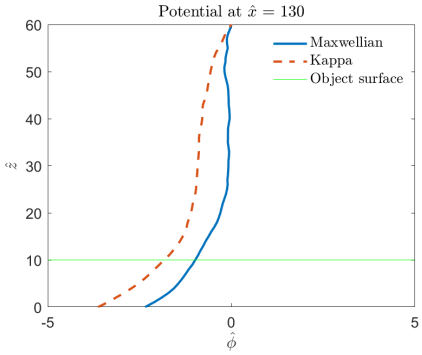

(f) Potential profile at $\hat{x}$ = 130

Figure 5.16. Comparison of potential profiles obtained with *Maxwellian* and κ- distributions

5.2.5. Concave Lunar Surface. For concave lunar surface, two rectangular objects with certain dimensions, representing two lunar surface constructions and a pit between the constructions, are located on the surface in the simulations. The details of the simulations will be presented in the following sections.

5.2.5.1. Simulation setup. The rectangular pit with a dimension of 50×2×6 PIC cells (physical dimension of 69.0×2.76×8.28 m) was located in the center of the lunar surface (with thickness of 8.22 m), and nearly half of the bottom surface inside the pit was covered by shadow, as shown in Figure 5.9(b). The dimension of the computation domain was 150×2×80 total PIC cells (physical dimension of 207.0×2.76×110.4 m). In total 3,600,000 simulation particles (1,800,000 solar wind electrons and 1,800,000 solar wind ions) were pre-loaded into the computation domain as the initial condition, another 6,000 solar wind electrons and 6,000 solar wind ions, and 6,000 photoelectrons were injected into the computation domain in each time step (dt = 0.02). The simulation ran about 50,000 steps, which was about 500 seconds in physical units. The wall clock time was about 3 hours.

5.2.5.2. Simulation results. The property profiles obtained with simulations are shown in Figures 5.17 ~ 5.20. Similar to the study of the convex surface, the potential is nearly zero above the surface in most areas, due to the neutrality of the total density.

The surface potential outside the pit is several volts negative (see Figure 5.20(a), 5.20(b), 5.20(e) and 5.20(f)), due to the emission of photoelectrons. The magnitude of potential inside the rectangular pic depends on the size of the shadow region. In this specific case, the shadow region is not large enough to cover the whole bottom surface inside the pit, hence the bottom surface potential outside the shadow region is several volts negative (see Figure 5.17), whereas the bottom surface potential inside the shadow region is more negative with a magnitude of tens of volts (see Figure 5.20(d)), caused by

the deposition of solar wind electrons on this surface, which leads to a negative charge accumulation; and the absences of exposure to sun light, which leads to the absence of photoemission in this region.

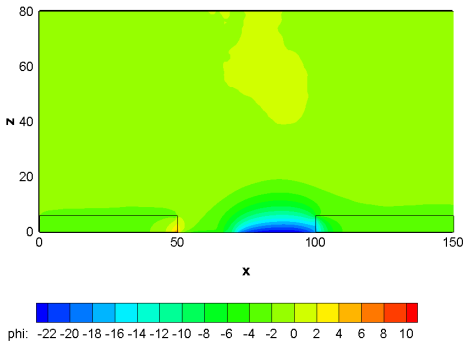

Figure 5.17. Potential of concave lunar surface (normalized by 2.2 V)

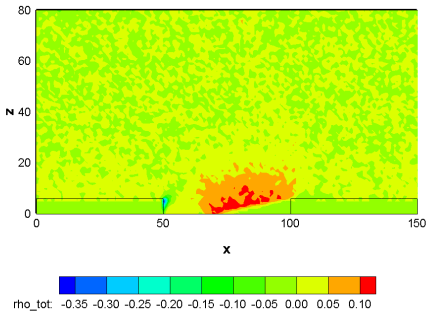

(a) Total density

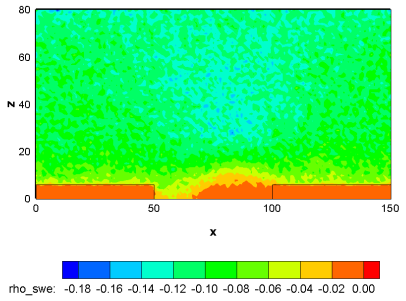

(b) Solar wind electron density

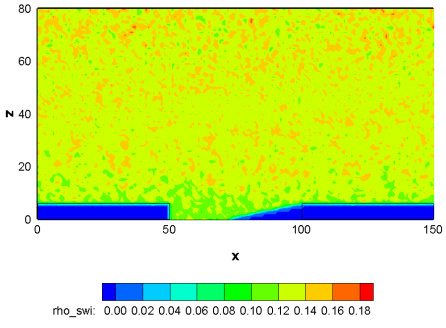

(c) Solar wind ion density

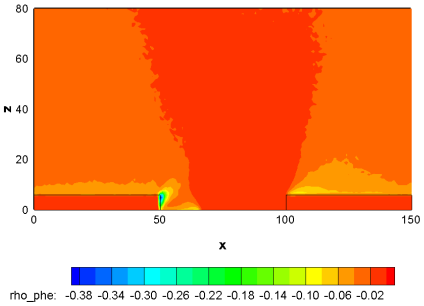

(d) Photoelectron density

Figure 5.18. Densities of solar wind and photoelectrons (normalized by 64 cm^{-3}) of concave lunar surface

The charge densities of the concave surface are also similar to those of convex surface. It can be seen in Figure 5.18(a), the total density is near neutral in most areas above the bottom surface, leading to near-zero potential region (see Figure 5.17). The density is slightly positive above the shadow region inside the pit (see Figure 5.18(a)), because the negatively charged bottom surface in the shadow region repels solar wind electrons nearby, creating a region with more ions. This is also demonstrated in solar wind electron profile as shown in Figure 5.18(b). The solar wind ions travel in a straight line (cold beam assumption), creating a triangular ion void area in the shadow region inside the pit, as shown in Figure 5.18(c). An "empty of photoelectron region" above the shadow region inside the pit was observed (see Figure 5.18(d)), which was caused by the absence of exposure to sun light inside the shadow region.

The potential profiles along z at different locations where $\hat{x}$ = 15, 35, 51, 90, 125, and 145 as shown in Figure 5.19 are presented in Figure 5.20. Similar to those of the convex surface, the potential profiles are quite similar in the areas where are relatively far away from the pit, due to the stable solar wind and photoelectron densities in these areas (see Figure 5.20(a), 5.20(b), 5.20(e) and 5.20(f)). The potential gradient near the top of the computation domain is also caused by the non-zero photoelectron density originated from the exposed surfaces.

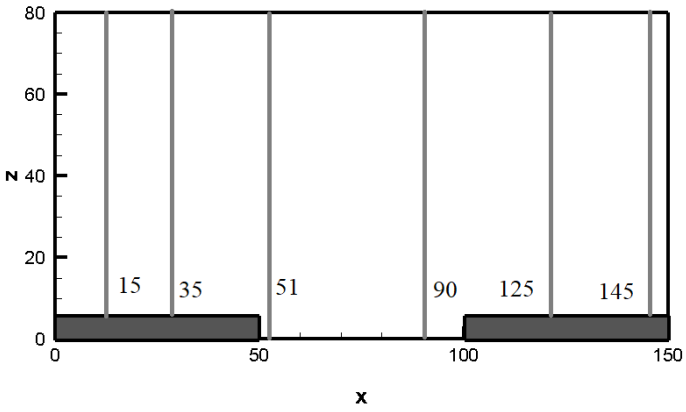

Figure 5.19. Locations to plot vertical potential profiles

The potential near the front vertical surface (see Figure 5.9) inside the pit shows a highly "irregular" potential profile (see Figure 5.20(c)), due to the large amount of photoelectrons here. There are almost no photoelectrons above and inside the shadow region (see Figure 5.18(d)), leading to a more "regular" potential profile as shown in Figure 5.20(d).

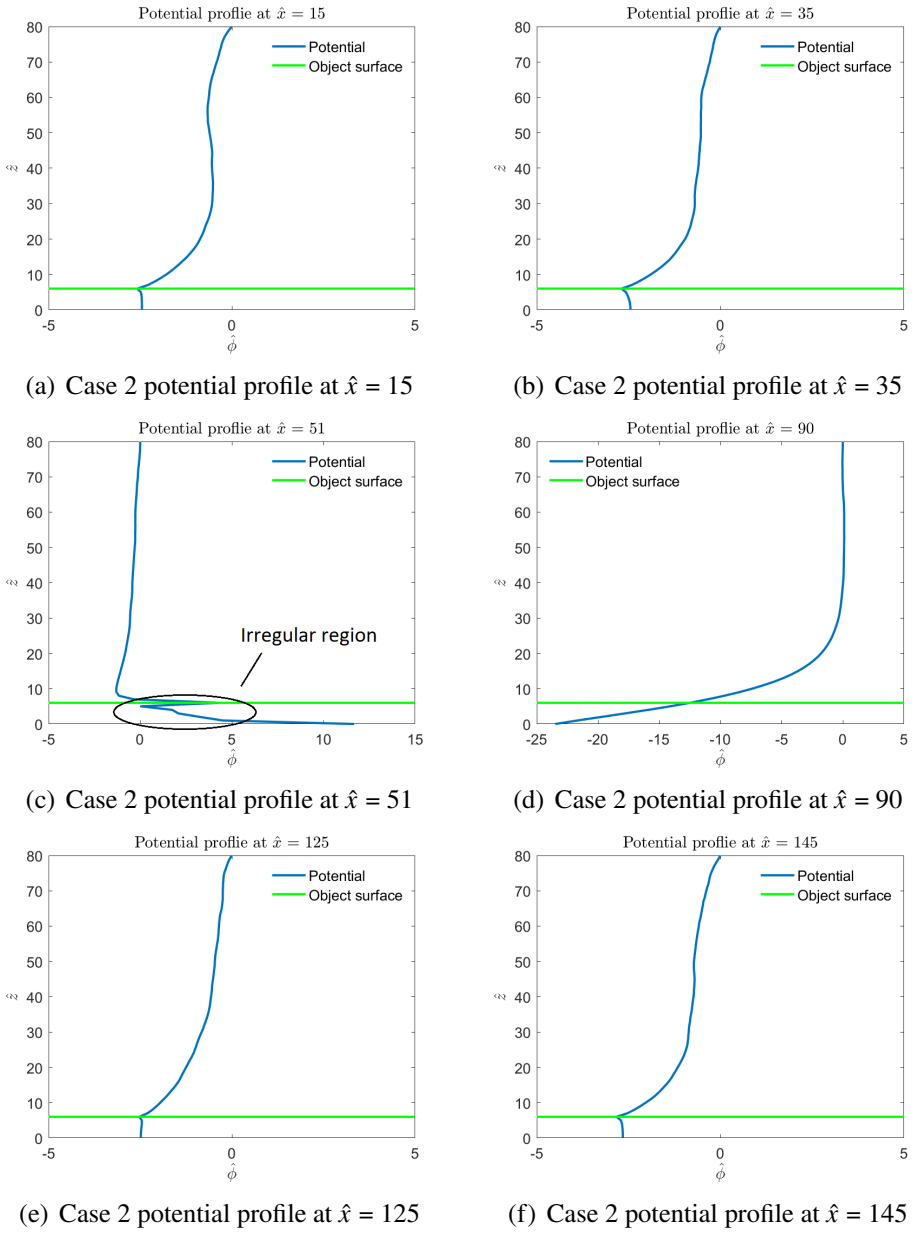

(a) Case 2 potential profile at $\hat{x}$ = 15

(b) Case 2 potential profile at $\hat{x}$ = 35

(c) Case 2 potential profile at $\hat{x}$ = 51

(d) Case 2 potential profile at $\hat{x}$ = 90

(e) Case 2 potential profile at $\hat{x}$ = 125

(f) Case 2 potential profile at $\hat{x}$ = 145

Figure 5.20. Potential profile of concave lunar surface at different locations along x

5.3. SUMMARY

We discussed the details of the simulations with considerations of the *Maxwellian* and κ-distribution solar wind electrons, and compared the difference between these two distributions under average solar wind condition in both 1-D and 2-D simulations. The results show that, even though there are slight differences, the quantities of interest such as the charge densities and potential profiles above the lunar surface are quite close between the two cases with different distribution functions. Thus the *Maxwellian* velocity distribution can be considered as accurate to describe the velocity distribution of solar wind electrons near the lunar surface under average solar wind condition.

6. SIMULATION OF DUST LEVITATION AND TRANSPORT

In this section, we will study the structure of the photoelectron sheath and its effects on charged dust transport dynamics. The FD-PIC code is utilized to simulate the plasma interaction near the lunar surface hence the local electrostatic environment, inside witch the transport dynamics of charged dust grains will be investigated. In Section 6.1, we will study the transport of the lofted charged dust grains. In Section 6.2, we will present the studies of electrostatic environment and the dust environment through uncoupled simulations. In Section 6.3, we will improve the study of Section 6.2 by taking into account of the influence of charged dust transport on local electrostatic environment through coupled simulations. A brief summary of this section will be given in Section 6.4.

6.1. DUST TRANSPORT DYNAMICS

In this section, we will introduce the dust transport dynamics, including the generation of lofted dust grains and the equations of motion.

6.1.1. Generation of Lofted Charged Dust Grains. In the simulations, the dust grains were assumed to be originated from the lunar surface with a slightly upward velocity, simulating lofted dust grains disturbed by human or mechanical activities on the lunar surface. To investigate the influence of the originated locations of the lofted dust, different dust generation locations were considered in both uncoupled and coupled simulations. The details of the uncoupled and coupled simulations will be introduced in Sections 6.3 and 6.2.

6.1.2. Governing Equations. To simplify the numerical model, all dust grains are considered as spheres with radius r_d. The dust transport dynamics follows Newton's second law as shown in Eq. (6.1).

$$\mathbf{F} = m_\mathrm{d}\frac{\mathrm{d}\mathbf{v}}{\mathrm{d}t} = Q_\mathrm{d}\vec{\mathbf{E}}(\vec{z}) - m_\mathrm{d}g \tag{6.1}$$

where m_d and Q_d are the mass and charge of the dust grain, respectively; $\mathbf{v}$ is the velocity vector; $\mathbf{E}$ is the electric field vector, which is obtained from the FD-PIC simulation; and g is the lunar gravitational acceleration. It should be noted that the last term on the right hand side of Eq. (6.1), $m_\mathrm{d}g$, only applies for z vector.

A simplified charge model, introduced by Wang *et al.* (2008), was utilized to calculate the net charge on each dust grain Q_d in numerical simulations, as shown in Eq. (6.2). In this model, the charge on each dust grain is assumed to be large enough to activate an electrostatic levitation, hence all dust grains are guaranteed to be lofted from the surface.

$$Q_\mathrm{d} = (1+\delta)Q_\mathrm{d,min} \tag{6.2}$$

where $Q_\mathrm{d,min} = (m_\mathrm{d}g)/E_s$, E_s is the electric field along z axis on the lunar surface (i.e., $E_s = E_z(z=0)$); $\delta \ll 1$ gives an initial acceleration to dust grains ($\delta = 0.05$ is assumed in this study).

According to Eqs. (6.1) and (6.2), the equations of motion of dust grains within photoelectron sheath can be obtained as Eq. (6.3).

$$\begin{aligned}
\frac{\mathrm{d}^2x}{\mathrm{d}t^2} &= \Big[(1+\delta)\frac{E_x(x,y,z)}{E_s}\Big]g \\
\frac{\mathrm{d}^2y}{\mathrm{d}t^2} &= \Big[(1+\delta)\frac{E_y(x,y,z)}{E_s}\Big]g \\
\frac{\mathrm{d}^2z}{\mathrm{d}t^2} &= \Big[(1+\delta)\frac{E_z(x,y,z)}{E_s} - 1\Big]g
\end{aligned} \tag{6.3}$$

where E_x, E_y, and E_z are the electric field along x, y, and z, respectively.

6.2. UNCOUPLED SIMULATIONS FOR UNEVEN SURFACE TERRAIN

In this section, we will introduce the studies on uneven lunar surfaces, including convex and concave surfaces, with uncoupled simulations.

6.2.1. 2-D Photoelectron Sheath Configuration. In this section, we considered two configurations of computation domain, one with a convex surface (see Figure 6.1(a)) and one with a concave surface (see Figure 6.1(b)). Then three cases with different dust generation locations (Case 1, 2, and 3 in Figure 6.1) will be simulated for each configuration.

As shown in Figure 6.1, for convex surface, dust grains in Case 1 were generated from the lunar surface in front of the surface structure. In Case 2, dust grains were originated inside the shadow region behind the surface structure. Whereas in Case 3, dust grains were generated outside the shadow region behind the surface structure. For concave surface, in Case 1 the dust grains were generated on the top of the first surface structure, in Case 2 the dust were originated from the bottom surface between two structures. It should be noted here that in Case 2, the dust grains were generated along the entire bottom surface ($\hat{x} = 50 - 100$), while the shadow region only covers $\sim 3/4$ of the bottom surface, as shown in Figure 6.1(b). In Case 3 the dust grains were generated on the top of the second structure.

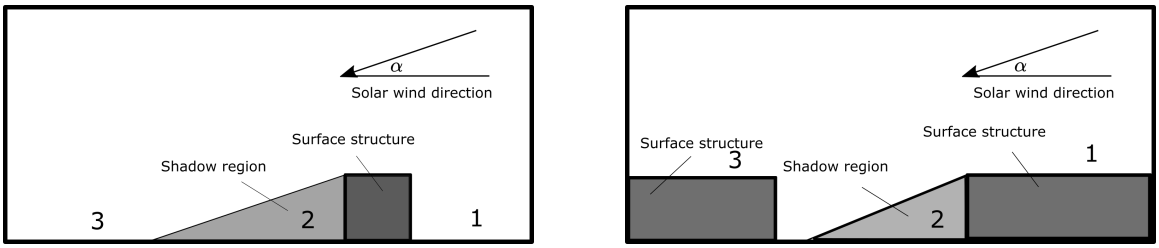

(a) Convex surface (b) Concave surface

Figure 6.1. Uneven lunar surface

The field information of the electrostatic environment were obtained with the simulations introduced in Section 5.2.

6.2.2. 2-D Plasma Environment. The details of the 2-D photoelectron sheath structure has been studied and introduced in Section 5.2. For both convex and concave lunar surface, a nearly neutral potential profile can be observed in most areas above the lunar surface, due to the density neutrality in these areas. For convex surface, the emission

of photoelectrons from the surface leads to a positive potential on the lunar surface outside the shadow region, whereas the lack of sun light leads to a negative potential on the lunar surface inside the shadow region. For concave surface, The magnitude of potential inside the pit depends on the size of the shadow region. In this specific case, the shadow region only covers a partial lunar surface inside the pit, hence the surface potential outside the shadow region is several volts negative, whereas the potential inside the shadow region is more negative with a magnitude of tens of volts, caused by the deposition of solar wind electrons and the absences of exposure to sun light.

6.2.3. 2-D Dust Environment. In these simulations, The computation domain was $150 \times 2 \times 80$ total PIC cells (physical dimension of $207.0 \times 2.76 \times 110.4$ m) for both convex and concave surfaces. 1000 dust grains were injected into the computation domain in each time step (dt = 0.1 s). The simulations ran about 5,000 steps, which was about 500 seconds in physical units. The wall clock time was about 20 minutes. The simulation results are given in the following sections.

6.2.3.1. Convex surface case 1. The dust density shown in Figure 6.2 was obtained with the charge model (Eq. (6.2)). Here we used two dust radii, $r_d = 1.0 \times 10^{-6}$ m and $r_d = 10.0 \times 10^{-6}$ m, to investigate the influence of dust radius on the dust trajectory. As it can be seen, both two radii show similar trajectories, indicating that the dust trajectories obtained by the charge model are not affected by dust radius. According to Eq. (6.2), the electric charge of each dust grain (therefore the electrostatic force) is proportional to the gravitational force acting on the grain, thus the motion of lofted dust grains are only controlled by the ambient electric field (generated according to local Sun elevation angle) within the photoelectron sheath. In Case 1, Some dust grains can be lofted and sustained at as high as ~83 m.

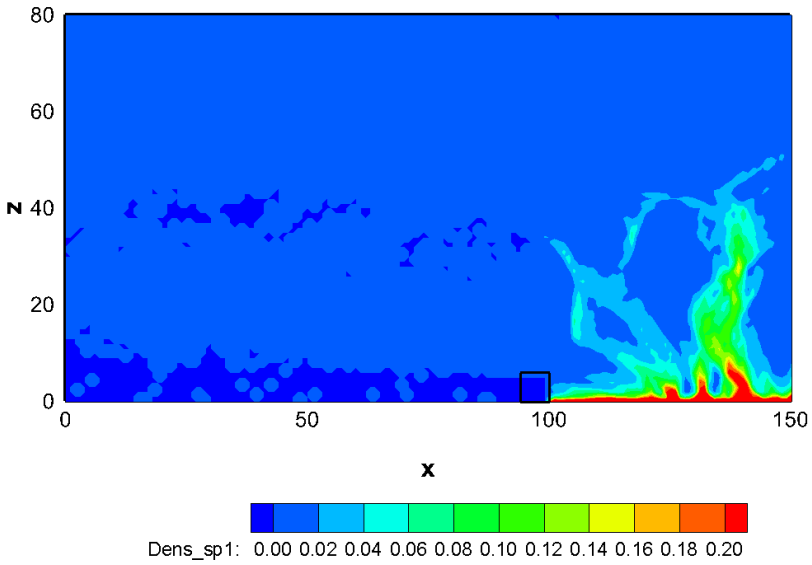

(a) $r_d = 1.0 \times 10^{-6}$ m

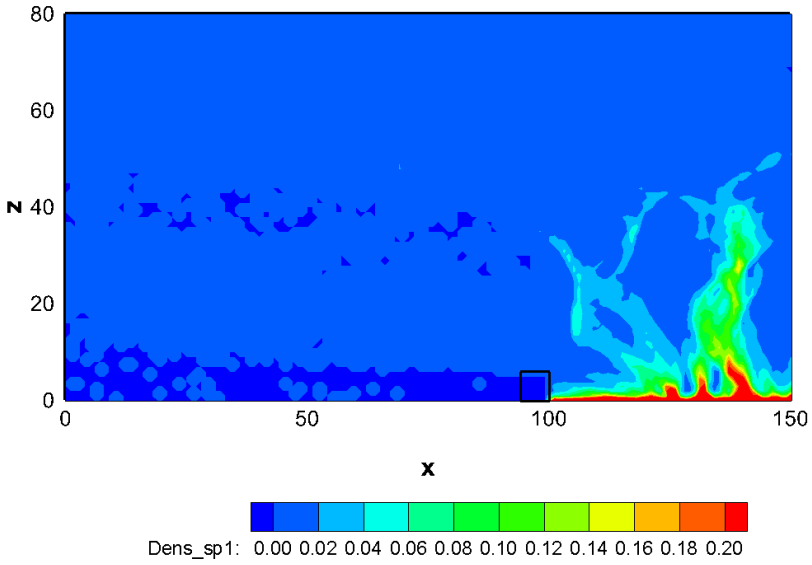

(b) $r_d = 10.0 \times 10^{-6}$ m

Figure 6.2. Dust density of convex surface Case 1

6.2.3.2. Convex surface case 2. It can be seen in Figure 6.3 that most of the dust grains in Case 2 are confined inside the shadow region. The dust density inside the shadow region is much greater than that outside the shadow region.

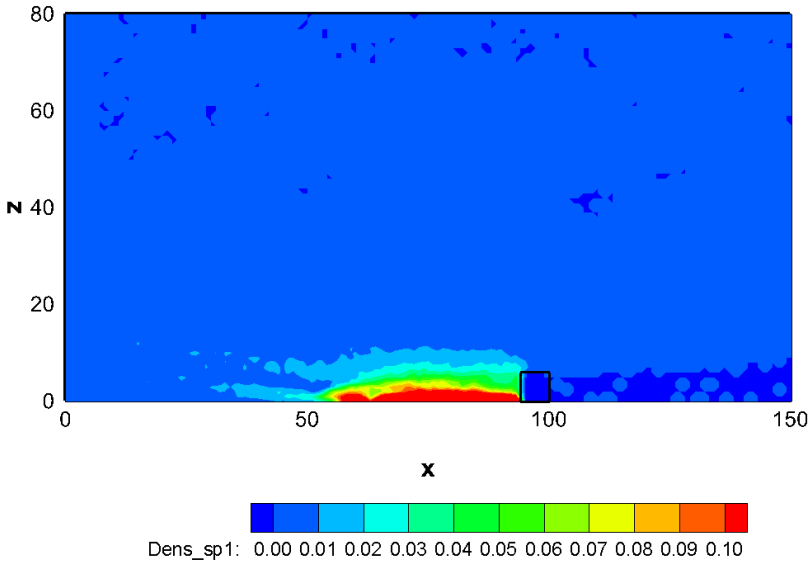

(a) $r_d = 1.0 \times 10^{-6}$ m

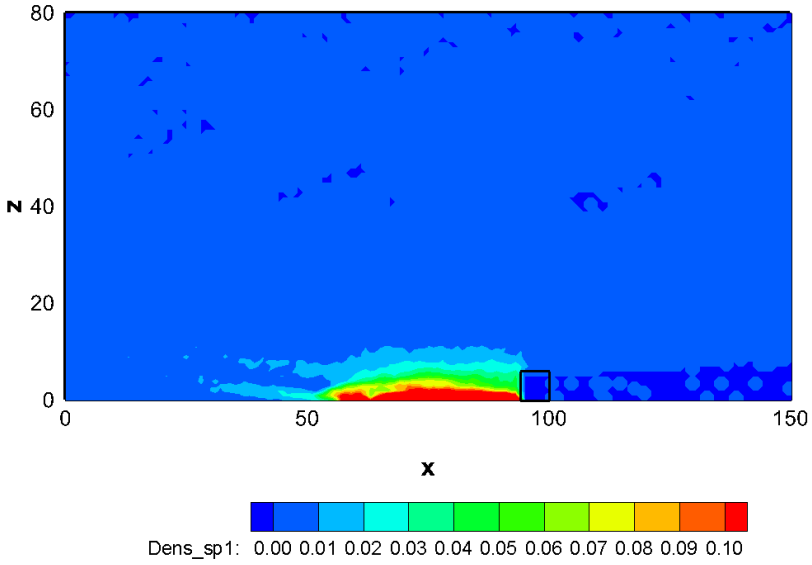

(b) $r_d = 10.0 \times 10^{-6}$ m

Figure 6.3. Dust density of convex surface Case 2

6.2.3.3. Convex surface case 3. In Case 3, the dust grains are distributed into a greater area compared with Case 1 and 2. It can be seen from Figure 6.4 that the dust grains generated near the shadow region behind the surface structure show a tendency to travel over the shadow region, and move to the other side of the surface structure.

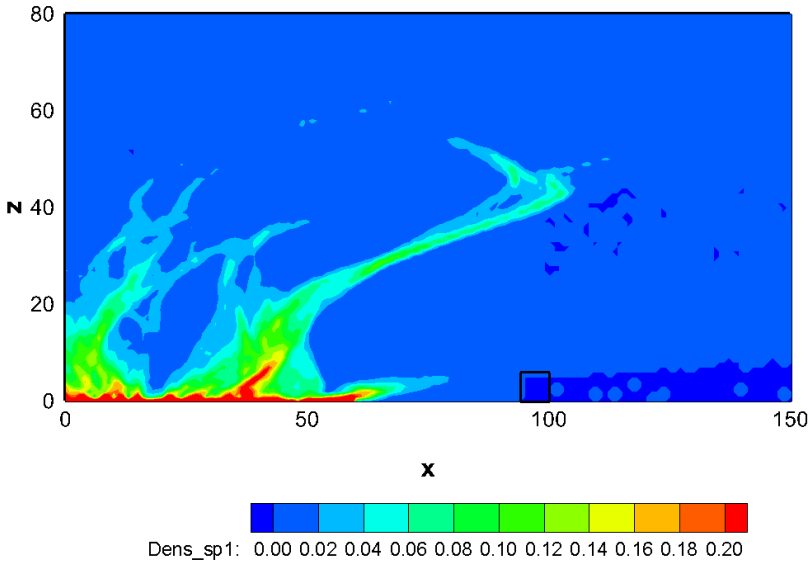

(a) $r_d = 1.0 \times 10^{-6}$ m

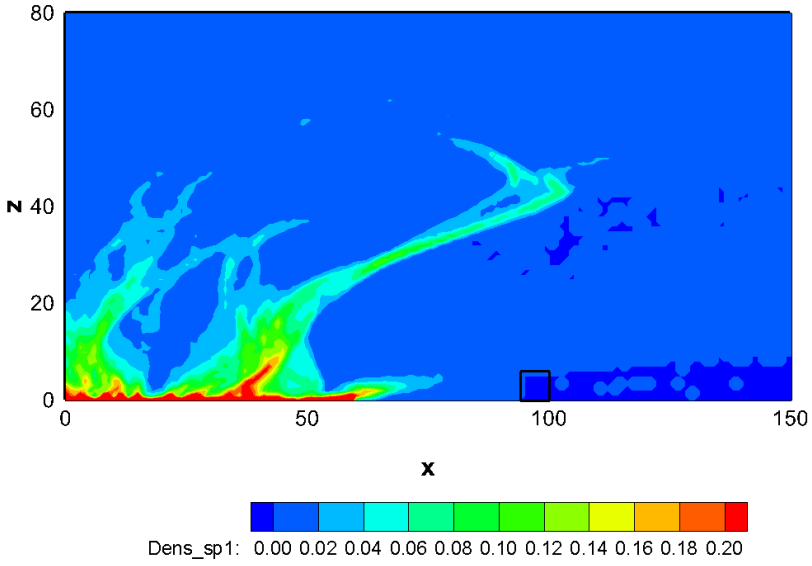

(b) $r_d = 10.0 \times 10^{-6}$ m

Figure 6.4. Dust density of convex surface Case 3

6.2.3.4. Concave surface case 1. Similar to the condition in convex lunar surface, dust generated in Case 1 tends to move upward under the effect of electrostatic force acting on the grains. The dust that generated in front of the pit shows tendency to travel to the left under the effect of solar wind (which travels from right to left), as shown in Figure 6.5.

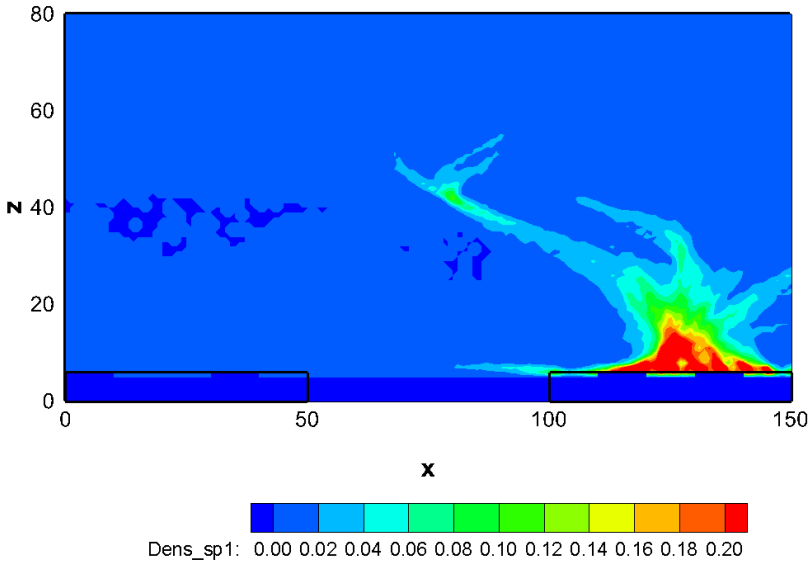

(a) Dust density, $r_d = 1.0 \times 10^{-6}$ m

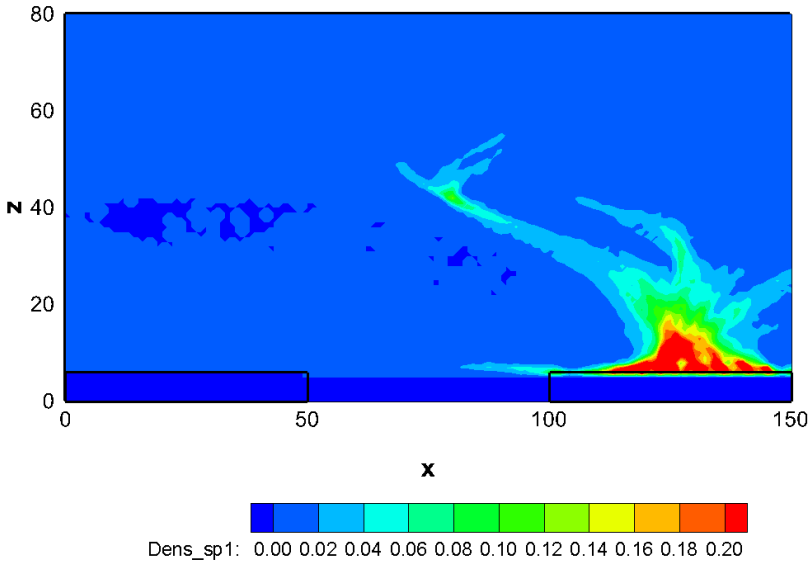

(b) Dust density, $r_d = 10.0 \times 10^{-6}$ m

Figure 6.5. Dust density of concave surface Case 1

6.2.3.5. Concave surface case 2. In Case 2, most of the dust generated inside the pit between the two structures are confined near the bottom of the pit. The dust grains originated outside the shadow region show a tendency to travel higher compared with the dust inside the shadow region, as shown in Figure 6.6.

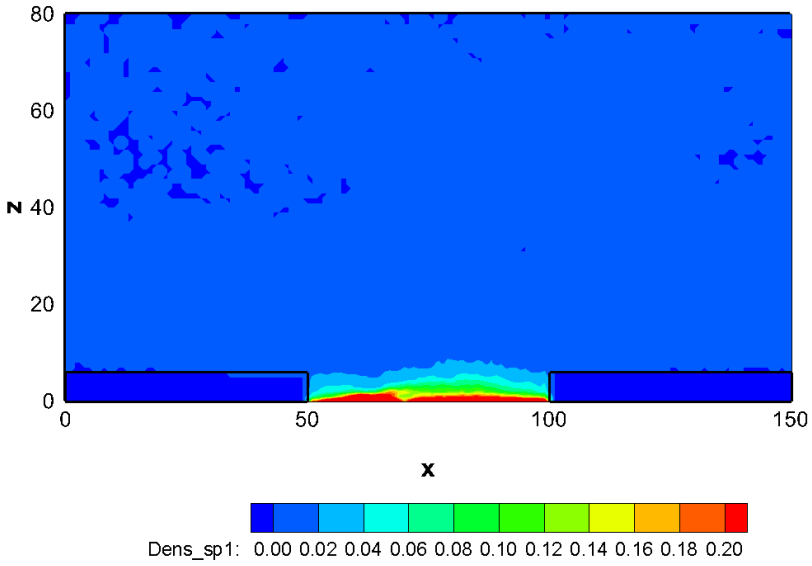

(a) Dust density, $r_d = 1.0 \times 10^{-6}$ m

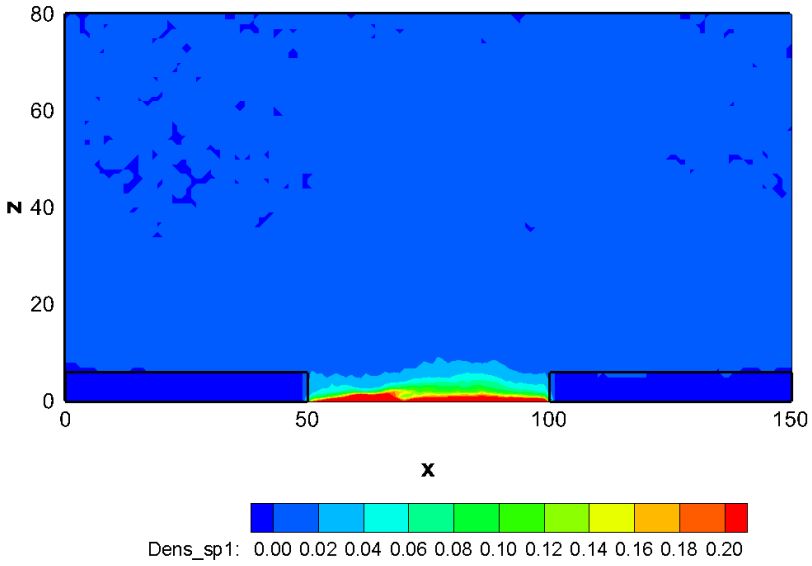

(b) Dust density, $r_d = 10.0 \times 10^{-6}$ m

Figure 6.6. Dust density of concave surface Case 2

6.2.3.6. Concave surface case 3. Again, the charged dust grains show a tendency to move upward under the effect electrostatic force in Case 3. Some of the dust grains near the pit tends to travel over the shadow region, and reach to the structure on the other side of the shadow region, as shown in Figure 6.7.

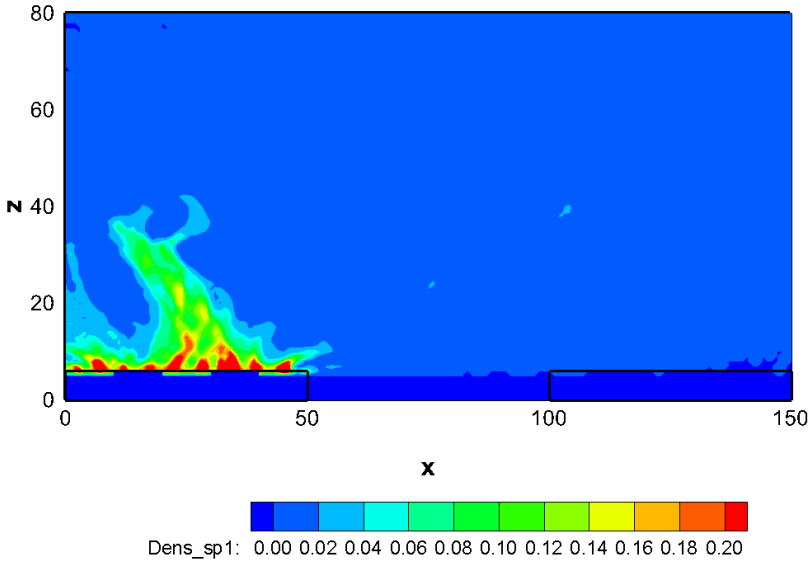

(a) Dust density, $r_d = 1.0 \times 10^{-6}$ m

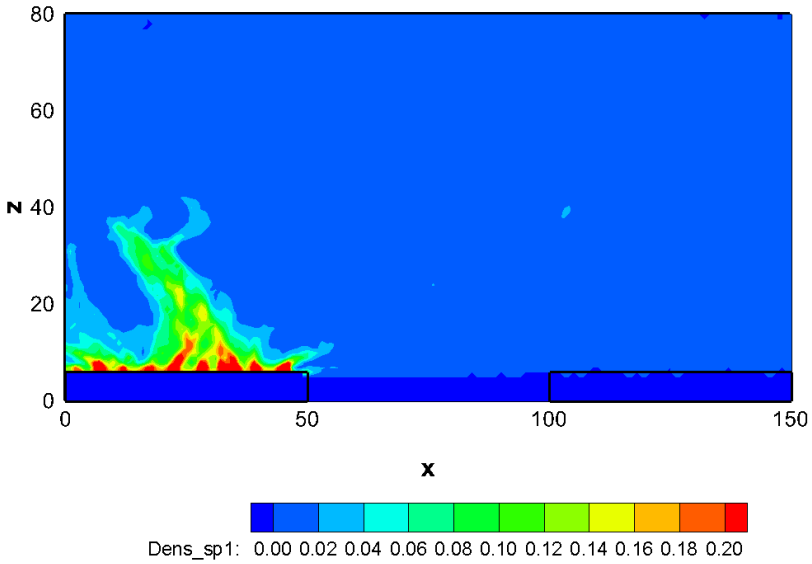

(b) Dust density, $r_d = 10.0 \times 10^{-6}$ m

Figure 6.7. Dust density of concave surface Case 3

6.2.4. 3-D Photoelectron Sheath Configuration. We have presented the studies of 1-D and 2-D configurations for even and uneven lunar surface terrains above. In this section, we will study the 3-D configuration of the photoelectron sheath above the uneven lunar surface and its effects on dust transport dynamics.

6.2.4.1. Problem description and simulation setup. The computation domain is presented in Figure 6.8. A cubic obstacle was located on the lunar surface at the center of the computation domain, representing a lunar surface construction. The solar wind enters the computation domain from the top boundary with a certain Sun elevation angle, α. The charged particles will deposit on the bottom surface of the computation domain (which is considered as the lunar surface) and the obstacle surfaces, creating a surface potential. The surface potential, together with the density above the lunar surface, controls the electrostatic environment inside the photoelectron sheath. The FD-PIC code will be used to run simulations to obtain the quantities of interest (electric potential, electric field, charge density, etc.) in the computation domain. In total four cases with different dust generation locations (Case 1, 2, 3, and 4 in Figure 6.9, which is the top view of the computation domain) will be simulated.

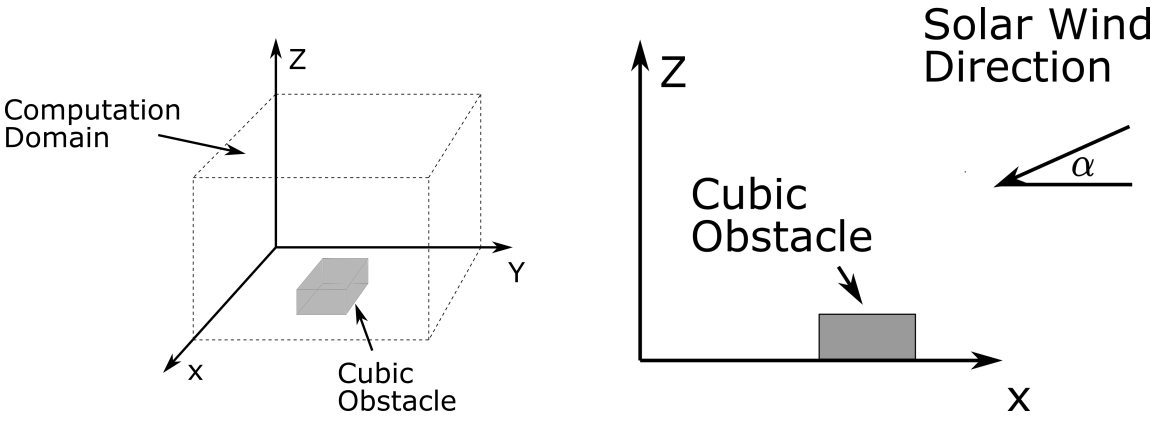

(a) Computation domain (b) Solar wind direction

Figure 6.8. 3-D computation domain

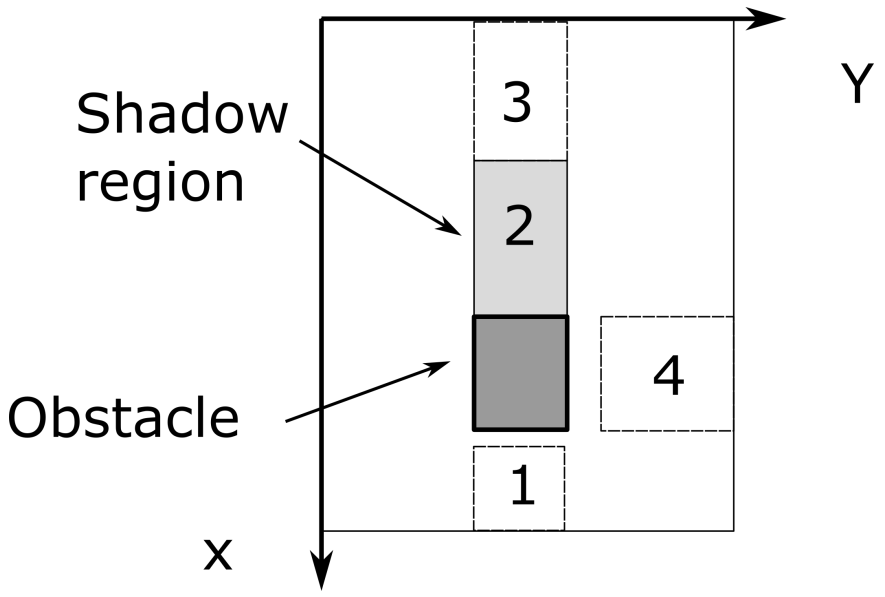

Figure 6.9. Dust generation locations in different cases

As shown in Figure 6.9, In Case 1, dust was originated in front of the obstacle. Whereas in Case 2, dust was disturbed in the shadow region behind the obstacle. In Case 3, dust was levitated behind the shadow region of the obstacle, And in Case 4, dust was generated alongside the obstacle.

6.2.4.2. Computation domain. The configuration of the computation domain is shown in Figure 6.10(a). The dimension of the computation domain is 70×25×50 total PIC cells (physical dimension of 96.6×34.5×69.0 m). The cubic obstacle with a dimension of 5×5×5 PIC cells (physical dimension of 6.9×6.9×6.9 m) is located on the lunar surface with a shadow region behind.

6.2.4.3. Particle boundary conditions. The boundary condition for surrounding boundaries was set as "periodic", meaning that once a particle crosses one of these boundaries. it will enter the computation domain from the opposite boundary with the same properties, therefore the computation domain represents a relatively larger domain with low computation cost in simulations. The bottom surface was set as "absorb", meaning the

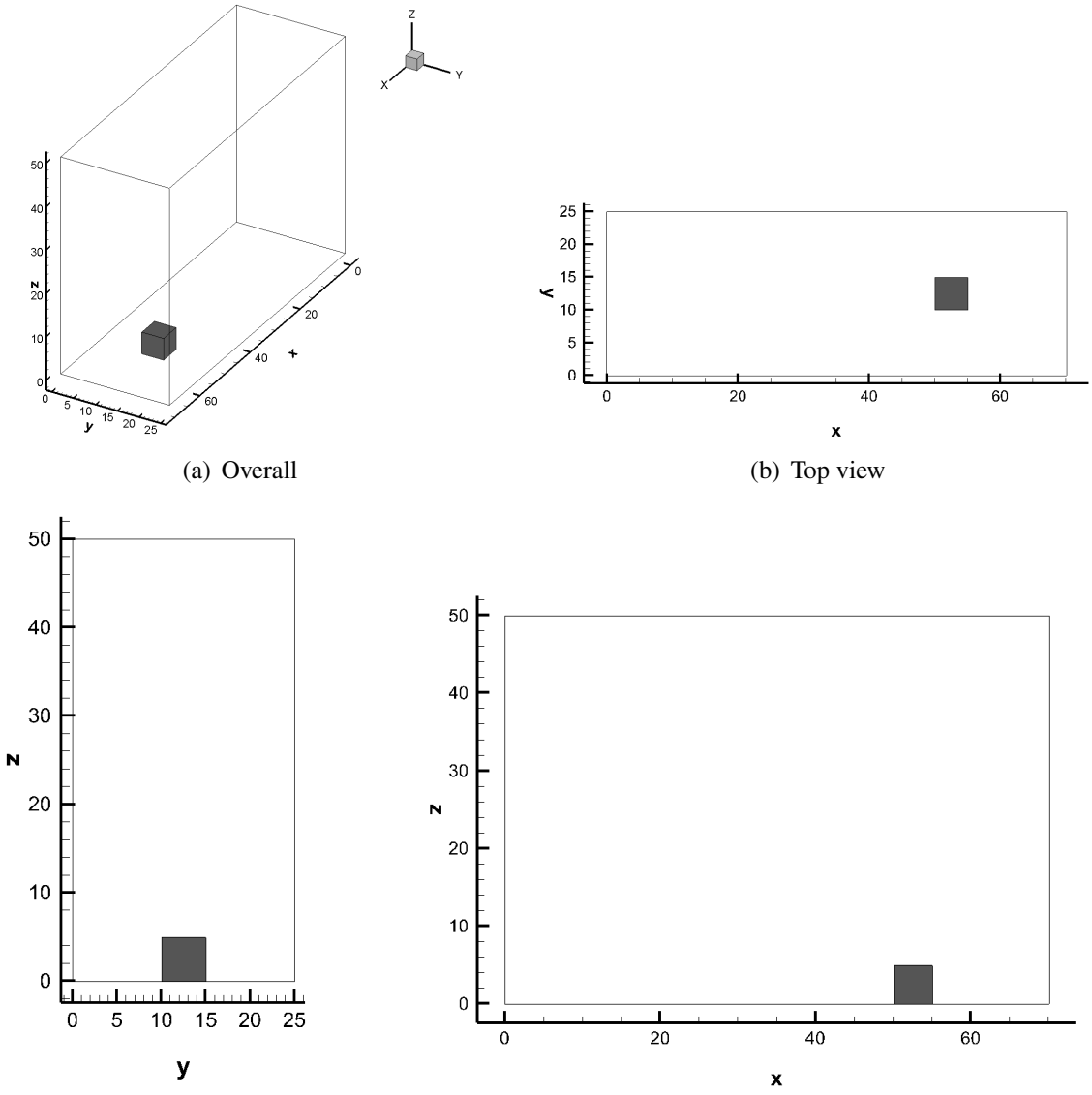

(a) Overall

(b) Top view

(c) Front view

(d) Side view

Figure 6.10. Computation domain in simulation

particle will deposit and the charge will be accumulated on the surface once it hits the surface. The top surface was set as “inject”, from where the solar wind enters the computation domain. The boundary conditions of the computation domain are listed in Table 6.1.

Table 6.1. Boundary conditions of the computation domain

Surrounding BC	Bottom BC	Top BC
periodic	absorb	inject

6.2.4.4. Field boundary conditions. The zero-Dirichlet boundary condition with $\phi = 0$ was applied for the $Z_{\max}$ boundary, where was considered as infinity in the simulations. All other boundaries were applied with the zero-Neumann boundary condition where $\frac{\partial \phi}{\partial n} = 0$.

6.2.4.5. Modeling plasma environment. In this section, we will focus on the plasma and dust environment near the lunar terminator region, therefore a 10 ° SEA was applied in the numerical simulations. During the simulations, the solar wind electrons, solar wind ions, and photoelectrons were considered as the plasma species within the photoelectron sheath. The solar wind was assumed traveling to the lunar surface with a 10° Sun elevation angle and 468 km/s velocity. The solar wind electrons were considered as thermal with a temperature of 12 eV, whereas the temperature of solar wind ions was 10 eV. The solar wind number density was 8.7 cm^{-3}. The temperature of photoelectron was 2.2 eV, and the density of photoelectron on the lunar surface was controlled by the SEA. The parameters of solar wind and photoelectrons are listed in Table 6.2 (Lund *et al.* (2020); Wang *et al.* (2008); Zhao *et al.* (2020b)).

Table 6.2. Solar wind and photoelectron parameters

	Solar wind electrons	Solar wind ions	Photoelectrons
Drifting Velocity, km/s	468	468	-
Density, cm^{-3}	8.7	8.7	64 $\sin(\alpha)$
Temperature, eV	12	10	2.2
Sun Elevation Angle, °	10	10	10

The solar wind were traveling into the computation domain through the X-Y plane. along -z-direction. At the beginning of the simulation, ~1,800,000 solar wind electrons and ~1,800,000 ions were pre-loaded inside the computation domain. Another ~10,000 solar wind electrons, ~10,000 solar wind ions, and ~10,000 photoelectrons were injected into the computation domain in each iteration. The simulation ran 50,000 steps for each case (dt = 0.005, mesh size is 1.0), which was ~250 seconds in reality, and ~50 hours in wall clock time. To increase the efficiency and reduce the complexity of numerical computation, All parameters were normalized by the references introduced in Section 4.4.2.

6.2.5. 3-D Plasma Environment. The distributions of potential and total density within the photoelectron sheath are shown in Figures 6.11 and 6.12. The density of each species is shown in Figures 6.13 6.15. As it can be seen in Figure 6.11(a), a nearly neutral potential profile can be observed in most areas above the lunar surface, due to the density neutrality in these areas (see Figure 6.12(a)). The emission of photoelectrons caused by the exposure to sun light, leads to a positive potential on the front and top surfaces of the obstacle and the lunar surface outside the shadow region. Whereas the lack of sun light leads to a negative potential inside the shadow region.

It is reasonable that the potential is much higher near the front surface of the obstacle, due to the larger photoelectron density (caused by the relatively greater incidence angle on the front surface) and the corresponding larger amount of positive charges accumulated on the front surface.

6.2.6. 3-D Dust Environment. In this simulation, all dust grains were considered as spheres with same radius (1.0×10^{-6} m). In total 2,000 dust grains were injected into the computation domain (70×25×50 PIC cells, about 96.6×34.5×69.0 m) in each time step (0.1 s). The motion of the dust were controlled by the governing equations introduced in Section 6.1.2. Since the physical initial dust density that originated from the lunar surface is random and can be affected by a number of conditions (concentration of dust grains on the lunar surface, strength of human activities, etc.) The initial non-dimensional dust density

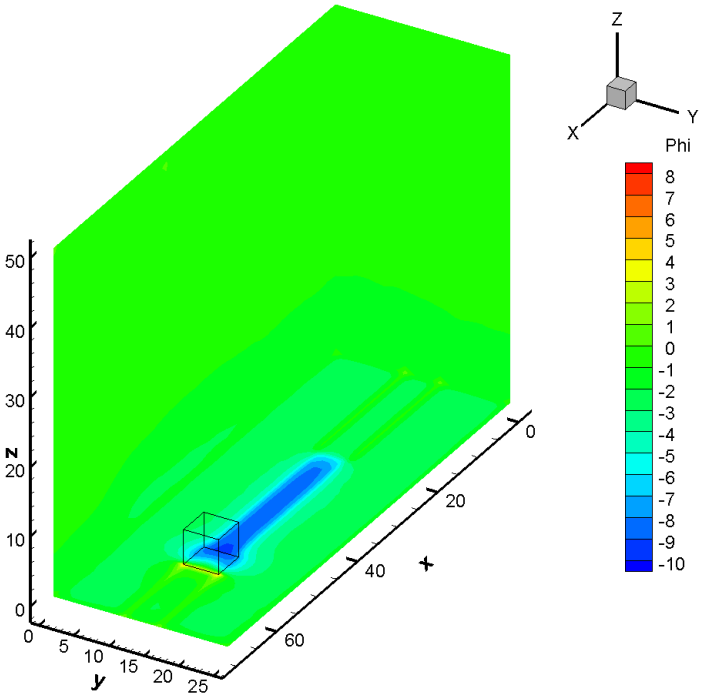

(a) Potential

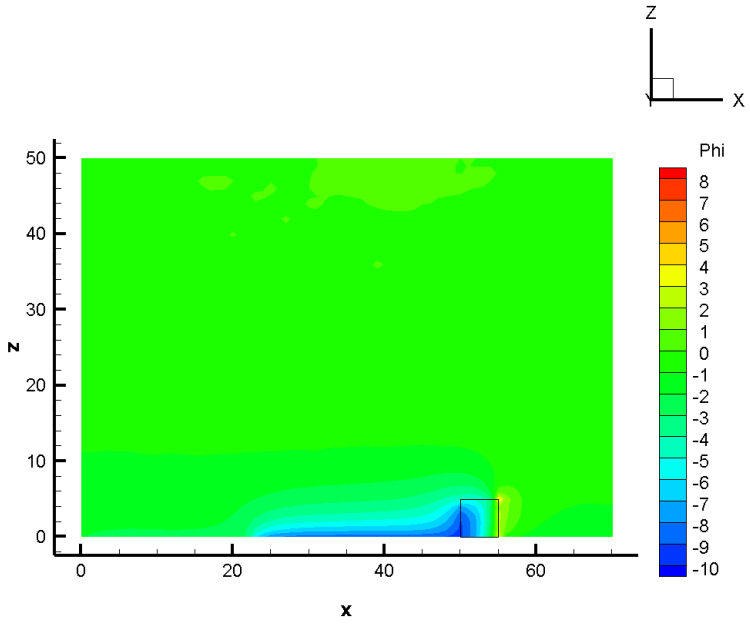

(b) Potential side view

Figure 6.11. Electric potential, normalized by 2.2 V

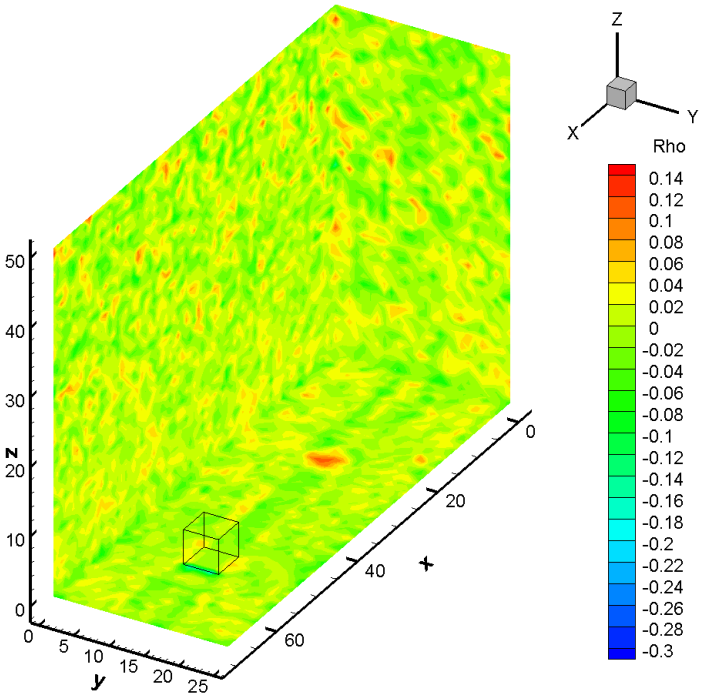

(a) Total density

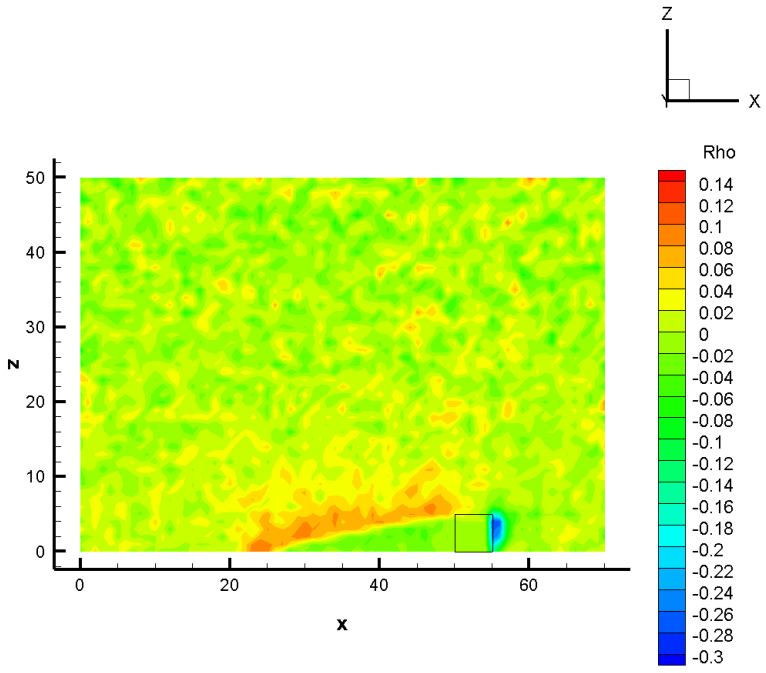

(b) Total density side view

Figure 6.12. Total density, normalized by 64 cm^{-3}

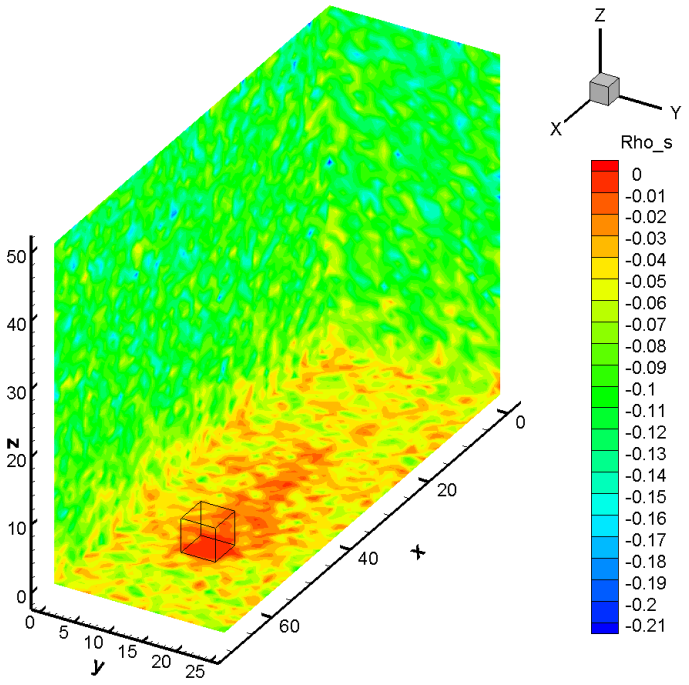

(a) Solar wind electron density

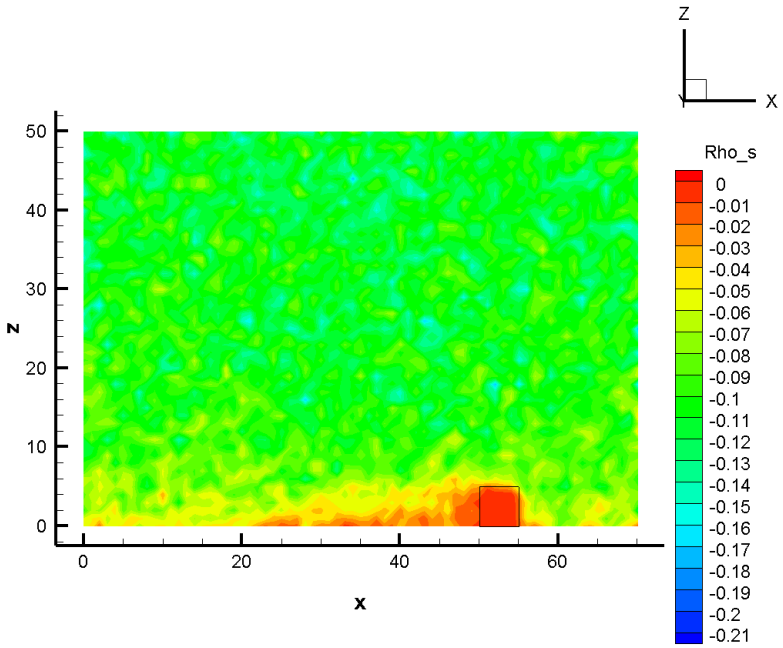

(b) Solar wind electron density side view

Figure 6.13. Density of solar wind electrons, normalized by 64 cm^{-3}

was set as 1.0 for each case in the simulation to present the ratios of dust density at different locations compared with the initial disturbed and levitated dust grains. The concentration of dust grains in the computation domain that generated at different locations are presented below.

6.2.6.1. Case 1. The concentration of dust grains that originated in front of the obstacle (Case 1) is shown in Figure 6.16. With a radius of 1.0×10^{-6} m and initial upward velocity of 0.1 m/s, most of the dust will be levitated and concentrated within ~2 m from the lunar surface under 10° Sun elevation angle in the average solar wind condition. However, a slight amount of dust can be lofted much higher (up to ~60 m) and distributed inside the entire computation domain, due to the greater accumulated electric charge and the corresponding greater electrostatic force acting on the dust (see Figure 6.16(b)).

6.2.6.2. Case 2. Slightly different from Case 1, The dust lofted in Case 2 does not distribute into a large area. The dust grains generated inside the shadow region are concentrated within ~2 m height from the lunar surface. The levitation height is slightly higher for the dust that closer to the obstacle. A slight amount of dust can be lofted to ~13 m above the surface behind the obstacle. It can be seen that some dust grains are able to reach as high as ~55 m right above the top of the obstacle.

6.2.6.3. Case 3. Similar to Case 1, the levitation height of the dust grains originated behind the shadow region of the obstacle is ~2 m from the lunar surface. A slight amount of dust can be distributed into a larger area around the origination of the dust. It can be seen in Figure 6.18(b) that the charged dust in Case 3 can be distributed into the shadow region behind the obstacle, whereas these dust will not distributed within a certain height (~41 m) above and in front of the obstacle.

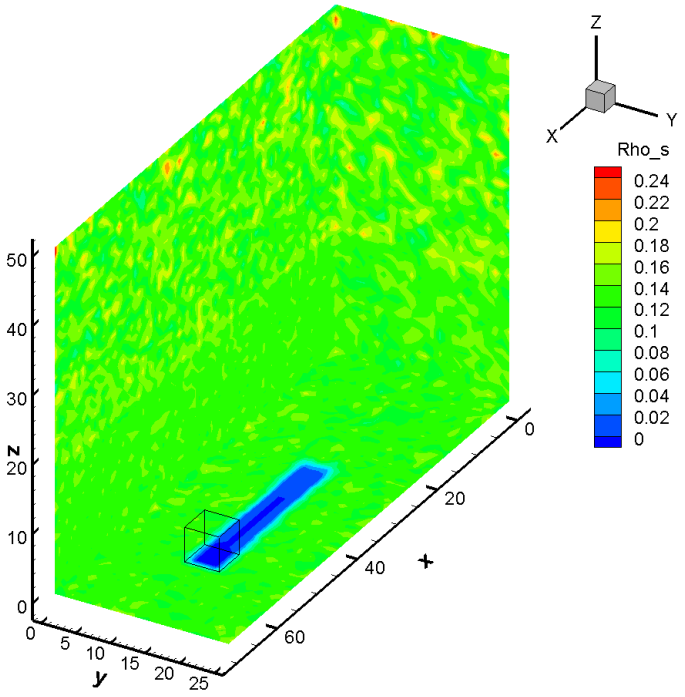

(a) Solar wind ion density

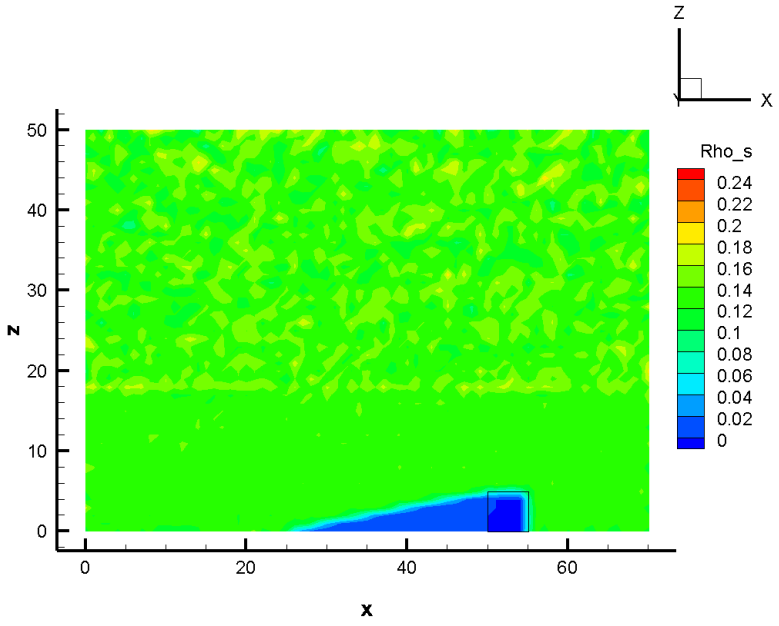

(b) Solar wind ion density side view

Figure 6.14. Density of solar wind ions, normalized by 64 cm^{-3}

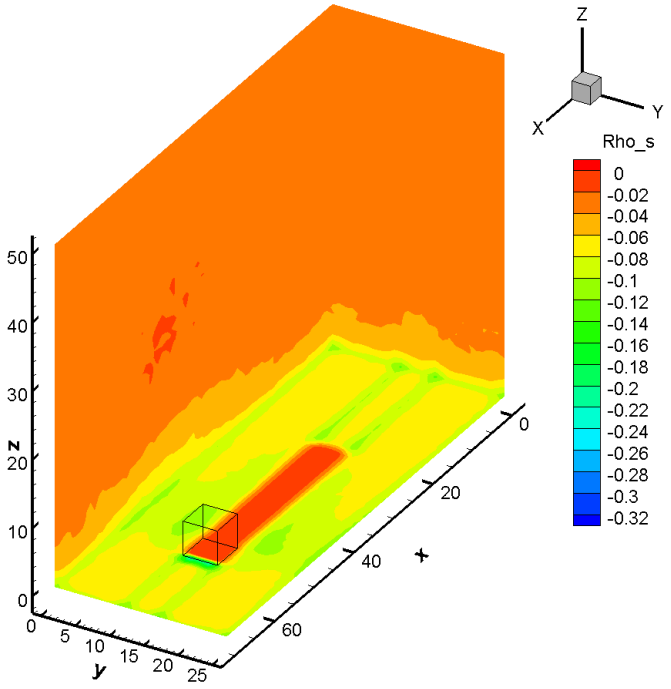

(a) Photoelectron density

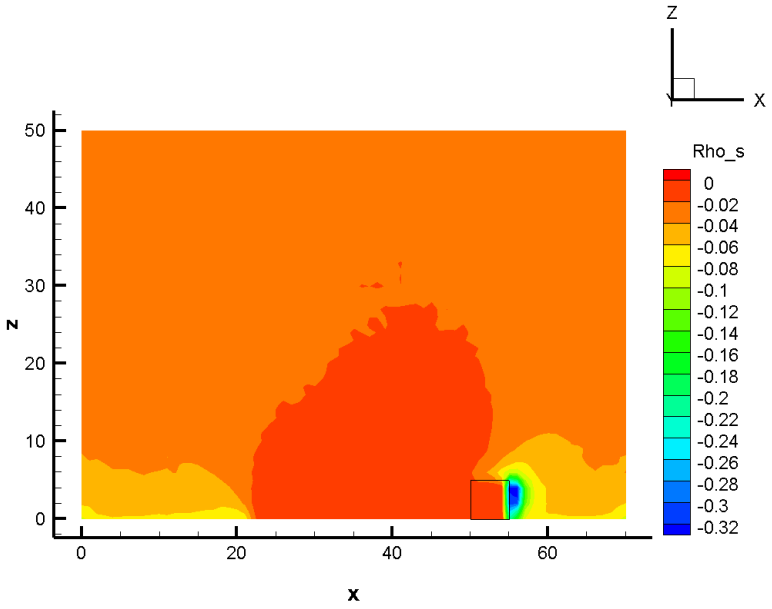

(b) Photoelectron density side view

Figure 6.15. Density of photoelectrons, normalized by 64 cm^{-3}

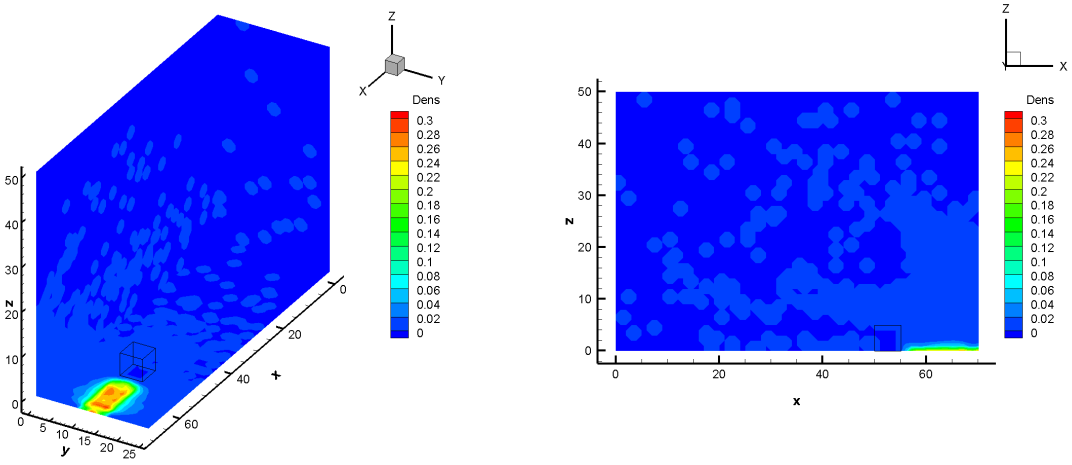

(a) Dust density (b) Dust density side view

Figure 6.16. Dust density of Case 1

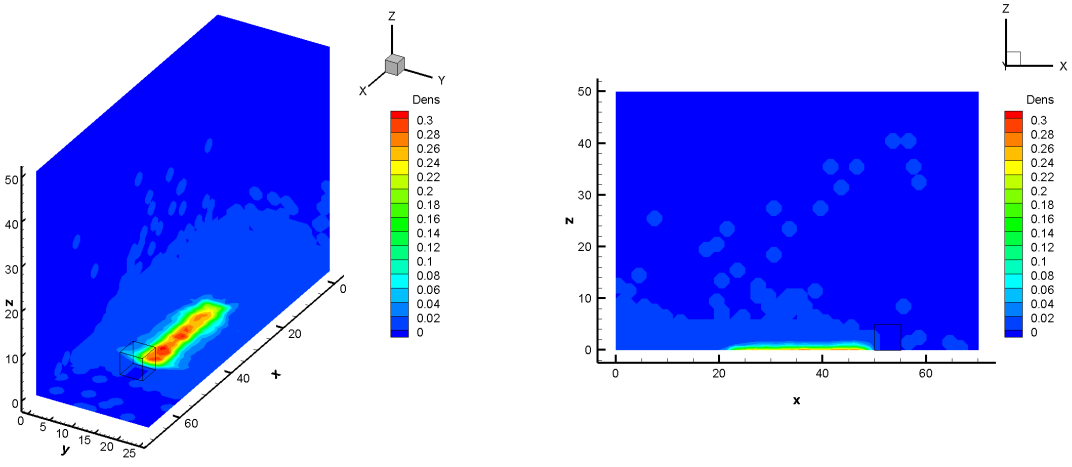

(a) Dust density (b) Dust density side view

Figure 6.17. Dust density of Case 2

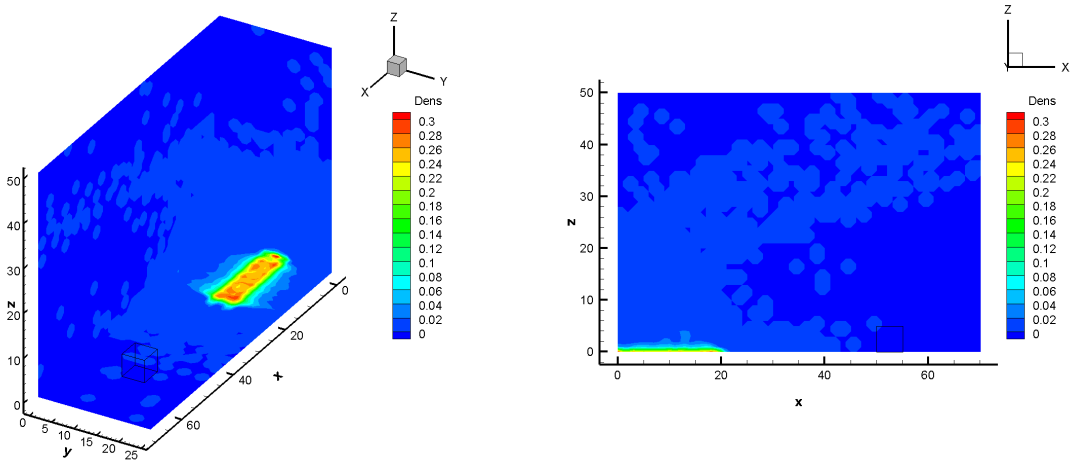

(a) Dust density

(b) Dust density side view

Figure 6.18. Dust density of Case 3

6.2.6.4. Case 4. In Case 4, the dust grains originated alongside the obstacle will still concentrate within ~2 m from the lunar surface. The further from the obstacle, the greater the density and lofted height of the dust will be (see Figure 6.19(a)). A slight amount of dust can be levitated to as high as the top surface of the obstacle. It can be seen from Figure 6.19(b) that some of the dust can reach to ~50 m. This can be caused by a greater accumulated electric charge on the dust, however it is not a general situation for charged dust grains, because only several dust grains can reach to such a height in Figure 6.19(b).

6.3. COUPLED SIMULATIONS FOR UNEVEN SURFACE TERRAIN

In this section, we will focus on the coupled simulation of the plasma and dust transport. We improved the FD-PIC code to include the influence of charged dust on local electrostatic environment in the simulations. The objective is to study the effect of the charged dust transport on local electrostatic environment. In the coupled simulations, the setups, including the computation domain dimension, solar wind conditions, and surface terrains, were the same as that of the uncoupled simulations as introduced in Section 6.2. In the simulations, about 315,000 solar wind electrons and 315,000 solar wind ions (about

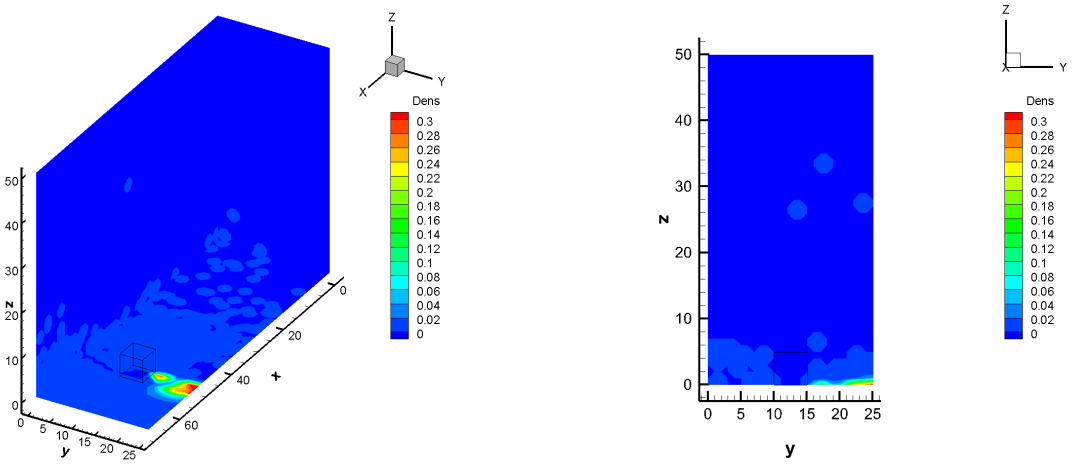

(a) Dust density

(b) Dust density side view

Figure 6.19. Dust density of Case 4

630,000 in total) were pre-loaded inside the computation domain (70×2×50 PIC cells, about 96.6×2.76×69.0 m). 2,100 solar wind electrons and 2,100 solar wind ions, and about 1,000 photoelectrons were injected into the computation domain in each time step (dt = 0.01, mesh size was 1.0). The simulation ran 100,000 steps for each cases, which was about 900 seconds in physical units, wall clock time was about 5 hours.

It should be noted that, since the dust grains are much larger and heavier compared to the electrons and ions, the time scale of dust motions is several orders of magnitude larger than that of the electrons and ions, which means that the dust grains are almost frozen from the electron's or ion's perspective in the simulations. Simulating the motion of electrons, ions, and charged dust grains with the same time scale is almost impossible. Therefore, in this study, the pushing process of the dust grains were activated every 10 iterations of the PIC simulation with a 1,000 times enlarged time scale (i.e., $dt_{dust} = dt \times 1000$). In the current simulations, the net charge accumulated on each dust grain was set as a constant value which was -1.0 $\times 10^5 e$, where e is the elementary charge, and the negative sign indicates the dust is negatively charged.

6.3.1. 2-D Dust Environment. The dust charge densities of Case 1, 2, and 3 are shown in Figure 6.20. The dust distributions at different time steps are shown in Figure 6.21. It can be seen that in most areas of the computation domain, the charge density caused by the charged dust remains near neutral. The lofted charged dust creates a negatively charged region as high as ~30 m from the lunar surface in all three cases, and most of the charge dust concentrates below ~3 m height. The charge density distribution is greater in Case 2 because the negatively charged dust is easily repelled by the negatively charged surface in the shadow region.

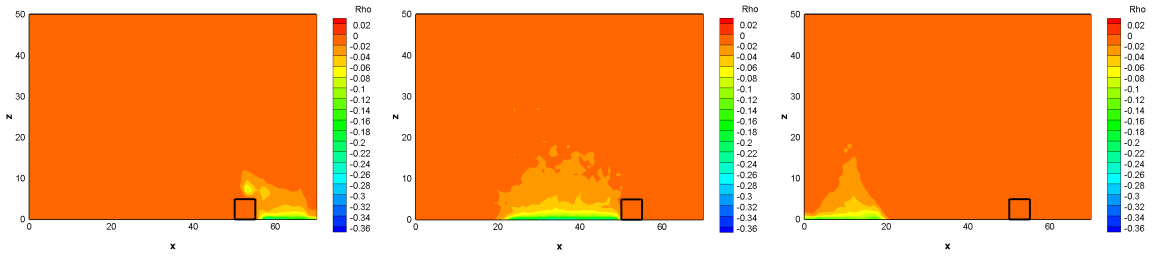

(a) Case 1 (b) Case 2 (c) Case 3

Figure 6.20. Charge density caused by dust

6.3.2. Comparisons between Uncoupled and Coupled Simulations. The comparisons of solar wind electron density, solar wind ion density, photoelectron density, total charge density, and electric potential are shown in Figures 6.22 - 6.24. It can be seen from the comparisons that, under average solar wind condition near lunar terminator region, the existence of the lofted charged dust does not have a noticeable effect on solar wind electron and ion density. The photoelectron concentrations are influenced by the charged dust generation location. The negatively charged dust repels the nearby negatively charged photoelectrons, creating a larger photoelectron void region. The electric potential profile is slightly affected by the existence of the charged dust as well, however such effect is not significant.

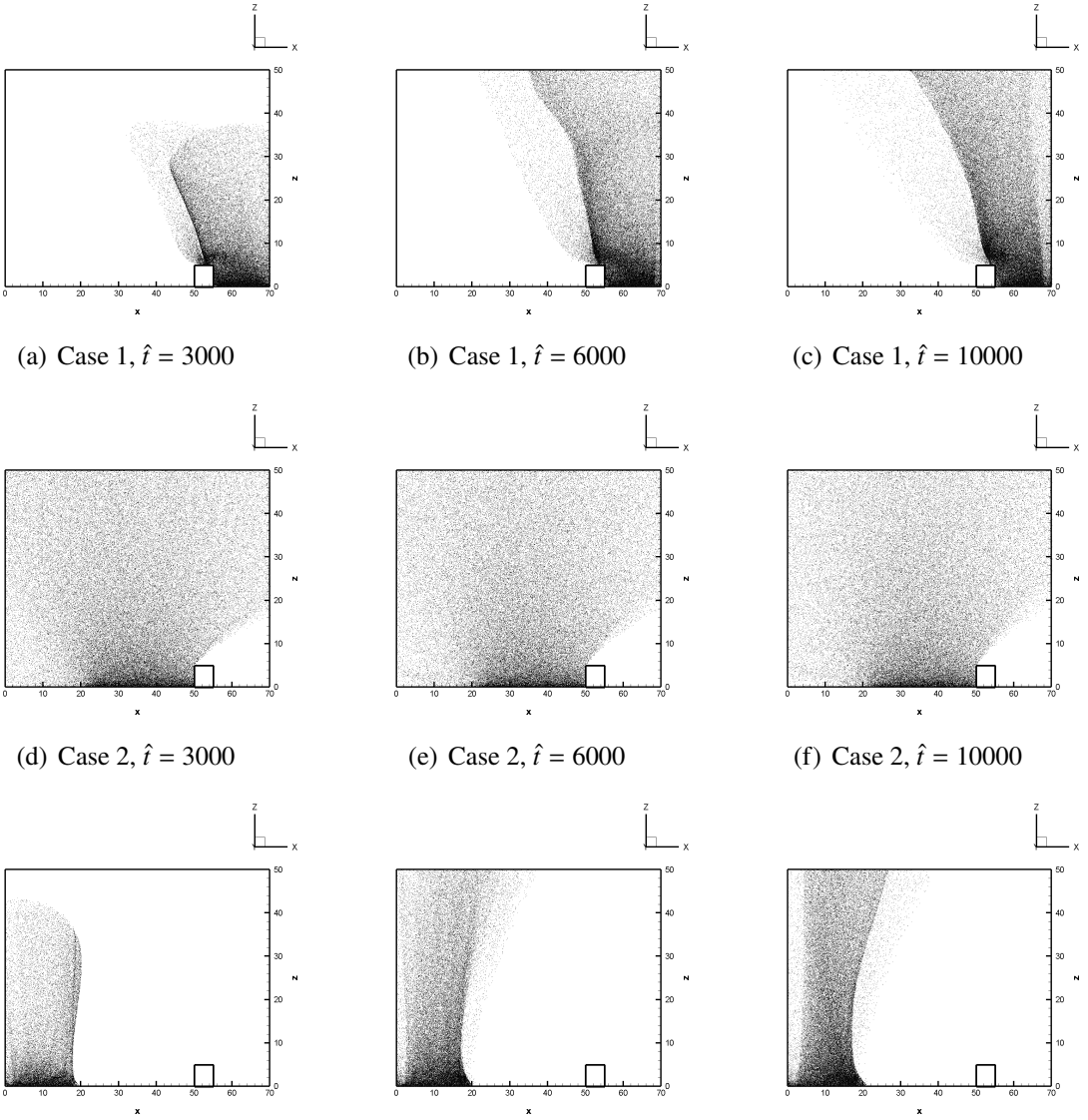

(a) Case 1, $\hat{t}$ = 3000 (b) Case 1, $\hat{t}$ = 6000 (c) Case 1, $\hat{t}$ = 10000

(d) Case 2, $\hat{t}$ = 3000 (e) Case 2, $\hat{t}$ = 6000 (f) Case 2, $\hat{t}$ = 10000

(g) Case 3, $\hat{t}$ = 3000 (h) Case 3, $\hat{t}$ = 6000 (i) Case 3, $\hat{t}$ = 10000

Figure 6.21. Dust distributions at different time steps

6.4. SUMMARY

In this section, we presented the 2-D and 3-D photoelectron sheath configurations at lunar terminator region (with 10° Sun elevation angle). The quantities of interest within the photoelectron sheath (electric potential, charge density, electric field, etc.) were obtained with the FD-PIC simulations. We also presented the study of the transport of lofted charged dust that originated from different locations on even and uneven lunar surfaces.

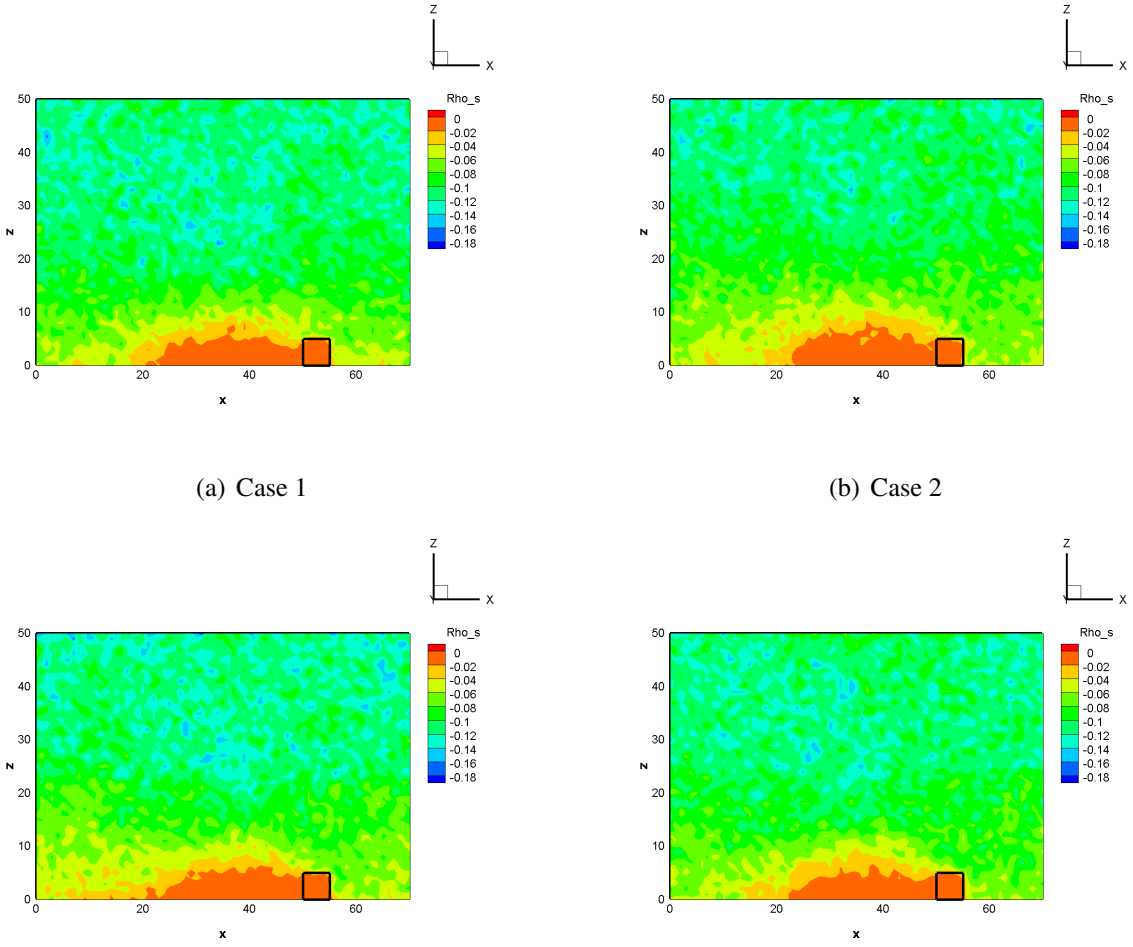

(a) Case 1

(b) Case 2

(c) Case 3

(d) Uncoupled

Figure 6.22. Comparisons of solar wind electron density

The simulation results showed that with 10° Sun elevation angle under average solar wind condition, the lunar surface potential can reach from -22 V in the shadow region behind a lunar surface construction to ~20 V on sunlit surface of the construction. With a initial upward velocity of 0.1 m/s, most of the charged lunar dust that originated from different locations would concentrate within a region of ~2 m height from lunar surface. A

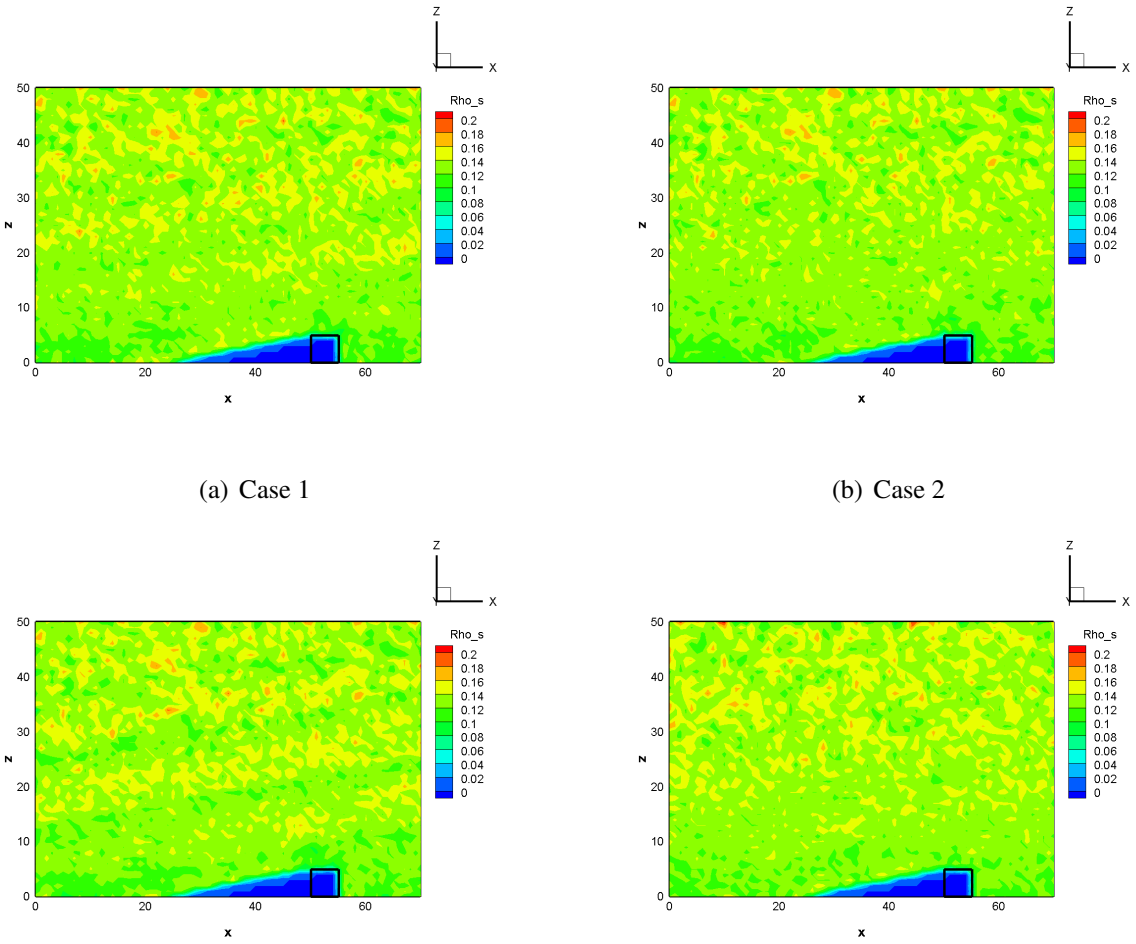

(a) Case 1

(b) Case 2

(c) Case 3

(d) Uncoupled

Figure 6.23. Comparisons of solar wind ion density

slight amount of dust with greater accumulated charge could be lofted higher and distributed into a larger area. The highest location that the dust originated alongside the construction could reach is lower compared with that of the dust originated from other locations.

We then presented the electrostatic environment and the charged dust transport above the lunar surface obtained with the coupled simulations. It can be concluded that under the average solar wind condition, the influence of the charged dust transport on the local electrostatic environment is not significant. It should be noted that we simplified our

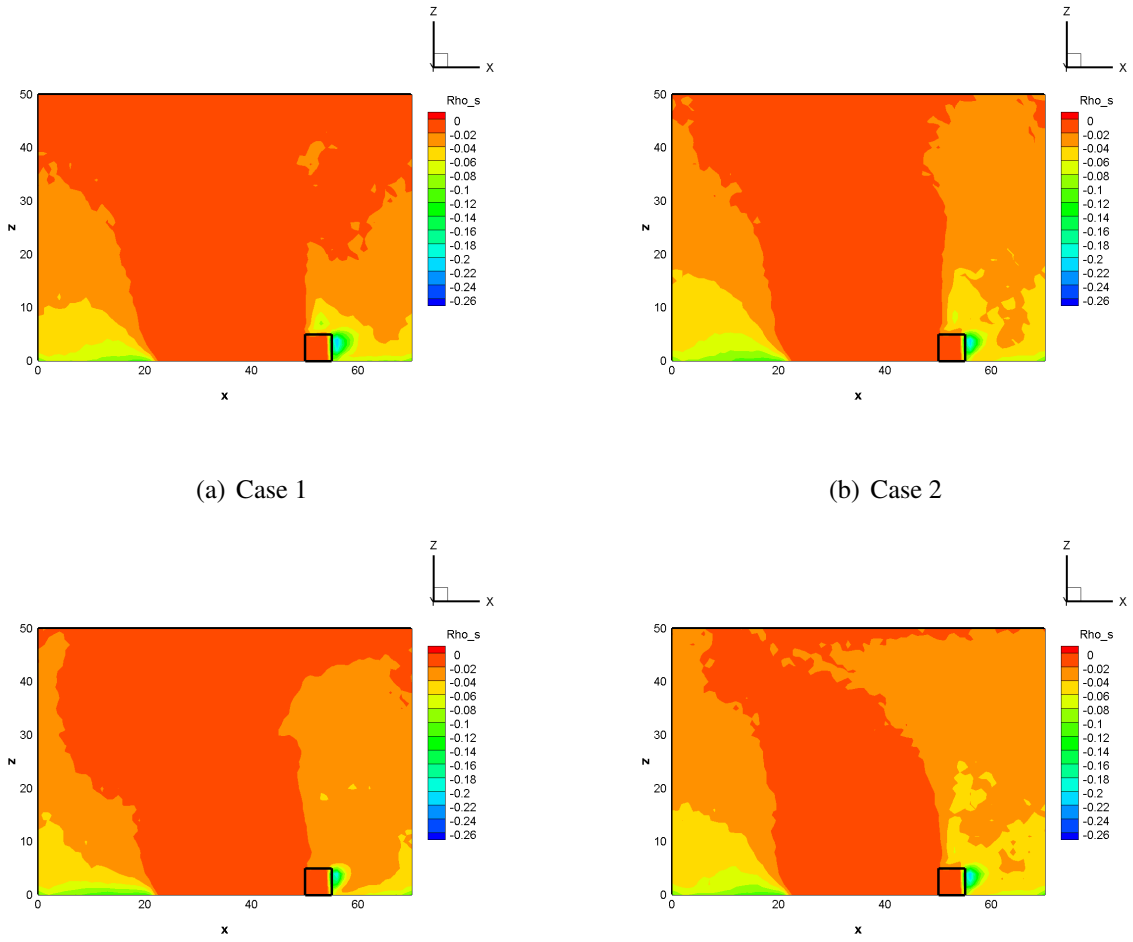

(a) Case 1

(b) Case 2

(c) Case 3

(d) Uncoupled

Figure 6.24. Comparisons of photoelectron density

model by using a constant charge value on all dust grains in the current simulations. To obtain more reliable consequences, more studies with different charge models and solar wind conditions are needed.

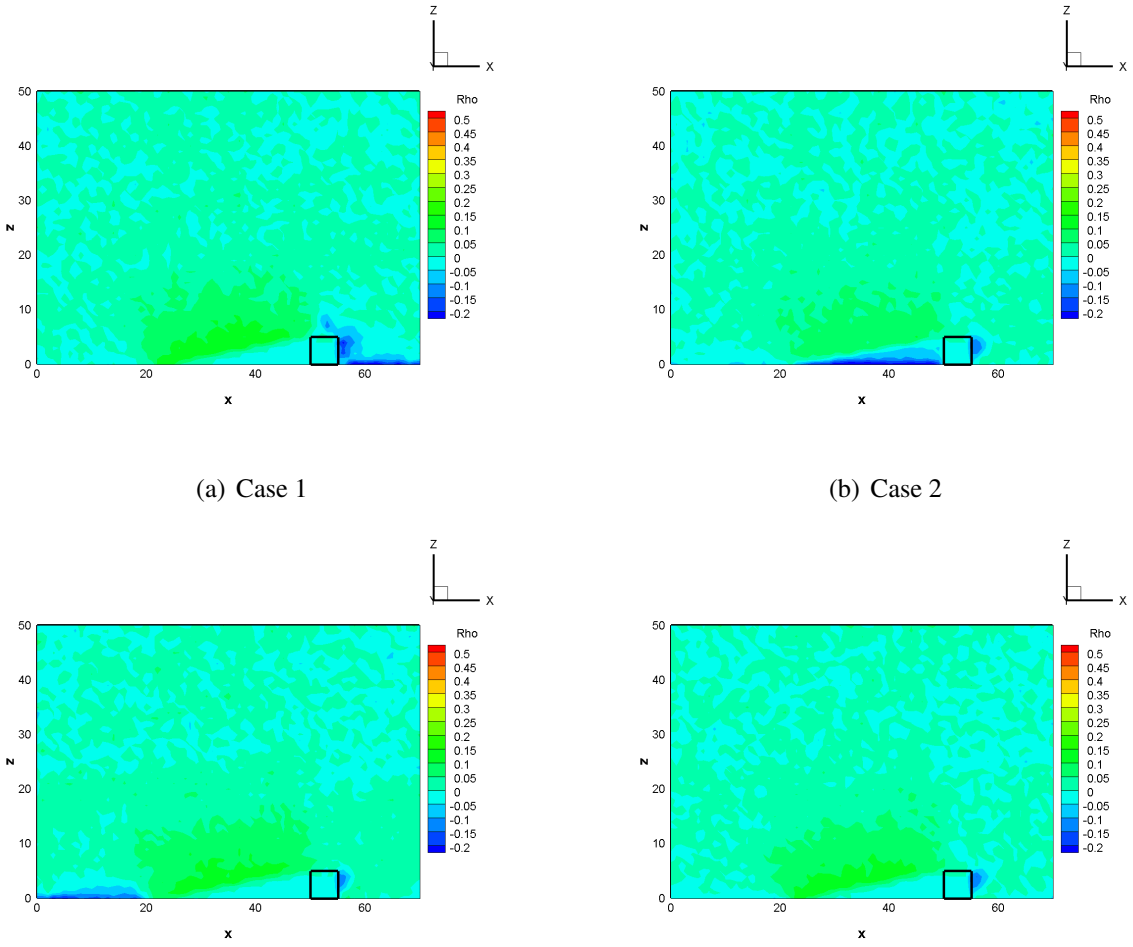

(a) Case 1

(b) Case 2

(c) Case 3

(d) Uncoupled

Figure 6.25. Comparisons of total charge density

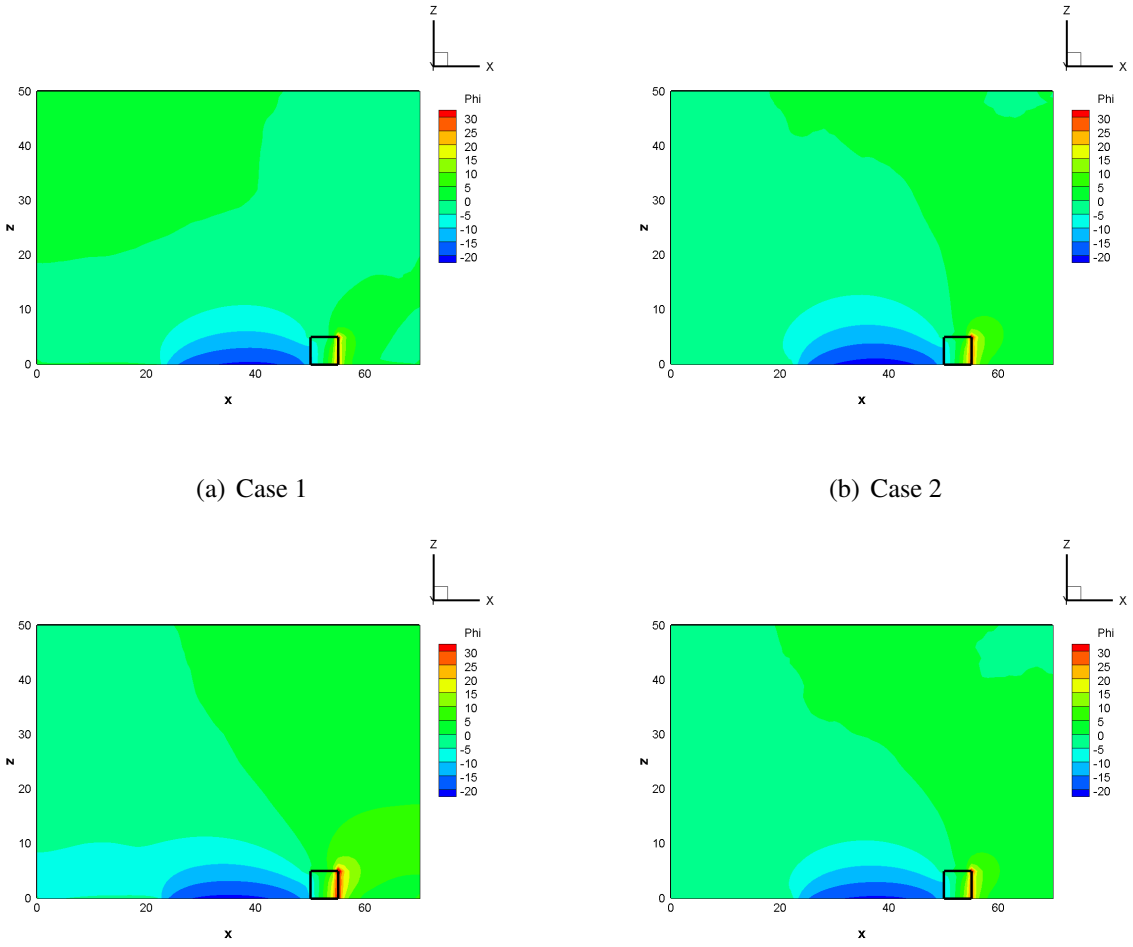

(a) Case 1

(b) Case 2

(c) Case 3

(d) Uncoupled

Figure 6.26. Comparisons of potential

7. CONCLUSIONS

This section will conclude the study in this dissertation. A summary of the work in each section and the contribution to the corresponding field of research will be briefly reviewed in Section 7.1. The conclusions of the study in this dissertation will be given in Section 7.2. The recommended future work will be provided in Section 7.3.

7.1. CONTRIBUTIONS

The study presented in this dissertation shows contributions to three areas including mathematical modeling and particle simulation of photoelectron sheath on lunar surface under average solar wind condition, and charged dust transport simulations within photoelectron sheath.

7.1.1. Contribution to Mathematical Modeling of Photoelectron Sheath. We provided the complete assumption and derivation of an analytic model to describe 1-D photoelectron sheath structure. A number of quantities of interest as functions of distance from lunar surface can be obtained with the analytic model, including electric potential, electric field, charge density, etc. The model is validated by comparing the semi-analytic solutions with the simulations which is independent to the model.

7.1.2. Contribution to Particle Simulation of Photoelectron Sheath. A package of fully kinetic FD-PIC code was introduced which is capable of numerically simulating the electrostatic environment in the photoelectron sheath, and providing the quantities of interest as functions of length from surface.

7.1.3. Contribution to Numerical Simulation of Charged Dust Transport. The FD-PIC code introduced in this dissertation was extended to include the functions to simulate the charged dust transport within photoelectron sheath. The dust transport functions are built into the code and coupled with the simulations of electrostatic environment, therefore the charged dust transport and the local electrostatic environment can influence each other.

7.2. CONCLUSIONS

7.2.1. Photoelectron Sheath. According to the semi-analytic and simulation study in this dissertation, it can be concluded that:

- The existence and the quantity of the photoelectrons have a significant influence on the photoelectron sheath structure near lunar surface.
- The Sun elevation angle determines the density of photoelectrons near the lunar surface, therefore influences the structure of the photoelectron sheath.
- The *Maxwellian* solar wind electrons show similar properties as that of κ-distribution under average solar wind condition, therefore is considered as accurate enough to simulate the photoelectron sheath.

7.2.2. Charged Dust Transport. According to the simulations of charged dust transport, it can be concluded that:

- With a initial upward velocity of 0.1 m/s, most of the charged lunar dust that originated from different locations will concentrate within a region of ~2 m height from the lunar surface.
- A slight amount of dust with greater accumulated charge can be levitated higher and distributed into a larger area.
- The highest altitude that the dust originated alongside a lunar surface structure can reach is lower compared with the dust originated from other locations.

7.3. RECOMMENDED FUTURE WORK

From the scope of the study in this dissertation, the following work can be recommended:

- The study of the influence of different lunar surface topographies, and different shapes and sizes of lunar landers and constructions.
- The study of the methods to improve the simulation code to achieve more efficient and computationally cheaper simulations. Such as parallel computations.
- The study of the solutions to couple the motion time scale of the electrons and ions with that of the charged dust, in order to achieve a more reliable and accurate simulation.
- The study of charging caused by secondary electrons between dust grains.
- The study of the effect of different Sun elevation angles and solar wind conditions.
- The study of uncertainty quantification of the numerical model with consideration of the fluctuations of key parameters.

APPENDIX

DERIVATION OF THE 1-D SEMI-ANALYTIC MODEL

The derivation process of the 1-D semi-analytic model is introduced in Section 4.3. In this appendix, we will present the extensions of each governing equation.

The densities of each population of electrons are given in Eqs. (1) - (4):

$$\begin{aligned} n_{\mathrm{swe,f}}(z) &= \int_{v_\mathrm{m}}^{\infty} n_{\mathrm{swe},\infty} f(v)\mathrm{d}v \\ &= \int_{v_\mathrm{m}}^{\infty} n_{\mathrm{swe},\infty} \frac{1}{\sqrt{\pi} v_{\mathrm{swe,th}}} \exp\left[-\frac{(v-v_\mathrm{d})^2}{{v_{\mathrm{swe,th}}}^2} \right] \exp\left[\frac{e(\phi_{(z)} - \phi_\infty)}{kT_\mathrm{swe}} \right] \mathrm{d}v \\ &= \frac{n_{\mathrm{swe},\infty}}{2} \exp\left[\frac{e(\phi_{(z)} - \phi_\infty)}{kT_\mathrm{swe}} \right] \left[1 - \mathrm{erf}\left(\sqrt{\frac{e(\phi_{(z)} - \phi_\mathrm{m})}{kT_\mathrm{swe}}} - \frac{v_\mathrm{d}}{v_{\mathrm{swe,th}}} \right) \right] \end{aligned} \tag{1}$$

$$\begin{aligned} n_{\mathrm{phe,f}}(z) &= \int_{v_\mathrm{m}}^{\infty} n_{\mathrm{phe},0} f(v)\mathrm{d}v \\ &= \int_{v_\mathrm{m}}^{\infty} n_{\mathrm{phe},0} \frac{1}{\sqrt{\pi} v_{\mathrm{phe,th}}} \exp\left[-\frac{(v-v_\mathrm{d})^2}{{v_{\mathrm{phe,th}}}^2} \right] \exp\left[\frac{e(\phi_{(z)} - \phi_0)}{kT_\mathrm{phe}} \right] \mathrm{d}v \\ &= \frac{n_{\mathrm{phe},0}}{2} \exp\left[\frac{e(\phi_{(z)} - \phi_0)}{kT_\mathrm{phe}} \right] \left[1 - \mathrm{erf}\left(\sqrt{\frac{e(\phi_{(z)} - \phi_\mathrm{m})}{kT_\mathrm{phe}}} \right) \right] \end{aligned} \tag{2}$$

$$\begin{aligned} n_{\mathrm{swe,r}}(z) &= 2\int_{0}^{v_\mathrm{m}} n_{\mathrm{swe},\infty} f(v)\mathrm{d}v \\ &= 2\int_{0}^{v_\mathrm{m}} n_{\mathrm{swe},\infty} \frac{1}{\sqrt{\pi} v_{\mathrm{swe,th}}} \exp\left[-\frac{(v-v_\mathrm{d})^2}{{v_{\mathrm{swe,th}}}^2} \right] \exp\left[\frac{e(\phi_{(z)} - \phi_\infty)}{kT_\mathrm{swe}} \right] \mathrm{d}v \\ &= n_{\mathrm{swe},\infty} \exp\left[\frac{e(\phi_{(z)} - \phi_\infty)}{kT_\mathrm{swe}} \right] \left[\mathrm{erf}\left(\sqrt{\frac{e(\phi_{(z)} - \phi_\mathrm{m})}{kT_\mathrm{swe}}} - \frac{v_\mathrm{d}}{v_{\mathrm{swe,th}}} \right) + \mathrm{erf}\left(\frac{v_\mathrm{d}}{v_{\mathrm{swe,th}}} \right) \right] \end{aligned} \tag{3}$$

$$
\begin{aligned}
n_{\mathrm{phe,c}}(z) &= 2\int_0^{v_\mathrm{m}} n_{\mathrm{phe},0} f(v)\mathrm{d}v \\
&= 2\int_0^{v_\mathrm{m}} n_{\mathrm{phe},0}\frac{1}{\sqrt{\pi}v_{\mathrm{phe,th}}}\exp\left[-\frac{v^2}{{v_{\mathrm{phe,th}}}^2}\right]\exp\left[\frac{e(\phi_{(z)}-\phi_0)}{kT_{\mathrm{phe}}}\right]\mathrm{d}v \\
&= n_{\mathrm{phe},0}\exp\left[\frac{e(\phi_{(z)}-\phi_0)}{kT_{\mathrm{phe}}}\right]\mathrm{erf}\left(\sqrt{\frac{e(\phi_{(z)}-\phi_\mathrm{m})}{kT_{\mathrm{phe}}}}\right)
\end{aligned} \tag{4}
$$

where $n_{\mathrm{swe,f}}$, $n_{\mathrm{phe,f}}$, $n_{\mathrm{swe,r}}$, and $n_{\mathrm{phe,c}}$ represent the densities of free solar wind electrons, free photoelectrons, reflected solar wind electrons, and captured photoelectrons, respectively; $n_{\mathrm{swe},\infty}$ and $v_{\mathrm{swe,th}}$ are density at infinity and thermal velocity of solar wind electrons; $n_{\mathrm{phe},0}$ and $v_{\mathrm{phe,th}}$ are density at the surface and thermal velocity of photoelectrons; $v_\mathrm{m} = \sqrt{2e(\phi_{(z)}-\phi_\mathrm{m})/m_\mathrm{swe}}$ is the minimum velocity required to travel over the potential barrier; ϕ_m is the minimum potential along the profile; and ϕ_∞ is the potential at infinity.

The ion density is obtained from continuity as in Eq. (5).

$$
n_{\mathrm{swi}}(z) = \frac{n_{\mathrm{swi},\infty}v_{\mathrm{swi},\infty}}{v_{\mathrm{swi}}(z)} = n_{\mathrm{swi},\infty}\left(1-\frac{2e\phi_{(z)}}{v_{\mathrm{swi},\infty}^2 m_{\mathrm{swi}}}\right)^{-\frac{1}{2}} \tag{5}
$$

where $n_{\mathrm{swi},\infty}$ and $v_{\mathrm{swi},\infty}$ are density and velocity of solar wind ions at infinity, respectively.

The Poisson's equation to calculate the potential can be written as Eq. (6):

$$
\frac{\mathrm{d}^2\phi}{\mathrm{d}z^2} = -\frac{e}{\epsilon_0}\left(n_{\mathrm{swi}} - n_{\mathrm{swe,f}} - n_{\mathrm{swe,r}} - n_{\mathrm{phe,f}} - n_{\mathrm{phe,c}}\right) \tag{6}
$$

where ϵ_0 is the vacuum permittivity.

The equations of zero charge density at infinity is shown in Eq. (7):

$$
\begin{aligned}
&n_{\mathrm{swe}}(\infty) + n_{\mathrm{phe}}(\infty) - n_{\mathrm{swi}}(\infty) = \\
&n_{\mathrm{swe,f}}(\infty) + n_{\mathrm{swe,r}}(\infty) + n_{\mathrm{phe,f}}(\infty) - n_{\mathrm{swi}}(\infty) = 0
\end{aligned} \tag{7}
$$

Equation (7) can also be written as Eq. (8):

$$\frac{n_{\mathrm{swe},\infty}}{2}\left[1+2\cdot\mathrm{erf}\left(\frac{v_{\mathrm{d}}}{v_{\mathrm{swe,th}}}\right)+\mathrm{erf}\left(\sqrt{-\frac{e\phi_{\mathrm{m}}}{kT_{\mathrm{swe}}}}-\frac{v_{\mathrm{d}}}{v_{\mathrm{swe,th}}}\right)\right] + \frac{n_{\mathrm{phe},0}}{2}\exp\left(-\frac{e\phi_0}{kT_{\mathrm{phe}}}\right)\left(1-\mathrm{erf}\sqrt{-\frac{e\phi_{\mathrm{m}}}{kT_{\mathrm{phe}}}}\right)-n_{\mathrm{swi},\infty}=0 \tag{8}$$

The equation of zero current density at infinity is shown in Eq. (9):

$$\begin{aligned} &J_{\mathrm{swe,f}}(\infty)+J_{\mathrm{phe,f}}(0)-J_{\mathrm{swi}}(\infty)\\ &=n_{\mathrm{swe,f}}\int_{v_{\mathrm{m}}(0)}^{\infty}vf_{\mathrm{swe}}(v)\mathrm{d}v+n_{\mathrm{phe,f}}\int_{-\infty}^{-v_{\mathrm{m}}(\infty)}vf_{\mathrm{phe}}(v)\mathrm{d}v+n_{\mathrm{swi},\infty}v_{\mathrm{swi},\infty}\\ &=0 \end{aligned} \tag{9}$$

Equation (9) can also be written as Eq. (10):

$$n_{\mathrm{phe},0}\exp\left[\frac{e(\phi_{\mathrm{m}}-\phi_0)}{kT_{\mathrm{phe}}}\right]-n_{\mathrm{swe},\infty}\sqrt{\frac{T_{\mathrm{swe}}}{T_{\mathrm{phe}}}}\left\{\exp\left[-\left(\sqrt{-\frac{e\phi_{\mathrm{m}}}{kT_{\mathrm{swe}}}}-\frac{v_{\mathrm{d}}}{v_{\mathrm{swe,th}}}\right)^2\right] + \frac{v_{\mathrm{d}}}{v_{\mathrm{phe,th}}}\sqrt{\pi}\mathrm{erfc}\left(\sqrt{-\frac{e\phi_{\mathrm{m}}}{kT_{\mathrm{swe}}}}-\frac{v_{\mathrm{d}}}{v_{\mathrm{swe,th}}}\right)\right\}+n_{\mathrm{swi},\infty}\sqrt{2\pi\frac{T_{\mathrm{swe}}}{T_{\mathrm{phe}}}\frac{m_{\mathrm{swe}}}{m_{\mathrm{swi}}}}M=0 \tag{10}$$

The equations of electric field are shown in Eqs. (13) - (17):

$$\nabla\cdot\mathbf{E}=\frac{\rho}{\epsilon_0} \tag{11}$$

$$\mathbf{E}=-\nabla\phi \tag{12}$$

$$
\begin{aligned}
E_{\mathrm{swe,f}}^2(z) &= 2\int_{\phi_\mathrm{m}}^{\phi_{(z)}} n_{\mathrm{swe,f}}\mathrm{d}\phi \\
&= \frac{T_\mathrm{swe}n_{\mathrm{swe},\infty}}{T_\mathrm{phe}n_{\mathrm{phe,ref}}}\left\{\exp\left[\frac{e(\phi_{(z)}-\phi_\infty)}{kT_\mathrm{swe}}\right]\left[1-\mathrm{erf}\left(\sqrt{\frac{e(\phi_{(z)}-\phi_\mathrm{m})}{kT_\mathrm{swe}}}-\frac{v_\mathrm{d}}{v_{\mathrm{swe,th}}}\right)\right]\right. \\
&\quad -\exp\left[\frac{e(\phi_\mathrm{m}-\phi_\infty)}{kT_\mathrm{swe}}\right]\left[1-\mathrm{erf}\left(-\frac{v_\mathrm{d}}{v_{\mathrm{swe,th}}}\right)\right] \\
&\quad \left.+\frac{v_{\mathrm{swe,th}}}{\sqrt{\pi}v_\mathrm{d}}\exp\left[\frac{e(\phi_\mathrm{m}-\phi_\infty)}{kT_\mathrm{swe}}-\frac{{v_\mathrm{d}}^2}{{v_{\mathrm{swe,th}}}^2}\right]\left[\exp\left(2\frac{v_\mathrm{d}}{v_{\mathrm{swe,th}}}\sqrt{\frac{e(\phi_{(z)}-\phi_\mathrm{m})}{kT_\mathrm{swe}}}\right)-1\right]\right\}
\end{aligned}
\tag{13}
$$

$$
\begin{aligned}
E_{\mathrm{phe,f}}^2(z) &= 2\int_{\phi_\mathrm{m}}^{\phi_{(z)}} n_{\mathrm{phe,f}}\mathrm{d}\phi \\
&= \frac{n_{\mathrm{phe},0}}{n_{\mathrm{phe,ref}}}\left\{\exp\left[\frac{e(\phi_{(z)}-\phi_0)}{kT_\mathrm{phe}}\right]\left[1-\mathrm{erf}\left(\sqrt{\frac{e(\phi_{(z)}-\phi_\mathrm{m})}{kT_\mathrm{phe}}}\right)\right]\right. \\
&\quad \left.-\exp\left[\frac{e(\phi_\mathrm{m}-\phi_0)}{kT_\mathrm{phe}}\right]\left[1-\frac{2}{\sqrt{\pi}}\sqrt{\frac{e(\phi_{(z)}-\phi_\mathrm{m})}{kT_\mathrm{phe}}}\right]\right\}
\end{aligned}
\tag{14}
$$

$$
\begin{aligned}
E_{\mathrm{swe,r}}^2(z) &= 2\int_{\phi_\mathrm{m}}^{\phi_{(z)}} n_{\mathrm{swe,r}}\mathrm{d}\phi \\
&= \frac{2T_\mathrm{swe}n_{\mathrm{swe},\infty}}{T_\mathrm{phe}n_{\mathrm{phe,ref}}}\left\{\exp\left[\frac{e(\phi_{(z)}-\phi_\infty)}{kT_\mathrm{swe}}\right]\right. \\
&\qquad \left[\mathrm{erf}\left(\sqrt{\frac{e(\phi_{(z)}-\phi_\mathrm{m})}{kT_\mathrm{swe}}}-\frac{v_\mathrm{d}}{v_{\mathrm{swe,th}}}\right)+\mathrm{erf}\left(\frac{v_\mathrm{d}}{v_{\mathrm{swe,th}}}\right)\right] \\
&\quad \left.-\frac{v_{\mathrm{swe,th}}}{\sqrt{\pi}v_\mathrm{d}}\exp\left[\frac{e(\phi_\mathrm{m}-\phi_\infty)}{kT_\mathrm{swe}}-\frac{{v_\mathrm{d}}^2}{{v_{\mathrm{swe,th}}}^2}\right]\left[\exp\left(2\frac{v_\mathrm{d}}{v_{\mathrm{swe,th}}}\sqrt{\frac{e(\phi_{(z)}-\phi_\mathrm{m})}{kT_\mathrm{swe}}}\right)-1\right]\right\}
\end{aligned}
\tag{15}
$$

$$
\begin{aligned}
E_{\mathrm{phe,c}}^2(z) &= 2\int_{\phi_\mathrm{m}}^{\phi_{(z)}} n_{\mathrm{phe,c}}\mathrm{d}\phi \\
&= \frac{2n_{\mathrm{phe,0}}}{n_{\mathrm{phe,ref}}}\left\{\exp\left[\frac{e(\phi_{(z)}-\phi_0)}{kT_{\mathrm{phe}}}\right]\left[\mathrm{erf}\left(\sqrt{\frac{e(\phi_{(z)}-\phi_\mathrm{m})}{kT_{\mathrm{phe}}}}\right)\right]\right. \\
&\quad \left. -\frac{2}{\sqrt{\pi}}\exp\left[\frac{e(\phi_\mathrm{m}-\phi_0)}{kT_{\mathrm{phe}}}\right]\sqrt{\frac{e(\phi_{(z)}-\phi_\mathrm{m})}{kT_{\mathrm{phe}}}}\right\}
\end{aligned} \tag{16}
$$

$$
\begin{aligned}
E_{\mathrm{swi}}^2(z) &= -2\int_{\phi_\mathrm{m}}^{\phi_{(z)}} n_{\mathrm{swi}}\mathrm{d}\phi \\
&= \frac{2T_{\mathrm{swe}}n_{\mathrm{swi},\infty}}{T_{\mathrm{phe}}n_{\mathrm{phe,ref}}}M^2\left[\sqrt{1-\frac{2e\phi_{(z)}}{kT_{\mathrm{swe}}M^2}}-\sqrt{1-\frac{2e\phi_\mathrm{m}}{kT_{\mathrm{swe}}M^2}}\right]
\end{aligned} \tag{17}
$$

where $E_{\mathrm{swe,f}}$, $E_{\mathrm{phe,f}}$, $E_{\mathrm{swe,r}}$, $E_{\mathrm{phe,c}}$, and E_{swi} is the electric field of free solar wind electrons, free photoelectrons, reflected solar wind electrons, captured photoelectrons, and solar wind ions, respectively; $n_{\mathrm{phe,ref}}$ is the reference photoelectron density at the Sun elevation angle of 90° (normal incidence); and $M = v_\mathrm{d}/C_\mathrm{s}$ is the ion Mach number where $C_\mathrm{s} = \sqrt{kT_{\mathrm{swe}}/m_{\mathrm{swi}}}$ is the ion acoustic velocity in the solar wind. The zero electric field condition at infinity can then be described as Eq. (18):

$$
E^2(\infty) = E_{\mathrm{swe,f}}^2(\infty) + E_{\mathrm{swe,r}}^2(\infty) + E_{\mathrm{phe,f}}^2(\infty) + E_{\mathrm{swi}}^2(\infty) = 0 \tag{18}
$$

REFERENCES

Abbas, M., Tankosic, D., Craven, P., Spann, J., LeClair, A., and West, E., 'Lunar dust charging by photoelectric emissions,' Planetary and Space Science, 2007, **55**(7-8), pp. 953–965, ISSN 0032-0633, doi:10.1016/j.pss.2006.12.007.

Abdul, R. and Mace, R., 'A method to generate kappa distributed random deviates for particle-in-cell simulations,' Computer Physics Communications, 2014, **185**(10), pp. 2383 – 2386, ISSN 0010-4655, doi:https://doi.org/10.1016/j.cpc.2014.05.006.

Austin, A., Sherwood, B., Elliott, J., Colaprete, A., Zacny, K., Metzger, P., Sims, M., Schmitt, H., Magnus, S., Fong, T., Smith, M., Casillas, R. P., Howe, A. S., Voecks, G., Vaquero, M., and Vendiola, V., 'Robotic lunar surface operations 2,' Acta Astronautica, 2020, **176**, pp. 424–437, ISSN 0094-5765, doi:https://doi.org/10.1016/j.actaastro.2020.06.038.

Baiden, G., Grenier, L., and Blair, B., 'Lunar underground mining and construction: A terrestrial vision enabling space exploration and commerce,' in '48th AIAA Aerospace Sciences Meeting Including the New Horizons Forum and Aerospace Exposition,' 2010 p. 1548.

Żbik, M. S., 'Possible morphological similarities between lunar dust particles and interplanetary dust particles collected from Earth's atmosphere,' Advances in Space Research, 2020, **66**(3), pp. 715–719, ISSN 0273-1177, doi:https://doi.org/10.1016/j.asr.2020.04.017.

Birdsall, C. and Langdon, A., *Plasma Physics via Computer Simulation*, Series in Plasma Physics, CRC Press, 2018, ISBN 9781482263060.

Bramble, J. H. and King, J. T., 'A finite element method for interface problems in domains with smooth boundaries and interfaces,' Advances in Computational Mathematics, 1996, **6**(1), pp. 109–138.

Carroll, A., Hood, N., Mike, R., Wang, X., Hsu, H.-W., and Horányi, M., 'Laboratory measurements of initial launch velocities of electrostatically lofted dust on airless planetary bodies,' Icarus, 2020, **352**, p. 113972, ISSN 0019-1035, doi:https://doi.org/10.1016/j.icarus.2020.113972.

Christoffersen, R. and Lindsay, J. F., 'Lunar dust effects on spacesuit systems: insights from the Apollo spacesuits,' Technical report, Johnson Space Center, 2009.

Christon, S. P., Mitchell, D. G., Williams, D. J., Frank, L. A., and Huang, C. Y., 'Spectral characteristics of plasma sheet ion and electron populations during undisturbed geomagnetic conditions,' Journal of Geophysical Research: Space Physics, 1989, **94**(A10), pp. 13409–13424, doi:10.1029/JA094iA10p13409.

Christon, S. P., Mitchell, D. G., Williams, D. J., Frank, L. A., Huang, C. Y., and Eastman, T. E., 'Energy spectra of plasma sheet ions and electrons from 50 ev/e to 1 mev during plasma temperature transitions,' Journal of Geophysical Research: Space Physics, 1988, **93**(A4), pp. 2562–2572, doi:10.1029/JA093iA04p02562.

Corazzari, I., Durante, M., Fubini, B., Karlsson, L., Linnarsson, D., Loftus, D., Mcdonald, F., Palmberg, L., Prisk, G., Staufer, U., Westrenen, W., Tranfield, E., and Turci, F., *History and Future Perspectives for the Evaluation of the Toxicity of Celestial Dust*, p. 46, ISBN 1-5275-6308-1, 01 2021.

Eastwood, J. W., Arter, W., Brealey, N. J., and Hockney, R. W., 'Body-fitted electromagnetic pic software for use on parallel computers,' Computer Physics Communications, 1995, **87**(1-2), pp. 155–178.

Farr, B., Wang, X., Goree, J., Hahn, I., Israelsson, U., and Horányi, M., 'Dust mitigation technology for lunar exploration utilizing an electron beam,' Acta Astronautica, 2020, **177**, pp. 405–409, ISSN 0094-5765, doi:https://doi.org/10.1016/j.actaastro.2020.08.003.

Farrell, W. M., Stubbs, T. J., Halekas, J. S., Collier, G. T. D. M. R., Vondrak, R. R., and Lin, R. P., 'Loss of solar wind plasma neutrality and affect on surface potentials near the lunar terminator and shadowed polar regions,' Geophysical Research Letters, 2008a, **35**(5).

Farrell, W. M., Stubbs, T. J., Halekas, J. S., Delory, G. T., Collier, M. R., Vondrak, R. R., and Lin, R. P., 'Loss of solar wind plasma neutrality and affect on surface potentials near the lunar terminator and shadowed polar regions,' Geophysical Research Letters, March 2008b, **35**(5), p. L05105, doi:10.1029/2007GL032653.

Farrell, W. M., Stubbs, T. J., Vondrak, R. R., Delory, G. T., and Halekas, J. S., 'Complex electric fields near the lunar terminator: The near-surface wake and accelerated dust,' Geophysical Research Letters, 2007, **34**(14), doi:10.1029/2007GL029312.

French, B. M., Heiken, G., Vaniman, D., and Schmitt, J., *Lunar sourcebook: A user's guide to the Moon*, CUP Archive, 1991.

Fu, J. H. M., 'Surface potential of a photoemitting plate,' Journal of Geophysical Research (1896-1977), 1971, **76**(10), pp. 2506–2509, doi:10.1029/JA076i010p02506.

Gault, D. E., Shoemaker, E. M., and Moore, H. J., *Spray ejected from the lunar surface by meteoroid impact*, National Aeronautics and Space Administration, 1963.

Gawronska, A., Barrett, N., Boazman, S., Gilmour, C., Halim, S., Harish, McCanaan, K., Satyakumar, A., Shah, J., Meyer, H., and Kring, D., 'Geologic context and potential eva targets at the lunar south pole,' Advances in Space Research, 2020, **66**(6), pp. 1247–1264, ISSN 0273-1177, doi:https://doi.org/10.1016/j.asr.2020.05.035.

Godwin, R., *Apollo 17: The NASA Mission Reports, Vol. 1*, Apogee Books, 2002.

Gosling, J. T., 'Chapter 5 - the solar wind,' in L.-A. McFadden, P. R. Weissman, and T. V. Johnson, editors, 'Encyclopedia of the Solar System (Second Edition),' pp. 99–116, Academic Press, San Diego, second edition edition, ISBN 978-0-12-088589-3, 2007, doi:https://doi.org/10.1016/B978-012088589-3/50009-8.

Halekas, J. S., Bale, S. D., Mitchell, D. L., and Lin, R. P., 'Electrons and magnetic fields in the lunar plasma wake,' Journal of Geophysical Research: Space Physics, 2005a, **110**(A7), doi:10.1029/2004JA010991.

Halekas, J. S., Delory, G. T., Brain, D. A., Lin, R. P., Fillingim, M. O., Lee, C. O., Mewaldt, R. A., Stubbs, T. J., Farrell, W. M., and Hudson, M. K., 'Extreme lunar surface charging during solar energetic particle events,' Geophysical Research Letters, January 2007, **34**(2), p. L02111, doi:10.1029/2006GL028517.

Halekas, J. S., Delory, G. T., Farrell, W. M. ., Angelopoulos, V., McFadden, J. P., Bonnell, J. W., Fillingim, M. O., and Plaschke, F., 'First remote measurements of lunar surface charging from artemis: Evidence for nonmonotonic sheath potentials above the dayside surface,' Journal of Geophysical Research, July 2011, **116**(A7), p. A07103, doi:10.1029/2011JA016542, solar and Heliospheric Physics.

Halekas, J. S., Lin, R. P., and Mitchell, D. L., 'Large negative lunar surface potentials in sunlight and shadow,' Geophysical Research Letters, 2005b, **32**(9), doi:10.1029/2005GL022627.

Halekas, J. S., Poppe, A. R., and McFadden, J. P., 'The effects of solar wind velocity distributions on the refilling of the lunar wake: Artemis observations and comparisons to one-dimensional theory,' Journal of Geophysical Research: Space Physics, 2014, **119**(7), pp. 5133–5149, doi:10.1002/2014JA020083.

Han, D., *Particle-in-Cell Simulations of Plasma Interactions with Asteroidal and Lunar Surfaces*, Ph.D. thesis, University of Southern California, 2015.

Hartung, J. B., Hörz, F., and Gault, D. E., 'Lunar microcraters and interplanetary dust,' in 'Lunar and Planetary Science Conference Proceedings,' volume 3, 1972 p. 2735.

Hartzell, C. M. and Scheeres, D. J., 'The role of cohesive forces in particle launching on the moon and asteroids,' Planetary and Space Science, 2011, **59**(14), pp. 1758–1768.

Hartzell, C. M. and Scheeres, D. J., 'Dynamics of levitating dust particles near asteroids and the moon,' Journal of Geophysical Research: Planets, 2013, **118**(1), pp. 116–125.

Hartzell, C. M., Wang, X., Scheeres, D. J., and Horányi, M., 'Experimental demonstration of the role of cohesion in electrostatic dust lofting,' Geophysical research letters, 2013, **40**(6), pp. 1038–1042.

Hastings, D. and Garrett, H., *Spacecraft-Environment Interactions*, Cambridge University Press, Cambridge, UK, 2004.

Heiken, G. H., Vaniman, D. T., and French, B. M., *Lunar Sourcebook: A User's Guide to the Moon*, Cambridge University Press, 1991.

Hewett, D. W., 'The embedded curved boundary method for orthogonal simulation meshes,' Journal of Computational Physics, 1997, **138**(2), pp. 585–616.

Jackson, J. D., *Classical Electrodynamics, 3rd ed*, John Wiley & Sons, inc., NewYork, NY, 1999.

Jiang, M., Dai, Y., Cui, L., and Xi, B., 'Soil mechanics–based testbed setup for lunar rover wheel and corresponding experimental investigations,' Journal of Aerospace Engineering, 2017, **30**(6), p. 06017005.

Kawamoto, H., 'Vibration transport of lunar regolith for in situ resource utilization using piezoelectric actuators with displacement-amplifying mechanism,' Journal of Aerospace Engineering, 2020, **33**(3), p. 04020014, doi:10.1061/(ASCE)AS.1943-5525.0001128.

Kuznetsov, I. A., Hess, S. L. G., Zakharov, A. V., Cipriani, F., Seran, E., Popel, S. I., Lisin, E. A., Petrov, O. F., Dolnikov, G. G., Lyash, A. N., *et al.*, 'Numerical modelling of the luna-glob lander electric charging on the lunar surface with spis-dust,' Planetary and Space Science, 2018, **156**, pp. 62–70.

Lund, D., Zhao, J., Lamb, A., and Han, D., 'Fully kinetic pife-pic simulations of plasma charging at lunar craters,' in 'AIAA Scitech 2020 Forum,' 2020 doi:10.2514/6.2020-1549.

McCoy, J. E. and Criswell, D. R., 'Evidence for a high altitude distribution of lunar dust,' in 'Evidence for a high altitude distribution of lunar dust,' Pergamon Press, 1974.

Metzger, P. T., Zacny, K., and Morrison, P., 'Thermal extraction of volatiles from lunar and asteroid regolith in axisymmetric Crank-Nicolson modeling,' Journal of Aerospace Engineering, 2020, **33**(6), p. 04020075, doi:10.1061/(ASCE)AS.1943-5525.0001165.

Morris, A. B., Goldstein, D. B., Varghese, P. L., and Trafton, L. M., 'Lunar dust transport resulting from single-and four-engine plume impingement,' AIAA Journal, 2016, **54**(4), pp. 1339–1349.

Nitter, T., Havnes, O., and Melandsø, F., 'Levitation and dynamics of charged dust in the photoelectron sheath above surfaces in space,' Journal of Geophysical Research: Space Physics, 1998, **103**(A4), pp. 6605–6620, doi:10.1029/97JA03523.

Popel, S. I., Golub', A. P., Izvekova, Y. N., Afonin, V. V., Dol'nikov, G. G., Zakharov, A. V., Zelenyi, L. M., Lisin, E. A., and Petrov, O. F., 'On the distributions of photoelectrons over the illuminated part of the moon,' JETP Letters, apr 2014, **99**(3), pp. 115–120, doi:10.1134/s0021364014030114.

Popel, S. I., Kopnin, S. I., Golub', A. P., Dol'nikov, G. G., Zakharov, A. V., Zelenyi, L. M., and Izvekova, Y. N., 'Dusty plasma at the surface of the moon,' Solar System Research, nov 2013, **47**(6), pp. 419–429, doi:10.1134/s0038094613060063.

Poppe, A., Halekas, J. S., and Horányi, M., 'Negative potentials above the day-side lunar surface in the terrestrial plasma sheet: Evidence of non-monotonic potentials,' Geophysical Research Letters, January 2011, **38**(2), p. L02103, doi:10.1029/2010GL046119, space Sciences.

Poppe, A. and Horányi, M., 'Simulations of the photoelectron sheath and dust levitation on the lunar surface,' Journal of Geophysical Research, August 2010, **115**(A8), p. A08106, doi:10.1029/2010JA015286.

Poppe, A. R., *Modeling, Theoretical and Observational Studies of the Lunar Photoelectron Sheath*, Ph.D. thesis, University of Colorado, Boulder, 2011.

Poppe, A. R., Piquette, M., Likhanskii, A., and Horányi, M., 'The effect of surface topography on the lunar photoelectron sheath and electrostatic dust transport,' Icarus, 2012, **221**, pp. 135–146.

Reiss, P., Hoehn, A., Walter, U., Barber, S., and Carpenter, J., 'Implications of sample size for the thermal extraction of volatiles from lunar regolith with the prospect instrument package,' Journal of Aerospace Engineering, 2017, **30**(3), p. 04016088, doi:10.1061/(ASCE)AS.1943-5525.0000688.

Rhodes, D. J., Farrell, W. M., and Jason, L. M., 'Tribocharging and electrical grounding of a drill in shadowed regions of the moon,' Advances in Space Research, 2020, **66**(4), pp. 753–759, ISSN 0273-1177, doi:https://doi.org/10.1016/j.asr.2020.05.005.

Sharma, H., Hedman, M. M., Wooden, D. H., Colaprete, A., and Cook, A. M., 'Constraining low-altitude lunar dust using the ladee-uvs data,' Journal of Geophysical Research: Planets, 2021, **126**(11), p. e2021JE006935.

Slavin, J. A., Smith, E. J., Sibeck, D. G., Baker, D. N., Zwickl, R. D., and Akasofu, S.-I., 'An isee 3 study of average and substorm conditions in the distant magnetotail,' Journal of Geophysical Research: Space Physics, 1985, **90**(A11), pp. 10875–10895, doi:10.1029/JA090iA11p10875.

Stubbs, T., Farrell, W., Halekas, J., Burchill, J., Collier, M., Zimmerman, M., Vondrak, R., Delory, G., and Pfaff, R., 'Dependence of lunar surface charging on solar wind plasma conditions and solar irradiation,' Planetary and Space Science, Januray 2014, **90**, pp. 10–27, doi:10.1016/j.pss.2013.07.008.

Summers, D. and Thorne, R. M., 'The modified plasma dispersion function,' Physics of Fluids B: Plasma Physics, 1991, **3**(8), pp. 1835–1847, doi:10.1063/1.859653.

Vasyliunas, V. M., '12. deep space plasma measurements,' in R. H. Lovberg and H. R. Griem, editors, 'Plasma Physics,' volume 9 of *Methods in Experimental Physics*, pp. 49 – 88, Academic Press, 1971, doi:https://doi.org/10.1016/S0076-695X(08)60859-5.

Wagner, S. A., 'The apollo experience lessons learned for constellation lunar dust management,' NASA Technical Publication TP-2006-213726. Washington, DC: National Aeronautics and Space Administration, 2006.

Wang, J., He, X., and Cao, Y., 'Modeling electrostatic levitation of dust particles on lunar surface,' IEEE Transactions on Plasma Science, October 2008, **36**(5), pp. 2459–2466, doi:10.1109/TPS.2008.2003016.

Wang, X., Schwan, J., Hsu, H.-W., Grün, E., and Horányi, M., 'Dust charging and transport on airless planetary bodies,' Geophysical Research Letters, June 2016, **43**(12), pp. 6103–6110, doi:10.1002/2016GL069491.

Willis, R., Anderegg, M., Feuerbacher, B., and Fitton, B., 'Photoemission and secondary electron emission from lunar surface material,' in R. Grard, editor, 'Photon and Particle Interactions with Surfaces in Space,' volume 37 of *Astrophysics and Space Science Library*, pp. 389–401, Springer Netherlands, ISBN 978-94-010-2649-9, 1973, doi:10.1007/978-94-010-2647-5_25.

Woodcock, G. R., 'Robotic lunar surface operations,' Boeing aerospace and electronics, NASA contract NAS2-12108, 1990, pp. 5–7.

Zhao, J., Wei, X., Hu, Z., He, X., Han, D., Hu, Z., and Du, X., 'Photoelectron sheath near the lunar surface: Fully kinetic modeling and uncertainty quantification analysis,' in 'AIAA SciTech 2020,' AIAA 2020-1548, Orlando, Florida, January 6-10, 2020a doi:10.2514/6.2020-1548.

Zhao, J., Wei, X., Hu, Z., He, X., Han, D., Hu, Z., and Du, X., 'Photoelectron sheath near the lunar surface: Fully kinetic modeling and uncertainty quantification analysis,' in 'AIAA Scitech 2020 Forum,' 2020b doi:10.2514/6.2020-1548.

Zimmerman, M. I., Farrell, W. M., Hartzell, C. M., Wang, X., Horanyi, M., Hurley, D. M., and Hibbitts, K., 'Grain-scale supercharging and breakdown on airless regoliths,' Journal of Geophysical Research: Planets, October 2016, **121**(10), pp. 2150–2165, doi:10.1002/2016JE005049.

Zook, H. A. and McCoy, J. E., 'Large scale lunar horizon glow and a high altitude lunar dust exosphere,' Geophysical Research Letters, 1991, **18**(11), pp. 2117–2120, ISSN 1944-8007, doi:10.1029/91GL02235.

VITA

Jianxun Zhao received his Bachelor's degree in Mechanical Engineering from Northeast Electric Power University, China, in 2012. He continued his study there and received the Master's degree in 2017. He started his Ph.D study in 2018, and had been working with Dr. Daoru Han until he received the Ph.D degree in July 2022 in Aerospace Engineering at Missouri University of Science and Technology, Rolla, MO, USA.